Towards a Miniaturized Device for Sorting of Biological Material

Clausen, Casper Hyttel

Publication date:
2011

Document Version
Publisher's PDF, also known as Version of record

DTU Nanotech
Department of Micro- and Nanotechnology

Technical University
of Denmark

Towards a Miniaturized Device for Sorting of Biological Material

Ph.D. Thesis

Casper Hyttel Clausen, s011699

Supervisors:
Associate Prof. Winnie Edith Svendsen
Assistant Prof. Maria Dimaki

NaBIS Group
Department of Micro and Nanotechnology
Technical University of Denmark
June 23, 2010

Abstract

The goal of this project was to investigate the properties of human chromosomes and superstructures of peptides. EFM was used to investigate the dielectric constant, while DEP manipulation was used to determine the conductivity.

Electrostatic force microscopy phase mode, (EFM)-phase, was used to investigate the dielectric constant of the human chromosomes and peptide structures in a dry state. It was observed that the EFM-phase method gave a relatively constant value for the dielectric constant for the chromosomes, while it was only able to distinguish between different peptide superstructures in terms of their different phase signal. In order to get an estimate for the dielectric constant a method for characterizing the atomic force microscope (AFM) cantilever was developed. Finally, the results obtained from the EFM-phase and AFM experiments on the chromosomes were used with data obtained from dielectrophoresis manipulation of chromosomes in a fluidic system in order to determine a range for the conductivity of the chromosomes. This was done together with theoretical simulations for the trajectories of the chromosomes in the DEP field.

Dansk resumé

Mod miniaturisering af system for sortering af biologiske prøver

Målet med dette projekt er at undersøge metoder til sortering af menneskelige kromosomer og peptide strukturer. Elektrostatisk kraft mikroskopi-fase, forkortet til (EFM)-fase, blev brugt til at undersøge de dielektriske egenskaber af menneskelige kromosomer og peptide strukturer. Det blev bemærket, at EFM-fase metoden gav en forholdsvis konstant værdi for den dielektriske konstant for kromosomer, mens den kun var i stand til kvalitativ at skelne mellem forskellige peptide strukturer, i form af deres forskellige fase signal. For at få et estimat for den dielektriske konstant var det nødvendigt at udvikle en ny metode til at karakterisere den atomare kraft mikroskopi (AFM) cantilever. Endelig blev resultaterne fra EFM-fase og AFM eksperimenter på kromosomerne anvendt sammen med oplysninger fra dielektroforese manipulation af kromosomer i en fluidic system for at få estimat af ledningsevnen af kromosomer.

Preface

This thesis is submitted as a partial fulfillment of the requirements for obtaining the Ph.D. degree in applied physics from the Technical University of Denmark (DTU). This report documents my work carried out between the 1st of November 2006 and October 31th, 2009 done at the Technical University of Denmark at the Department of Micro- and Nano-technology (DTU Nanotech). The supervisors of the project were Associate Professor Winnie Edith Svendsen and Assistant Professor Maria Dimaki.

During the project some experiments were carried out with either inconclusive results or none at all. These are not included in the main part of the report but are described in short in the appendix. These were: 1) Attempts to do acoustic sorting of the chromosomes. The experiments were carried out at Lund University in Sweden, at the group of Thomas Laurell. 2) Impedance detection of the chromosomes in liquid, and 3) Attempts to use the peptide nanotubes as molds for nano sized fluidic channels.

This work was made possible through funding by the Lundbeck Foundation and by the Research Council for Technology and Production. I also worked with a lot of colleagues and students during this project, whom I would like to take the opportunity to thank here.
First of all I would like to thank my supervisors Winnie Edith Svendsen and Maria Dimaki for guidance, advise, question answering, discussion of results, proof reading, and help in general. I would also like to thank the students that I supervised during my Ph.D., in particular Jason Jensen working on the EFM scans of peptide nanotubes, Sonia Mary Buckley working on the EFM scans and DEP of chromosomes and Martin Græsvænge Hansen who worked on the imprinting and KPM of proteins.
Further, I would like to thank Kristian Mølhave for lending me parts from his setups, as well as Jacob Moresco Lange and Jaime Castillo for providing the samples.
I should not forget to thank everyone in the NaBIS group, of which I was a mem-

ber, who contributed to a great atmosphere in the labs and offices and of course my family for their support during the last 3 years. Finally, I would like to thank Tim Booth for proof reading part of the final report.

Casper Hyttel Clausen

Kgs. Lyngby, October 31th, 2009

Contents

List of Abbreviations

Abbreviation	Interpretation
μ-TAS	Micro Total Analysis Systems
C-TAS	Chromosome Total Analysis System
DEP	Dielectrophoresis
TEM	Transmission Electron Microscopy
AFM	Atomic Force Microscopy
SPM	Scanning Probe Microscopy
SFM	Scanning Force Microscopy
KPM	Kelvin Probe Force Microscopy
EFM	Electrostatic Force Microscopy
PID	Proportional–Integral–Derivative
PI	Proportional–Integral
SEM	Scanning Electron Microscopy
IgG	Immunoglobulin G
PDMS	Polydimethylsiloxane
ASE	Advanced Silicon Etch
SCCM	Standard Cubic Centimeters per Minute
PB	Phosphate-Buffer
PBS	Phosphate-Buffered Saline
PVP	Polyvinylpyrrolidone

List of Figures

List of Tables

Chapter 1

Introduction

1.1 Motivation

In recent years the in interest in using biological materials for nanotechnology applications has been increasing. One of the reason for this merge of biotechnology and nanotechnology is the possibility of using biomaterials for medical applications. As nanosized devices have the advantage of being smaller or on the same scale as living biological samples, nanotechnology is a useful tool e.g. for investigating how bacteria move inside the body or how cells respond to different drug treatments [18] etc. Further, the advantages of using biological materials in nanosized devices could lead to better biocompatibility or smarter or more advanced structure [13]. So far several reports exist on the possible use of biological self assembled structures for applications in nanotechnology [13]. Two particular examples are protein/peptide structures or chromosomes.

It has for example been shown, that peptides can self-assemble into several different super structures, such as tube-like structures with a very small diameter [19, 20, 21], or spherical objects [22]. Further, these super structures have interesting properties as it has been shown that they are biocompatible as well as easily surface functionalized [23]. These properties make them interesting candidates for using as the active part of e.g. biosensors as their surface can be functionalised specifically so as to give a measurable signal upon contact with particular molecules/cells/bacteria etc.

In order to use these structures in nanosized devices it is necessary to some of their properties. The properties necessary to know depend on the application and can be mechanical (size, Young's modulus, etc.) or electrical (charge, dielectric constant, etc.).

Material properties can be found in several ways. The most common methods

for finding the material properties involve measurements on bulk of the material, e.g. investigating how several hundred cells respond to change [24]. However, this is not always possible e.g. there is limited samples or if the size of the sample is in the nanoscale. This have given rise to extendedly research in develop existing methods capable of working in the nanoscale, as well as finding new ones [25]. For this Ph.D. project the focus is on the dielectric properties. The common method for investigating these properties is dielectric spectroscopy [26], which will be described further in this chapter.

1.1.1 μ-TAS Systems

As this Ph.D. is part of two different larger projects, a description of these two projects will be given here.

The main project this PhD is part of is called Chromosomes Total Analysis System or C-TAS. The goal of this project is to develop a micro-fluidic device, which should be able to screen for chromosomal defects, in order to easily identify patients with e.g. Downs syndrome or certain types of Leukemia [27]. The micro-fluidic device was envisioned to be able to perform all process steps used for screening for chromosomal defects:

1. Isolation and growth of the white blood cells.
2. Lysing of the white blood cells.
3. Identification and isolation of the chromosomes.
4. FISH analysis of the chromosomes.

This Ph.D. deals with the identification and isolation of chromosomes. The main question addressed by the project is whether sorting could be achieved and which method would be optimal for the purpose.

The BeNatural project was a European project focusing on the investigation of self assembled biological nanostructures, their properties and manipulation, and applications. This Ph.D. project aimed also at investigating some of the properties of these self assembled biological nanostructures, especially their electrical properties.

1.2 Background and State of the Art

The goal of this project has been to investigate the physical properties of specific biological materials. More specifically, the electrical properties of these biological samples. The driving force for this has been the use of these materials for

μ-TAS devices (see the C-TAS project) and the self-assembly of biosensors (see the BeNatural project).

Traditionally a number of methods exist for the mapping of different physical properties of samples. However, most of these methods are developed for bulk material (micro range) and not for structures on the nanoscale. In the case of the dielectric properties of materials, the most common method is dielectric spectroscopy, which is a term covering a lot of different techniques. The method utilizes either an electrical signal or an optical signal to probe the dielectric properties of the material [26]. It can be a two contact measurement or a three contact measurement on the sample. The latter is known as electrochemical impedance spectroscopy method and is mostly used on samples where ionic conduction dominates [28]. For the two contact method several ways are used to measure the dielectric properties [26]. Normally they are measured by varying the frequency of the applied signal [26]. Depending on the frequency range the applied signal is either an electrical signal or a light or electromagnetic wave [26]. At frequencies in the range 10^{-6} to 10^{7} a electrical signal is used. at higher frequencies 10^{6} to 10^{12} electromagnetic wave are used, the reason for this is that at frequencies around 10^{6} the parasitic capacitance from cables, connectors etc. start to becoming dominate [26]. The applied frequency is swept and the response is recorded [26]. The issue with this method when it comes to investigating sub micrometer structures is to get contact to them (be it electrical or optical). It is possible to contact sub micrometer structures by e.g. electron beam lithography, however, this is a slow and expensive process requiring good localization of the structures under investigation and good alignment capabilities.

One approach to measure electrical properties of nano sized objects is to investigate a lot of them between two (micro sized) contacts. This was done for example by F. Fang *et al.* [29], where gold nanoparticles made with different preparation methods were added between a set of electrodes and then the conductivity of different prepared samples was measured. The good thing about this approach is that changes in properties can rather easily be measured, however the changes to the particles need to be the same to draw any conclusions about the individual particles. Further, they need to be rather easy to manipulate in a liquid in order to place them at the electrodes. This is an issue for chromosomes and other biological samples, as they are not completely uniform as is the case for solid state samples.

Electrical investigations on biological samples are not simple due to difficulties in handling. However, some work has been done on mainly cells. For example, D. Holmes *et al.* [30], performed impedance measurements on different white blood cells (monocytes, neutrophils, T-lymphocytes), using a micro-fluidic sys-

tem with electrodes in the channel. For samples that are smaller in size than cells other measurement techniques are needed.

For samples with dimensions on the nanoscale electron microscopy or probe microscopy are interesting and relevant techniques as they offer the resolution needed to investigate single samples in this range [31, 32]. These techniques are usually used for gaining topographical information. However, technological advances have made it possible to measure much more than just the geometrical characteristics of various particles. Some examples are surface charge, magnetic properties, thermal properties and surface conductance.

Due to the fact that the biological material considered in this project was highly inhomogeneous in terms of geometry and composition, the investigation method chosen was one that could address and measure on individual particles. More specifically, different kinds of scanning probe microscopy (SPM) techniques were utilized. At the time of this project both SPM equipment and SEM equipment was available at the department. The reason for choosing SPM over SEM was that it is a much more versatile method as it has more options, being able to probe a variety of physical properties, e.g. thermal, magnetic, electrical and mechanical [33]. Furthermore, even though SEM can be used to investigate the electrical properties of samples, its selection of options for doing this is limited compared to SPM [34]. Special treatment of the samples are also normally needed for SEM investigations [31], as the samples need to be completely dry and degassed and preferably conducting for achieving good images. SPM on the other hand can work under most conditions, including in liquid [35].

The ability of SPM to probe a single particle is good in terms of sample inhomogeneity. However, the disadvantage is that the method is slow and it can take a long time to get any statistical information [31, 32].

The abbreviation SPM covers several techniques which can be used to investigate electrical properties of nanoscales. All these are collectively described with the term electrostatic force microscopy (EFM) [36]. Over the years, since the first report on EFM was published in 1991 by M. Nonnenmacher *et al.* [37], many different techniques have been developed, such as Kelvin Probe Microscopy (KPM), and Scanning Conductance Microscopy (SCM) [38], also called EFM-phase [39]. The first report on KPM [37] describes the measurement of the contact potential difference between gold, platinum, and palladium. The authors [37] state that they were able to distinguish between the different materials but no quantitative value could be extracted which fitted with other measurement of the contact potential between these metals. More recently E. Mikamo-Satoh *et al.* [40] used KPM microscopy to investigate double-stranded DNA. Their result shows that

they can distingue isolated DNA from tangled DNA based on the electrostatic response. The other major EFM method, EFM-phase, is named so because it uses the phase of the vibration of the cantilever as the signal readout. The earliest reports on this method are from around 2000 [38] where M. Bockrath *et al.* tried to use the method to get an estimate of the conductivity of single walled carbon nanotubes. Further work done by C. Staii *et al.* [41] used the method for quantitative analysis of polymer wires. Specifically they used the method to distinguish between conducting and non-conducting wires, as well as estimate the dielectric constant for the non-conducting wires. Their results were in agreement with existing data [41]. T. S. Jespersen *et al.* [39] used the method to quantitatively estimate electrons trapped by single walled carbon nanotubes dispersed on a surface. Further, the same group later used the same method to map the positions of single walled carbon nanotubes embedded in a polymer [1]. They spin coated poly-methylmethacrylate containing the single walled carbon nanotubes on a substrate.

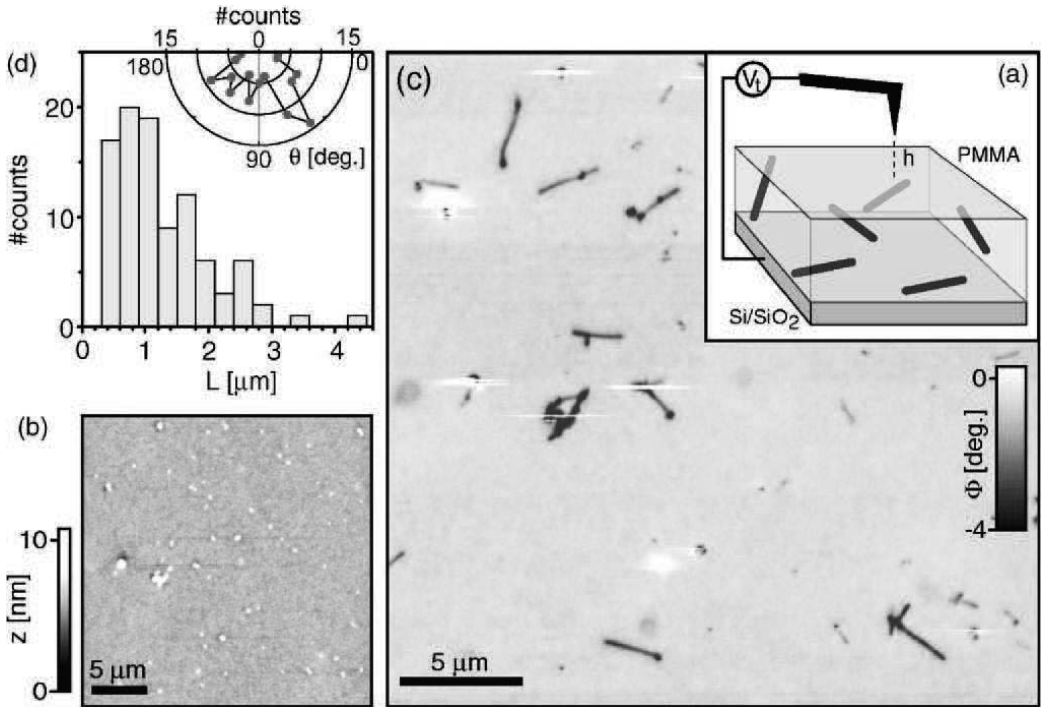

Figure 1.1: Figure from [1]: A schematic drawing of the setup, B topography of the surface of the spined polymer C EFM-phase image of B, D distribution of the orientation of the carbon nanotubes in the polymer.

Figure 1.1 A shows a schematic drawing of the setup. Figure 1.1 B shows the topography of the spin coated polymer film, while figure 1.1 C shows the EFM-phase image. Figure 1.1 D shows the angular distribution of the carbon nanotubes

in polymer which is attributed to the spinning process. As can be seen from comparing the images in figure 1.1 B and C it seems that darker areas appear in the EFM-phase image but not in the topography image. This is interpreted as being the single walled carbon nanotubes in the polymer, as earlier reports shows that the tubes appear dark in the phase image [38, 39]. This indicates that this method is a powerful tool for investigating composite samples on sub-micrometer scale, something mostly Transmission Electron Microscopy (TEM) was capable of doing [31].

A lot of work has also been put into the pros and cons of the two different techniques, e.g. G. Koley *et al.* [2] show that the signal potential on the cantilever, when using the KPM technique, is heavily influenced by other potentials nearby, not just under the cantilever tip. Their setup consisted of two sets of interdigitated electrodes next to each other with known potentials applied to them (one at 0, the other at 5 V), as shown in figure 1.2.

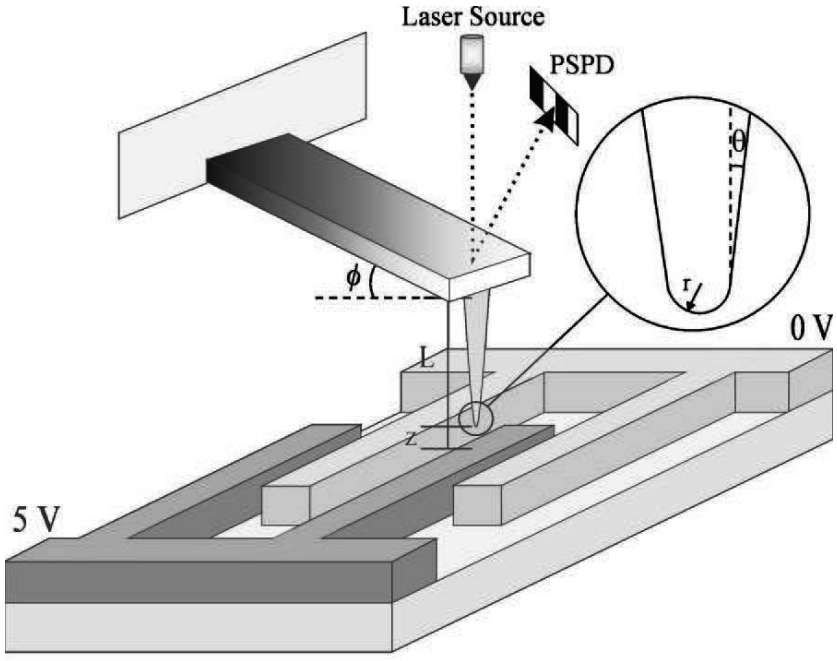

Figure 1.2: Figure from [2], schematic drawing of the setup, consisting of an interdigitated array of electrodes with different potentials. The tip distance from the surface is varied and the potential response is measured.

The tip is placed over one of the electrodes with 5 V applied between the two electrodes and the distance from the electrode is varied and the change in the potential response is measured as shown in figure 1.3.

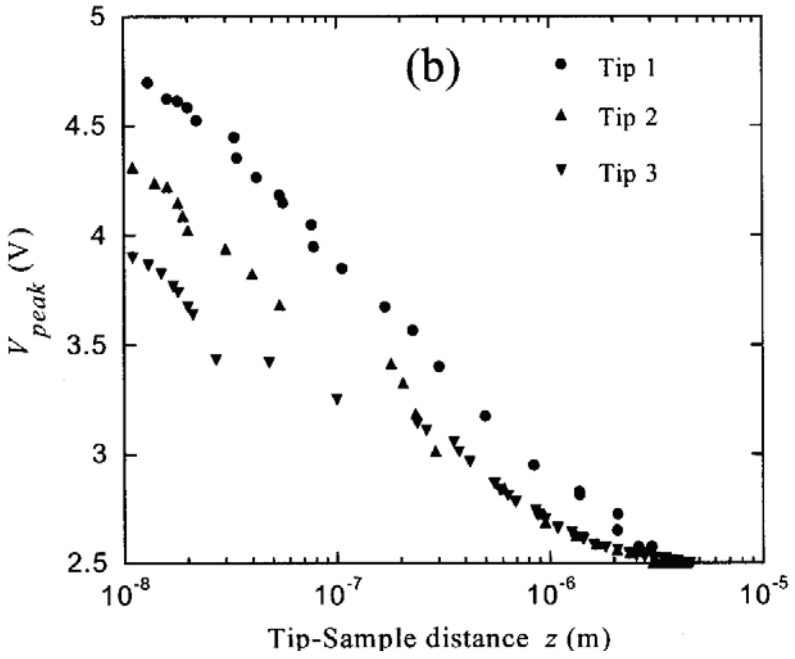

Figure 1.3: Figure from [2], shows the potential on three different cantilevers as a function of the tip electrode distance.

As figure 1.3 shows, the potential decreases as the tip moves away from the surface. Further, the figure also shows that the measured potential varies depending on the tip used, and none of them measures the right value of the potential (which was 5 V). Another report on the differences between the two methods is e.g. work done be J. Colchero *et al.* [42], where the authors treat the difference between the two methods theoretically and practically and arrive to the conclusion that the EFM-phase method is less influenced by nearby potentials compared to the KPM method.

1.3 Aim of the project

During the course of this project a number of goals were set:

1. Apply different scanning probe techniques on human chromosomes. This was done in order to investigate their dielectric properties to see if they were suited for dielectrophoresis sorting.

2. Apply different scanning probe techniques on different peptide structures. This was done in order to check if the same information could be obtained as from the chromosomes.

3. Investigate the dielectrophoretic properties of chromosomes in order to check if the dielectrophoresis effect could be used for manipulating chromosomes.

1.4 Manipulation

As mentioned earlier part of this Ph.D. was financed by the C-TAS, where one of the goals was to investigate different manipulation methods for the possible sorting of human chromosomes in a micro-fluidic setup. For this reason a pre-study was made of three common sorting methods for used in micro-fluidic systems.

1.4.1 Dielectrophoresis

Dielectrophoresis is the movement of particles in an inhomogeneous electrical field, due to polarization of the particles. As such, the important parameters controlling the process besides the shape and size of the particles are the properties of the electrical field and how the medium and particles polarize [43, 44].

In order to obtain an inhomogeneous field several things can be done; the most simple way is to apply a DC field on two planar electrodes. The geometry of the electrodes needs to be such, so that the field they create is inhomogeneous [43, 44]. Although DEP occurs with DC fields it is more common to use AC fields instead. The advantage of the AC field is the frequency dependency of the force on the particles both in terms of amplitude and in terms of direction. The method has been used in several LOC systems and requires normally the presence of one or more pairs of electrodes in micro-fluidic channels. The direction of the dielectrophoresis force, $\bar{F}_{DEP}(\bar{r})$ [43], depends on how polarizable the particle is relative to the medium. In an electrical field if the particle is more polarizable than the medium (figure 1.4 A) the surface of the particle will contain more charges than the medium and the net charge of the particle and the surrounding medium will look like the situation in figure 1.4 C. Here the polarization of the particle gives rise to a force between the charged surface of the particles and that of the electrodes, and as the charge on the particle is uniform the particle will move towards areas with the higher electric field. Figure 1.4 B shows the opposite situation, where the particle is less polarizable than the medium. Here the polarization is the opposite (figure 1.4 B), which gives rise to a force in the opposite direction [43].

The dielectrophoresis force ($\bar{F}_{DEP}(\bar{r})$) on a particle with an induced dipole is given as [45]

$$\bar{F}_{DEP} = (\bar{p}_e \nabla)\bar{E}(\bar{r}), \tag{1.1}$$

where $\bar{p}_e$ is the induced dipole moment of the particle and $\bar{E}(\bar{r})$ is the electrical

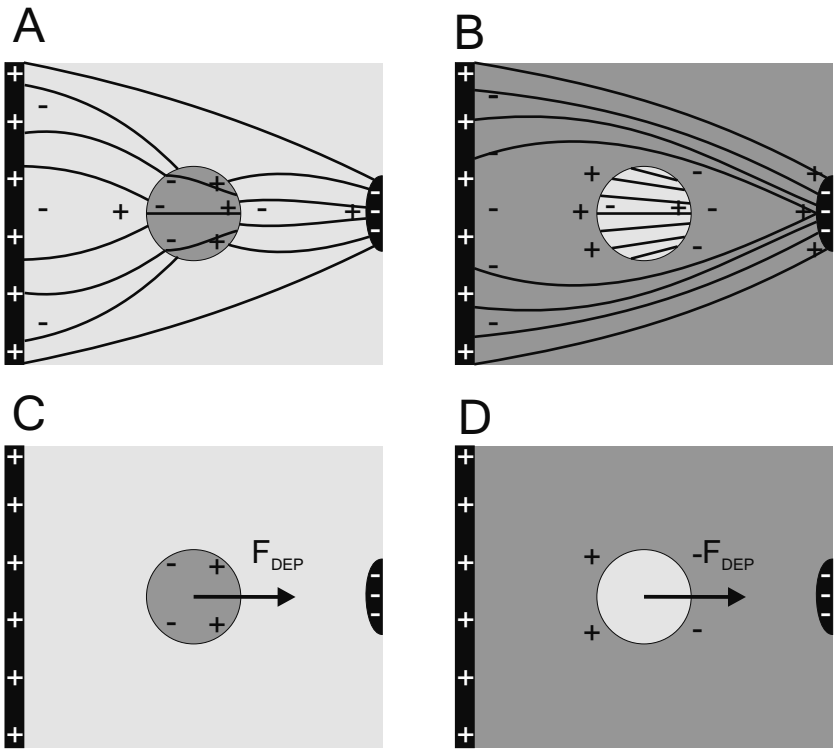

Figure 1.4: Schematic representation of the polarization of particle and medium for the case where the particle is more polarizable than the medium (A) and where the medium is more polarizable than the particle (B). In (C) the net charge on the particle is shown as a result of the situation in (A) as well the direction of the dielectrophoresis force, while in (D) the same is shown for the situation in (B).

field at the position $\bar{r}$. The induced dipole moment can be described as [46]

$$\bar{p}_e = v_p u_m \bar{E}(\bar{r}), \tag{1.2}$$

where v_p is the volume of the particle and u_m is the effective polarisability. Substituting equation 1.2 into equation 1.1 and using that the curl of the electrical field is zero ($\nabla \times \bar{E} = 0$) as well as product rules for vectors [45] the dielectrophoresis force becomes

$$\bar{F}_{DEP} = v_p u_m \nabla (\bar{E}(\bar{r}))^2. \tag{1.3}$$

According to [46] the effective polarisability can be written as

$$u_m = \epsilon_m Re\{f_{CM}(\epsilon_m^*, \epsilon_p^*)\}, \tag{1.4}$$

where ϵ_m is the permittivity of the medium and $f_{CM}(\epsilon_m^*, \epsilon_p^*)$ is the Clausius-Mossotti factor, which depends on the complex permittivity of the particle and the medium, ϵ_p^* and ϵ_m^* respectively, the geometry of the particle, and the frequency

of the electric field. Using this in equation 1.3 one gets the dielectrophoresis force as

$$\bar{F}_{DEP}(\bar{r}) = \epsilon_m \mathrm{Re}\{f_{CM}(\epsilon_m^*, \epsilon_p^*)\}\Gamma\nabla(\bar{E}(\bar{r}))^2, \tag{1.5}$$

where $\Gamma = v_p$ a parameter that depends on the geometry of the particle. Further ϵ_m^* and ϵ_p^* are given as

$$\epsilon_{m,p}^* = \epsilon_{m,p} - i\frac{\sigma_{m,p}}{\omega}, \tag{1.6}$$

where $\sigma_{m,p}$ is the conductivity of the medium/particle and ω is the angular frequency of the electrical field. The only parameter which determines if the force on the object in question is negative or positive is $Re\{f_{CM}(\epsilon_m^*, \epsilon_p^*)\}$, as the sign of this parameter is determined by the relative polarisabilities of the particle and the medium. If the medium is more polarizable then the particle will move away from the regions with a high electric field, which are usually the electrode edges. This is named negative DEP. The opposite effect is called positive DEP [47]. The majority of particles can experience both positive and negative DEP, depending on the frequency of the electric field. The turnover frequency differs from particle to particle (depends on among other things the permittivity and as well as the conductivity of both particle and medium) which enables the sorting of particles by DEP. This is why the majority of reports on DEP for manipulation of particles use an AC field, as one can rather easily change the frequency of the field. This project focuses on the sorting of biological structures whose shape resemble cylinders. In this case the Clausius-Mossotti factor can be approximated by that of a prolate ellipsoid [46]

$$f_{CM} = \frac{\epsilon_p^* - \epsilon_m^*}{(\epsilon_p^* - \epsilon_m^*)A_z + \epsilon_m^*}, \tag{1.7}$$

where A_z is a factor depending on the geometry of the ellipse given as [43, 46]

$$A_z = \frac{1}{2}a_1a_2a_3\int_0^\infty \frac{ds}{(s+a_z^2)\sqrt{(s+a_1^2)\cdot(s+a_2^2)\cdot(s+a_3^2)}}, \tag{1.8}$$

where the subscript z determines the axis of alignment of the particle and a_1, a_2, a_3 are the half axis of the ellipse. Using that the volume of an ellipsoid is $\frac{4\pi a_1a_2a_3}{3}$, Γ for a ellipsoid becomes [47]

$$\Gamma = \frac{\pi a_1a_2a_3}{3}. \tag{1.9}$$

Other things to take into consideration are forces acting on the particle besides the electrical one. The viscous drag or force could be a factor to take into account. This force is dependent on the velocity of the particle with respect to velocity of the liquid [48]. Further, the electrical field also gives rise to Joule heating of the

liquid, which might cause the liquid to move making the modeling the trajectories of the particle rather difficult. Further if the particles are fragile, they could be damaged by the DEP force [49]. if trapping with positive DEP is the goal one has to be aware that if the particle spans the electrodes, current will flow between the electrodes through the particle and heat will be deposited in the particles, which might damage them.

A challenge with biological samples is that their structures are rather complex, which can make it difficult to come up with a valid estimate of an optimal solution based on the theory. Another thing to consider is that the geometry (gap, size, and shape) of the electrodes needs to be optimized in order obtain the desired result. The advantage of DEP is that no pretreatment of the sample is needed. and that the electrodes are rather easy to fabricate. Further the method has been successfully applied to trap complex biological structures such as bacterial chromosomes [4] and cells [50].

The most common electrode design is two sharp tips separated by a few μm, as they provide a rather high and highly inhomogeneous electrical field in the gap making it easier to perform the experiment. Figure 1.5 shows a simulation of the electrical field between two sharp electrodes. As it can be seen the field is higher at the tip of the sharp electrodes. Another type of electrodes used is the parallel type, with two electrodes shaped like lines opposite to each other. This type has the advantage that a lot more of the sample can be trapped than in the case case for the sharp electrodes.

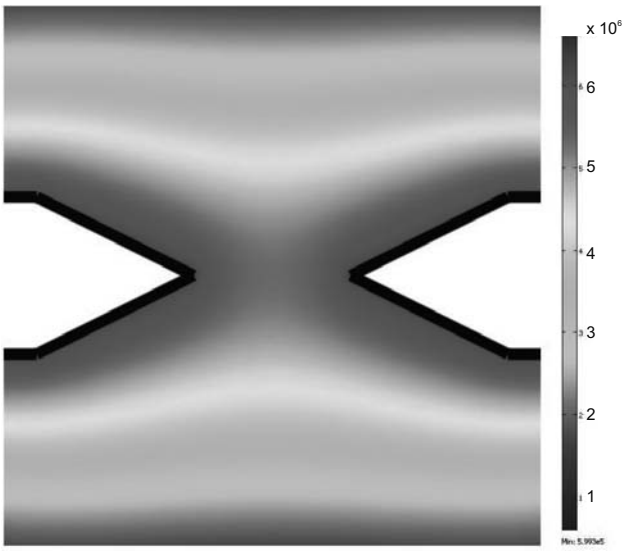

Figure 1.5: Simulation of the electrical field between two sharp electrodes done with Comsol Multiphysics software$^{\mathrm{tm}}$ (the white tips are the electrodes).

DEP has over the years been used for several different LOC applications as it is easy to implement electrodes on a micro-system. Its applications range from manipulation of beads or cells [5, 51, 52] to trapping bacterial chromosomes [4]. The majority of reports on DEP focus on trapping of the particles such as the work done by R. Krupke *et al.* [3] where single-walled carbon nanotubes with different properties (metallic and semi-conducting) were sorted by trapping of the metallic ones with parallel electrodes (figure 1.6 A). C. Prinz *et al.* [4] made a combined device for lysing Escherichia coli cells and trapping of the released chromosomes. The principle is shown in figure 1.6 B. This was realized by defining the electrodes on a silicon wafer and making the channels in PDMS as done described by D. C. Duffy *et al.* [53]. B. G. Hawkins *et al.* [5] used DEP for continuous sorting, where the principle was that coherently shaped barriers (see figure 1.6 C) between the electrodes in the flow channel caused the electrical field to deflect the particles to different parts of the channel. These two parts were held together by a holder which also contained the inlets. Others have attempted to increase the trapping of the particles by adding floating electrodes or points in the gap as shown in figure 1.6 D [6], [54].

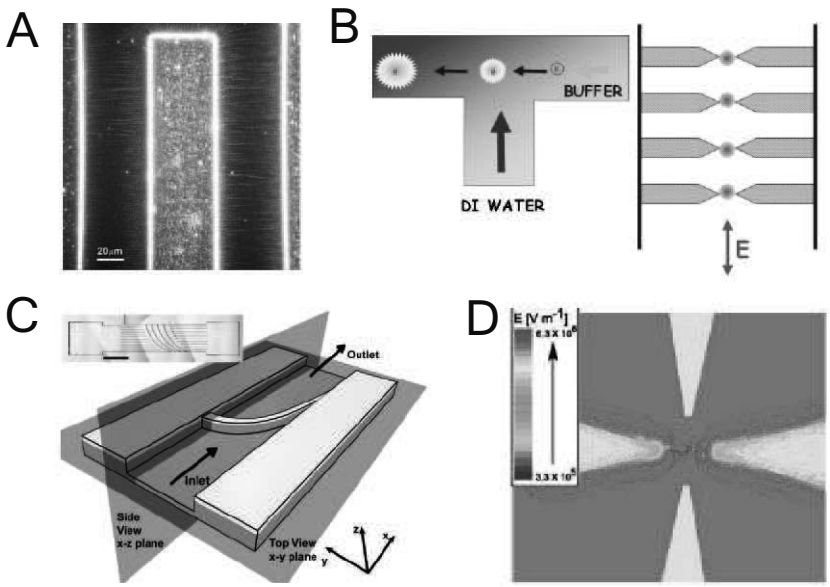

Figure 1.6: A) Optical image of trapped metallic carbon nanotubes, from [3]; B) Schematic drawing of the principle of cell lyses and chromosomes, from [4]; C) The curve barrier in the channel causes the electrical field to have changing gradient along the barriers, from [5]; D) Simulation of the electrical field between two electrodes with floating electrode points added in the gap, from [6].

1.4.2 Acoustic Sorting

The principle behind sorting using acoustic waves is that an external applied force on the micro-fluidic chip gives rise to (standing) waves in the fluidic channels. This can be done in several ways, but the most common procedure is to glue a piezo element on a microchip with channels for fluidics embedded in it [8]. The piezo element in operation generates waves which make a force on the particle leading them to different nodes. This force is due to a pressure gradient (see figure 1.7).

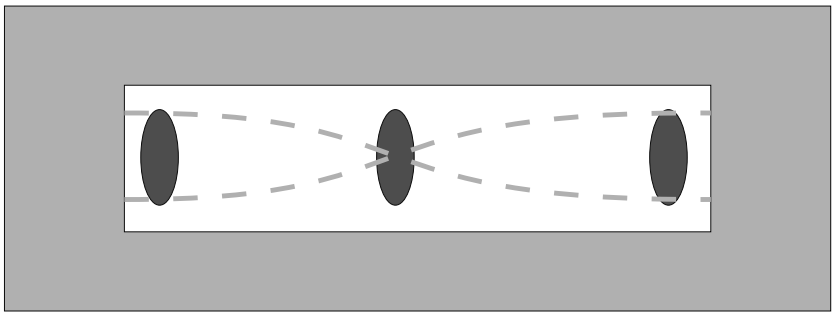

Figure 1.7: Schematic drawing of a channel cross-section showing the first standing wave (the grey dashed line) The dark grey bulbs define the nodes and antinodes where particles will be trapped.

For standing waves in the channel the formula for the pressure $p(x)$ in the channel in the direction orthogonal to the channel length is given by [55]

$$p(x) = p_0 \sin(kx) \sin(\omega t), \tag{1.10}$$

where p_0 is the acoustic pressure amplitude, k is the wave number, x is the distance from the nodal point, ω is the angular frequency, and t is the time. In order to calculate the acoustic radiation force on a particle the acoustic energy, U_a, is needed. According to G. Whitworth *et al.* [56] the acoustic energy is given as

$$U_a = -V_p B_{pm} \langle KE \rangle + V_p (1 - \frac{\gamma_p}{\gamma_m}) \langle PE \rangle, \tag{1.11}$$

where V_p is the volume of the particle, B_{pm} is a parameter that depends on the geometry of the particle as well as on the density of the medium and particle, $\langle KE \rangle$ is the time-averaged kinetic energy density, γ_m and γ_p is the compressibility of the medium and the particle respectively, and $\langle PE \rangle$ is the time-averaged potential energy density. According to [56] the kinetic energy density, KE, is given as

$$KE = \frac{(\int \nabla p(x) dt)^2}{2\rho_m}, \tag{1.12}$$

where ρ_m is the density of the medium. Using equation 1.10 one gets

$$KE = \frac{p_0^2}{2\rho_m}(\int \nabla \sin(\omega t)\sin(kx)dt)^2 = \frac{p_0^2 k^2}{2\omega^2\rho_m}\cos(\omega t)^2\cos(kx)^2. \quad (1.13)$$

The potential energy density is given as [56]

$$PE = \frac{p(x)^2\gamma_m}{2} = \frac{p_0^2\gamma_m}{2}\sin(\omega t)^2\sin(kx)^2. \quad (1.14)$$

As both equations 1.13 and 1.14 contain either a $\sin(\omega t)^2$ or a $\cos(\omega t)^2$ part the time-averaged kinetic and potential energy densities will be

$$\langle KE\rangle = \frac{p_0^2 k^2}{4\omega^2\rho_m}\cos(kx)^2, \quad (1.15)$$

$$\langle PE\rangle = \frac{p_0^2\gamma_m}{4}\sin(kx)^2, \quad (1.16)$$

as $\frac{1}{T_0}\int_0^{T_0}\sin(\omega t)^2 dt = \frac{1}{T_0}\int_0^{T_0}\cos(\omega t)^2 dt = \frac{1}{2}$, where $T_0 = \frac{2\pi}{\omega}$. Inserting equations 1.15 and 1.16 into equation 1.11 gives

$$U_a = -V_p B_{pm}\frac{p_0^2 k^2}{4\omega^2\rho_m}\cos(kx)^2 + V_p(1-\frac{\gamma_p}{\gamma_m})\frac{p_0^2\gamma_m}{4}\sin(kx)^2. \quad (1.17)$$

The acoustic radiation force, F_a, is given as

$$F_a = -\nabla U_a, \quad (1.18)$$

so inserting equation 1.17 into 1.18 gives

$$F_a = \nabla\Big(V_p B_{pm}\frac{p_0^2 k^2}{4\omega^2\rho_m}\cos(kx)^2 - V_p(1-\frac{\gamma_p}{\gamma_m})\frac{p_0^2\gamma_m}{4}\sin(kx)^2\Big) =$$

$$F_a = \frac{V_p p_0^2 k\gamma_m}{4}\sin 2kx\Big(\frac{k^2 B_{pm}}{\omega^2\rho_m\gamma_m} + 1 - \frac{\gamma_p}{\gamma_m}\Big). \quad (1.19)$$

The compressibility of the medium can be written as $\gamma_m = \frac{1}{c_m^2\rho_m}$ and k is equal to $k = \frac{2\pi}{\lambda_m} = \frac{\omega}{c_m}$, where c_m is the characteristic speed of the waves in the medium and λ_m is the wavelength. So using these expressions equation 1.19 can be rewritten as [56]

$$F_a = \frac{V_p p_0^2 k\gamma_m}{4}\sin 2kx\Big(B_{pm} + 1 - \frac{\gamma_p}{\gamma_m}\Big). \quad (1.20)$$

The factor $B_{pm} + 1 - \frac{\gamma_p}{\gamma_m}$ depends on the density of both the particle and the medium as well as the compressibility and for the acoustic force to act on the particles it is required that this function is not zero. This factor can be used to engineer if the particle trapping occurs in the nodes or antinodes by use of different fluidics.

One of the advantages of acoustic sorting is that the force on the particles is constant and as such diffusion of the particles can be neglected [57]. Another force to consider since the particles cluster at the nodes and antinodes is inter particle repulsion. The result of this is that if the particle concentration is too high the sorting effectiveness decreases [57]. Another important requirement is that the particle diameter must be less that half of the acoustic wavelength, or else the acoustic force will act in more that one direction [8]. As the waves can generate considerable forces damage of fragile particles is not uncommon. The generation of the waves also creates irradiation, which will heat the system, something that could cause changes to particles sensitive to heat [55]. Moreover the transmitting of the energy for generating the standing waves is a concern, which limits the choice of material if a high effect is important [57]. In this case only ”rigid” materials can be used making the fabrication more complicated. The ultrasound might also enhance the degradation of polymers, thus limiting the lifespan of this type of device [58]. The method has never been tested on chromosomes or other elongated objects. In terms of fabrication two types of system designs seem to be successful so far. In the first type made by Kapishnikov *et al.* [7] the channels and cavities for the piezo elements were fabricated by using SU-8 molds in PDMS [53], which was subsequently bonded to a glass surface. Figure 1.8 A shows the layout of the system. As it can be seen the piezo elements are placed on each side of the channel, which makes the area there rigid enough for standing waves to occur.

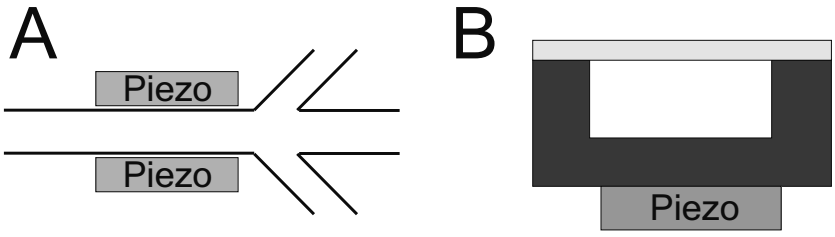

Figure 1.8: Schematic draw of two different acoustic systems, A)top drawing of the device made by S. Kapishnikov *et al.* [7] B) cross section drawing of the device made by A. Nilsson *et al.* [8].

Figure 1.8 B shows a cross sectional drawing of the other type of device developed by A. Nilsson *et al.* [8]. In this system the channels are made in silicon with a glass lid. Due to the fact that the whole setup is fabricated in a rigid material A. Nilsson *et al.* do not have to integrate the piezo element into their design as silicon can transmit the waves without too much loss. The advantage of the first type of device is that it can be used together with an inverted microscope (which is the type of microscope normally used when investigating biological samples and especially chromosomes). It is therefore simpler and faster to fabricate. The disadvantage is that it needs two piezo elements. The opposite is the case for the

second type of devices.

Acoustic standing waves have been successfully used to sort beads with different size [7] with the device shown in figure 1.8 A. Also F. Petersson *et al.* [9] made a rigid device in silicon (figure 1.9 A) and sorted blood cells from lipid particles in blood without damaging them. Further M. Evander *et al.* [10] placed piezo elements in channel crossings and so obtained an acoustic force density which gives rise to nodes in both channel directions. This creates ”wells” in the force density where particles can be trapped (see figure 1.9 B). The system was used in order to trap cells and keep them alive by slowly changing the cell medium continuously.

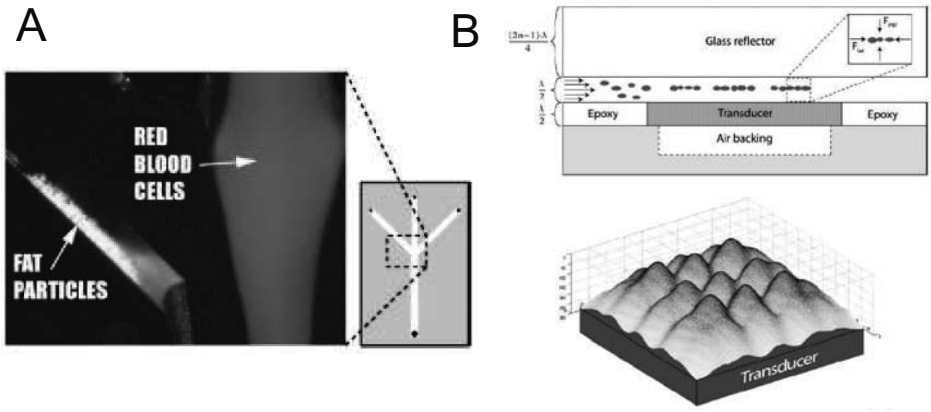

Figure 1.9: A) Optical image of sorting of human lipid from human erythrocytes with acoustic forces from [9] B) Schematic drawing of the principle of the microfluidic system as well plotted pressure distribution for the trapping cells from [10].

1.4.3 Bumper Array

The idea to use asymmetric patterns of pillars to sort particles in a liquid (called bumper or post arrays) was suggested and demonstrated by L. R. Huang *et al.* [59]. The principle is that the particles follow the flow lines which get separated when passing the bumps depending on the geometry. The principle is shown in figure 1.10.

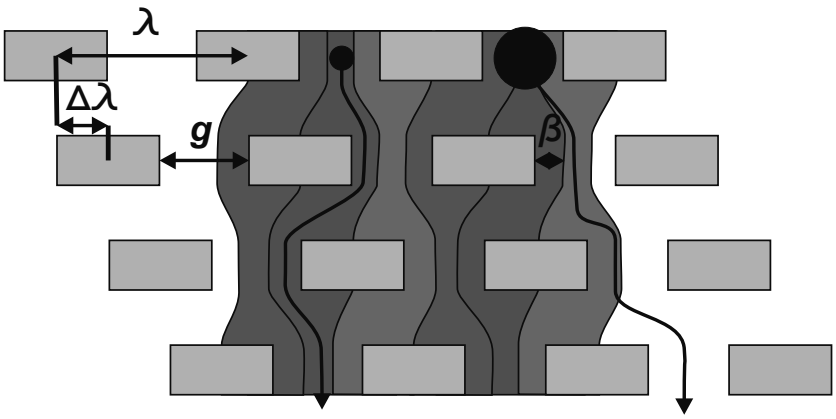

Figure 1.10: Schematic drawing of the principle in bumper array sorting. The colored areas symbolize different flow streams, and the black circles different particles. As it can been seen the large particle moves to the right due to the fact that its center of mass is in a different flow stream while the smaller one only follows one stream.

The colored areas in figure 1.10 represent different flow streams, while the black circles symbolize particles with different sizes. Only three flow streams are sketched for simplicity. The large particles move to the right because a larger part of them is in flow streams which pull it to the right, while the smaller particles only follow one flow stream so they pass through the system unaffected by the bumpers. The parameters which describe the sorting properties of the array are the distance between the posts orthogonal to the flow direction, λ, the size of the gap between two neighboring posts, g, and ϵ which determines the displacement between the orthogonal post arrays (see figure 1.10) and is given as $\epsilon = \frac{\Delta\lambda}{\lambda}$, where $\Delta\lambda$ is the shift of the next array. To describe the maximum size of a particle which will "zigzag" though the arrays (as the small particle in figure 1.10), D_m (the diameter of the particle), the parameter β, describing the length of the flow profile which stays in the center (see figure 1.10) is used. In order for the particle to stay in the center $D_m < 2\beta$ or, expressed by the design parameters [11], $D_m < 2\eta g\epsilon$, where η is a variable parameter which accommodates for the fact that the flow is not uniform though the gap. If it is assumed that the shape of the flow profile between two posts is parabolic, a good assumption as the flow is normally laminar [48], then the velocity profile $u(x)$ between two neighboring pillars can be written as

[60]

$$u(x) = \frac{g^2}{4} - \left(x - \frac{g}{2}\right)^2. \tag{1.21}$$

As β is defined as the width of the displaced flow then

$$\int_0^{\beta} u(x)dx = \epsilon \int_0^{g} u(x)dx. \tag{1.22}$$

Solving this equation one gets

$$-\frac{\beta^3}{3} + \frac{g\beta^2}{2} = \epsilon\frac{g^3}{6} \tag{1.23}$$

or

$$\left(\frac{\beta}{g}\right)^3 - \left(\frac{3}{2}\frac{\beta}{g}\right)^2 + \epsilon\frac{1}{2} = 0. \tag{1.24}$$

Using $2\beta \approx D_m$ solving equation 1.24 and plotting $\frac{D_m}{g}$ vs. ϵ one gets the curve of figure 1.11 A. Using $\beta \approx \eta g\epsilon$ solving equation 1.24 and plotting η vs. ϵ, one gets the curve of figure 1.11 B. Both figures are plotted from 0 to 0.5 as larger values (0.5 to 1) would just be a repetition due to symmetry.

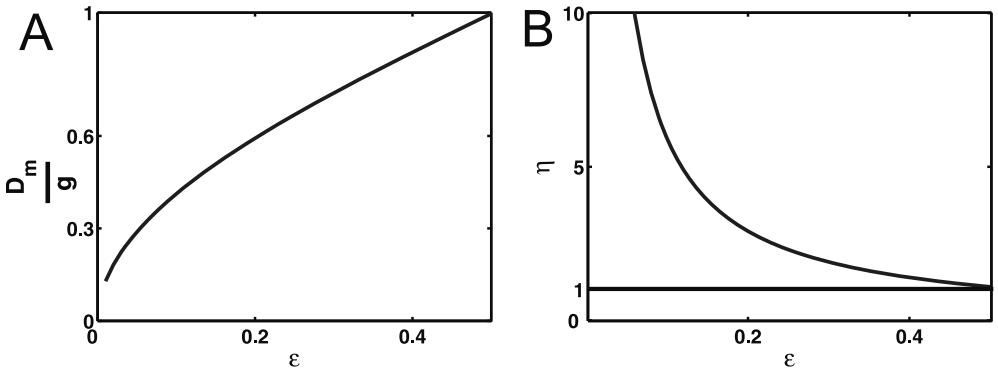

Figure 1.11: A) maximum particle size divided by gap size as a function of displacement between the orthogonal post arrays; B) Size of nonuniform flow though the gap (η) as a function of displacement between the orthogonal post arrays.

It can be seen from figure 1.11 A that for a fixed gap size the maximum size of the particle for "zigzag" movement in the system follows ϵ. It can be seen that D_m can be tuned for a fixed g or ϵ. This means that rather big or small variations in particle size can be sorted, making this method versatile when it comes to designing the device. Figure 1.11 B shows the size of the nonuniform flow parameter ($\eta(\epsilon)$) as a function of the relative displacement between the orthogonal post arrays. It shows that for large values of ϵ this parameter can be neglected but for low values of ϵ it is dominant compared to ϵ. As $D_m = 2\eta g\epsilon$ and the figure 1.11

B does not show a linear dependence of η on ϵ the value of D_m does not depend linearly on ϵ at low values.

The flow velocity of the system needs to be high in order to minimize diffusion of particles from the different streams [59]. The advantage of the bumper array is that as it is flow driven it can work without any electrical fields, laser, or other external forces. This makes this method interesting as a micro-fluidic flow system can be driven by either a battery (electroosmotic flow) or by a pump making the method optimal for the so called point of care testing systems. J. D. Davis *et al.* [11] succeeded in sorting blood components (red and white blood cells and platelets) by fabricating an array with varying ϵ from 0.04 to 0.4 which resulted in that the device first sorted the smallest particles from the rest, while further into the device the sorting of the larger particles took place due to the increase in ϵ (see figure 1.12 A). J. D. Davis *et al.* [11] also made a device that filters the cells out of the blood and into a buffer in order to be able to study the plasma. The device consists besides the array also of a serpentine structure which is connected to the array as shown in figure 1.12 B. The blood is injected into the array while the serpentine structure has buffer injected. The array is designed so that it leads the cells in the blood into the serpentine structure, separating it from the blood plasma. Further L. R. Huang *et al.* [59] also sorted bacterial chromosomes (Escherichia coli) (they act as soft spheres) with an array with varying ϵ.

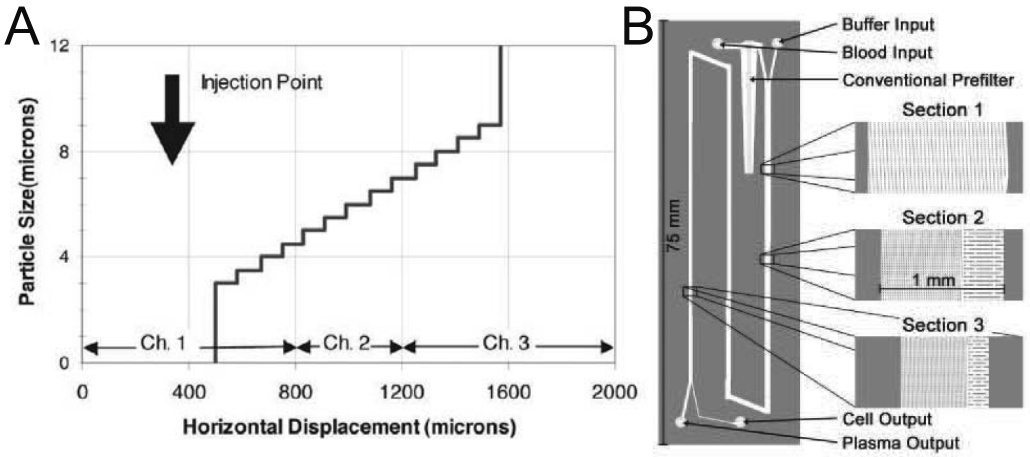

Figure 1.12: A) Graph of the predicted input-output curve with a variation of 13 different ϵ; B) Image of array connected with a serpentine structure for sorting cells from blood plasma from [11].

As this sorting method is rather new, only limited research has been done in order to test which type of particles this method works on. The method has been shown to be able to sort beads with diameters of 0.8 μm, 0.9 μm, and 1.03 μm successfully [59], indicating that this method is rather sensitive to size. D. W.

Inglis *et al.* [60] optimized the parameters of the arrays and were able to sort beads with size of 2.3 μm from 16 μm without clogging the system. Further if a lot of particles need to be sorted, a long channel is needed in order to get sufficient separation. This might limit the resolution as diffusion will play a significant role in a longer design [60]. For this work the challenge with the bumper arrays is to see if they can be used to sort cylinder-like objects as chromosomes are. Cylindrical objects will most likely get a complex motion pattern from bouncing on the posts, which will both disturb the flow through the posts as well as make modeling rather difficult.

1.5 Summary

The three methods of sorting discussed in this chapter have different potentials as the choice for sorting of the samples. First the sensitivity of the methods is different. All of them should in theory be able to separate micro sized particles with a variation of hundred nanometers in size.

Reports published on the acoustic method have mostly succeeded in separating samples with very different properties (e.g. blood cells and lipids particles, but not different types of blood cells [57]). Further, while the acoustic force on the particles (equation 1.20) depends on the properties of the medium, the majority of the parameters controlling it are the properties of the particles that need to be separated. This gives little room for optimization of any process as the method's ability to separate particles depends mostly on the particles properties. Further the acoustic method lacks experimental proof of separation of similar particles, which reduces the chances of its success with chromosomes significantly. So, to summarize the acoustic method it is a good way to sort particles with different material properties but not that good for separating particles based on their size.

The reports published on the bumper array show that it has very good sorting ability when it comes to round beads (with a variation in diameter of hundreds of nanometers [59]). However, the systems are notorious for being easily clogged. This is definitely an issue with solutions containing biological material e.g. chromosomes as they contain cell debris. Furthermore, at the moment no data exists on how bumper array systems function with soft cylindrical objects, which makes the method not an optimal choice for the sorting of chromosomes. For these reasons the bumper array does not seem an optimal choice. To summarize the bumper array method is good for sorting particles with different sizes as long as they are round, so to sum up the arrays give rise to clogging.

Last the DEP method is more versatile compared to the two others. First while the resolution of separation of particles might not be as good as for the bumper

array it is possible to tune the direction of the force by changing the frequency (equation 1.5). Using an optimal frequency Y. Li *et al.* [61] was able to separate live and dead yeast cells, which are rather similar in size and properties, making the DEP method an interesting choice as the sorting method to investigate. So, to summarize the DEP method, it is a good method for sorting a wide variety of particles, which was why this method was chosen for further investigation.

For optimization of a sorting device theoretical work is needed. From equations 1.5 and 1.7 it can be seen that the parameters determining the dielectrophoretic behavior of particles are the dielectric constant and conductivity of the particles. Therefore estimates for these parameters are needed. For this investigation two separate approaches will be used. First electrostatic investigation will be done with different Scanning Probe Microscopy (SPM) methods. More specifically analysis of the electric force and phase shift in combination with topography imaging will be done in order to get an estimate of the dielectric properties of the samples under investigation. Secondly micro fluidic systems will be used to estimate the conductivity of the samples based on dielectrophoretic measurements.

1.6 Samples

This section contains a short description of the samples used in this project. The main type of samples investigated were human chromosomes (from the C-TAS project) and self assembled dipeptide structures (from the BeNatural project). The type of samples that was investigated was Immunoglobulin G proteins as they were available in the labs.

1.6.1 Chromosomes

Chromosomes are interesting as they contain a very complex architecture of DNA and proteins, and chromosomal abnormalities may results in diseases such as Turner Syndrome and leukaemia among other [62, 63].

Chromosomes consist of DNA and proteins, and determine the properties of living organisms. DNA or deoxyribonucleic acid is a molecule which acts as an organic chain polymer. The DNA chain consists of aromatic bases and sugar and phosphate groups. The sugar and the phosphate groups make up the ”backbone” of the chain while the bases are attached to the sugar [64].

In order to manage the DNA cells make use of several different proteins. The proteins are used for several different jobs e.g. packing, repairing, and copying the DNA in the cells. The special properties of these proteins are that they recognize different parts of the helix by different means. This includes a specific

base pair sequence, local twist of the backbone structure, and specific base hydrogen bonding. An example of protein-DNA interaction is chromosomes. They are mostly made up of DNA together with proteins called histones. The primary role of histones is to organize the DNA with respect to packaging and ordering. Their impact is especially apparent during cell division when the DNA is copied packed into the well-known X-shaped structures, which can be cargoed to the two daughter cells. The genomes of all animals are divided up into a characteristic number of chromosomes. This number is called the diploid (or 2n) number. These chromosomes occur as homologous pairs, one member of each pair having been acquired from the gamete of one of the two parents of the individual whose cells are being examined. The DNA can only function in replication and transcription because it is associated with proteins that control and catalyze the process [65].

The DNA of the biggest human chromosome is about $274 \cdot 10^6$ base pairs long and as each base pair is around 0.3 nm this gives a total length of the DNA to around 8 cm. When the chromosomes are condensed into the X shape they are about 2-20 μm long [66]. Chromosomes will have different shapes and sizes depending on what period of the cell cycle they are in. For most of the life of the cell, chromosomes are very difficult to observe under a microscope. This is called interphase (the period of the cell cycle where the cell is not dividing) and individual chromosomes cannot be distinguished - they appear in the nucleus as a homogeneous tangled mix of DNA and protein [65].

During mitosis (cell division), the chromosomes start to roll up (become more condensed). They stop to have their normal function (transcription stops) and form the well known X shaped structure which makes the individual chromosomes visible. Figure 1.13 A and B show a Transmission Electron Microscopy (TEM) image and an Atomic Force Microscopy (AFM) image of a metaphase human chromosome. The shorter arms are called p arms and the longer arms are called q arms. This is the only natural context in which individual chromosomes are visible with an optical microscope. Therefore, in order to study the chromosomes, they have to be forced to enter into the metaphase [65]. In this project human chromosomes in the metaphase were used for the investigation.

1.6.2 Peptides

Peptide molecules are interesting as they exists in most living organisms [67]. If they are formed by a small number of amino acids (2-20) they are call oligopeptides. However, peptide links can join together from 20 to 2000 amino acids residues in length to form polymeric chains of L-α-amino acids known as polypeptides [68]. The chemical diversity and flexibility plus their stability and biocompatibility make peptides key building blocks for applications in bionanotechnology. The dipeptide from the diphenylalalnine motif of the Alzheimer's β-amyloid

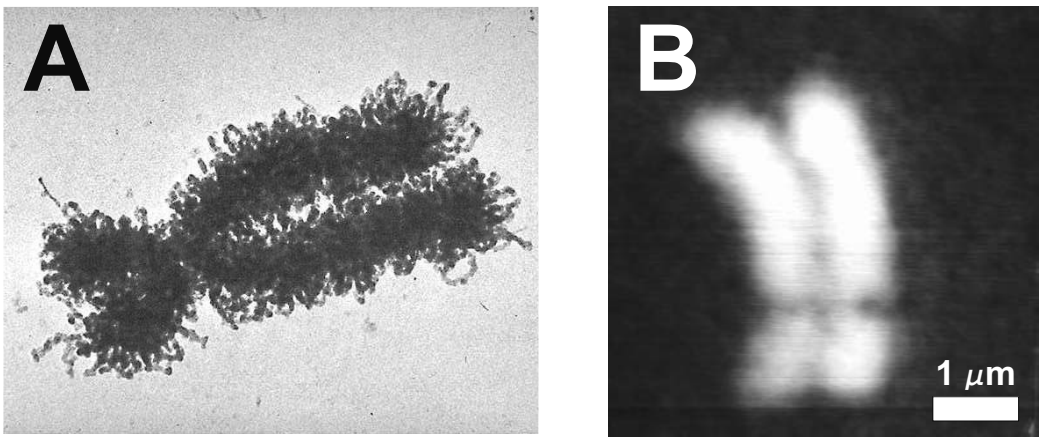

Figure 1.13: A) TEM image of a human metaphase chromosome [12] B) AFM image of a human metaphase chromosome obtained by the author.

peptide is the smallest and simplest peptide used for the fabrication of rigid nanotubes [69].

Biological tubular nano structures have several interesting applications as they are normally made up of self-assembled building blocks [21]. These structures are highly ordered giving rise to some unique properties [70]. In this project diphenylalanine peptides structures were investigated as they have the interesting ability to self-assemble into different superstructures such as tubes or spheres which have diameters in the nanometer scale [13]. Figure 1.14 A illustrates the β-amyloid molecule, while figure 1.14 B to D illustrate the self-assembly mechanism of the peptide tube as presented in [13].

Research describing the reactions on an atomic level is to my knowledge not available. But J. D. Hartgerink *et al.* [71] state that it could include dipole interaction, $\pi - \pi$ stacking, hydrogen bonds, electrostatic, and hydrophobic forces or a combination of them. Studies, [13], have indicated the assembly process as illustrated in figure 1.14. The protein molecules first stack in a single row (figure 1.14 B) followed by the formation of sheets (figure 1.14 C). Probably due to hydrophobic forces these sheets roll up into a tube in water as S. Zhang *et al.* [21] suggests. Tubular structures will contain several tubes around each other in the same way as with the graphite sheets structure in carbon nanotubes [72]. As the β-amyloid molecule is an organic compound it has been shown that it is easy to chemically modify its surface with bio-molecules [23]. Also the organic structure makes it rather easy to dissolve the tubes again. This has led to the tubes having been used as molds for the casting of metallic wires and the fabrication of coaxial cables [13]. The tubes have also been used for enhancing the signal of electro chemical electrodes [20].

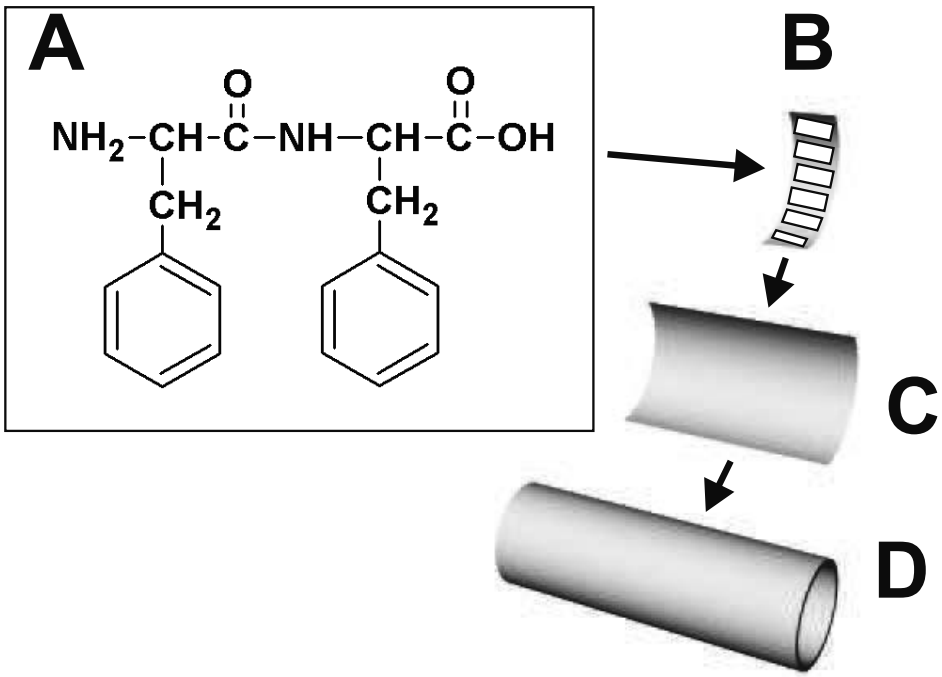

Figure 1.14: Schematic drawing of the expected self-assembly process for β-amyloid peptide tubes based on work done by [13].

1.6.3 Immunoglobulin G

The last sample type to be investigated was Immunoglobulin G (IgG). IgG is a protein which exists in blood and form part of the immune system [67].

Protein-protein interactions constitute the key mechanism for maintaining the function of cells. Understanding the physical principles governing these interactions and the ability to predict the presence of both interacting partners and the three-dimensional structures of the complexes they form are therefore very important tasks. Electrostatic interactions, being long-range interactions, are of particular interest for protein-protein association. Today protein-protein interactions can be detected in several ways. One of the most common methods to detect the protein-protein binding is to use fluorescent labeled proteins. In this way the binding can be detected by the fluorescence of the single proteins. However, in order to understand the binding mechanisms better the potential of the proteins before and after binding could be investigated. Thereby interaction between different types of proteins could be described by the overall surface potential of the structure. This could e.g. be utilized as a label free detection method for different protein-protein interactions.

The interaction between IgG from rabbits, and an antibody against it was investigated using KPM. IgG is a protein which serves as the antigen for the production of antibodies [67]. Antibodies are also proteins called immunoglobulins (Ig) and they are part of the immune system. These antibodies are the ”soldiers”, which identify the enemy, also called the antigen (foreign bodies e.g. viruses), and then neutralize the antigen by enveloping them. IgG was chosen for this experiment, because its antibody (anti-IgG) has a very specific binding to a single antigen (IgG), [67, 73]. It will therefore be a good test system for investigating the possibility of measuring the surface charge of the antigen, antibody, and the bonded antigen and antibody in order to see if they can be distinguished using this property.

The IgG used in this experiment was ordered from Sigma-Aldrich Denmark A/S. The IgG (Sigma-Aldrich: I5006) came from a rabbit serum and the anti-rabbit IgG (Sigma-Aldrich: R5506) was developed in goat IgG fraction of antiserum. As such the antigen used is actually also an antibody [67]. The antibody (IgG) molecule can be described as a Y-shaped molecule (based on X-ray crystallography), which consists of three equal sized branches that are connected by a flexible tether [67]. The Y shaped structure is formed by four protein chains, two light and two heavy. These are bound together by disulfide bonds [67]. A sketch of the antibody molecule is shown in figure 1.15 A based on [67]. The antigen also has a Y-shape form (also based on X-ray crystallography) and its structure is similar to that of the antibody (two heavy and two light protein chains); it is just made up of different protein chains.

The two arms of the Y-shape (made up of the light and heavy chain) are called the V region. It is this region that the molecule uses to bind with. The base of the Y-shape is called the C region. It is this C region which distinguishes the five classes of immunoglobulin (IgM, IgD, IgG, IgA, and IgE) from each other [67]. The immunoglobulin molecule is a very flexible structure. The two arms can move independently and the V region can bend and rotate relative to the C region, because of the hinge region (the junction between the V and C region) [67]. The size of IgG has been measured to 14,5 nm $\times$ 8,5 nm $\times$ 4,0 nm by X-ray diffraction [67]. Due to the high degree of flexibility of the IgG molecule different heights have been measured. The binding of anti-IgG to IgG is sketched in figure 1.15 B. It is the anti-IgG that binds to IgG so the active arms (V regions) of the anti-IgG bind to the C region of the IgG (as the C region is specific for this Ig antibody). The IgG (antigen) height has been measured at 4 nm to 9 nm and the height of the anti-IgG (antibody) from 4,2 nm to 12 nm [74, 75, 76]. It is hard to predict the exact height of the molecule when it is attached on a surface, as it depends on what orientation it has on the substrate, where it is micro-contact printed. The anti-IgG and the IgG are as earlier explained both antibodies, and they therefore both have the same Y-shape and thereby size. The only difference

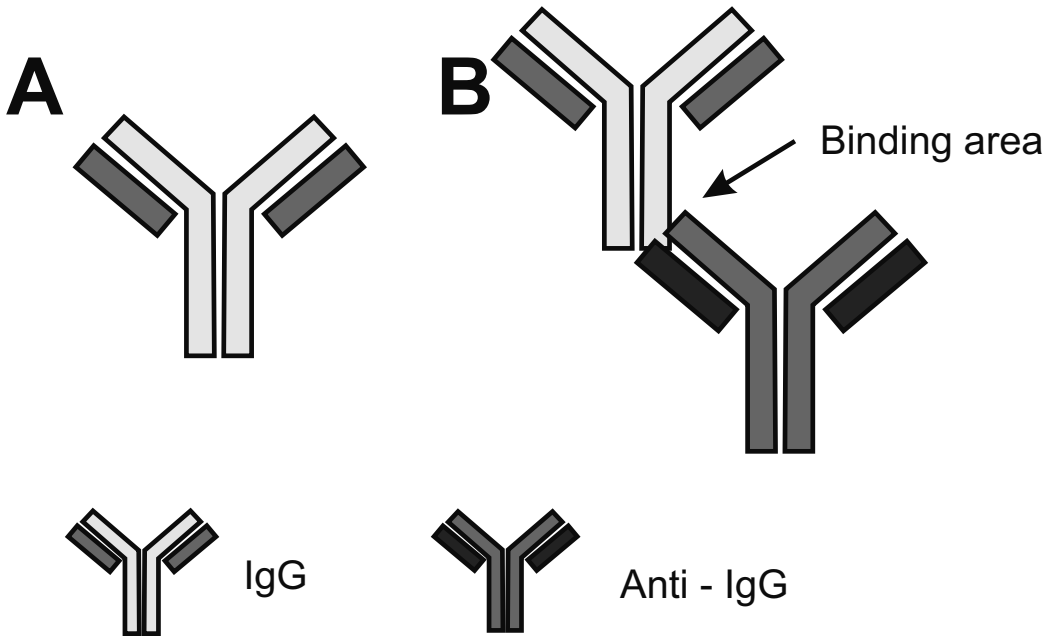

Figure 1.15: A) Schematic drawing of the structure of the IgG and anti-IgG proteins. The structure consists of two heavy protein chains (light grey) and two light chains (dark grey) connected by disulfide bonds B) The expected interaction between the IgG (light grey) and anti-IgG protein (dark grey).

between the two is the amino acids at the end of their arms [67]. The anti-IgG will have amino acids which can only bond to the IgG, whereas the ends of the IgG arms will be inactive in this system. The arms of the anti-IgG can and will bond anywhere on the IgG molecule. For the electrostatic measurements it is the change in the surface charge at the arms of the Y-shape protein, where the antigen binds to the antibody, which is going to be investigated.

1.7 Outline

In chapter 1 the background and the aim of the project are given. Furthermore, a description of the different biological samples used are described. Chapter 2 describes the different scanning probe microscopy methods used in this project. It also contains descriptions of the different effects encountered in SPM in order to analyze the data better. Chapter 3 contains a description of investigations carried out with these methods on human metaphase chromosomes and different dipeptide superstructures. Chapter 4 describes the fabrication and the micro-fluidic systems used in order to obtain an estimate of the electromobility and conductivity of human chromosomes. This chapter also describes the compilation of the estimates of the dielectric constant obtained in chapter 3 with the estimated values

from chapter 4 and a discussion of the results. Chapter 5 contains a conclusion of the project as well as suggestions for continuations for work in the area.

Chapter 2

Scanning Probe Microscopy

Scanning probe microscopy (SPM) is a term covering a range of techniques which probe (or feel) force interactions on the nanoscale. A sharp tip is normally used as the probe [32]. There are numerous techniques within SPM depending on the detected interaction. There are mainly two types of readout: either an electrical signal (e.g. in scanning tunneling microscopy) where the tunneling of electrons between the sample and tip is used for the readout of the surface electron distribution [32], or the deflection of a cantilever containing the tip is monitored. The most used interaction for readout is the Van der Waals force and the specific method monitoring this force is either called Scanning Force Microscopy (SFM) or Atomic Force Microscopy (AFM) [32, 33]. Other typically monitored interactions include electrostatic forces like Kelvin Probe Force Microscopy (KPM) or Electrostatic Force Microscopy (EFM) [32]. In recent years advances in the interpretation of the signals have led to the use of SPM for mapping out electrical properties of different nano sized particles [41, 38, 39]. This makes SPM an interesting collection of methods for studying the electrical properties of small samples. It seems natural to continue this line of studies on biological samples.

The chapter will describe the theory behind the SPM methods used in this project: AFM, EFM (or EFM-phase), and KPM.

2.1 Concept of Atomic force Microscopy

The basic principle behind AFM is that a sharp tip on a cantilever close enough to a surface will interact with it through the surface forces. These forces are normally in the range of 1 nN [25] but can be as low as tens of pN [77]. The tip is scanned across the surface and the deflection of the cantilever caused by the surface topography is typically measured with a laser beam and a position sensitive photo detector (see figure 2.2).

To scan the tip across the surface, piezoelectric elements (forming a tube called

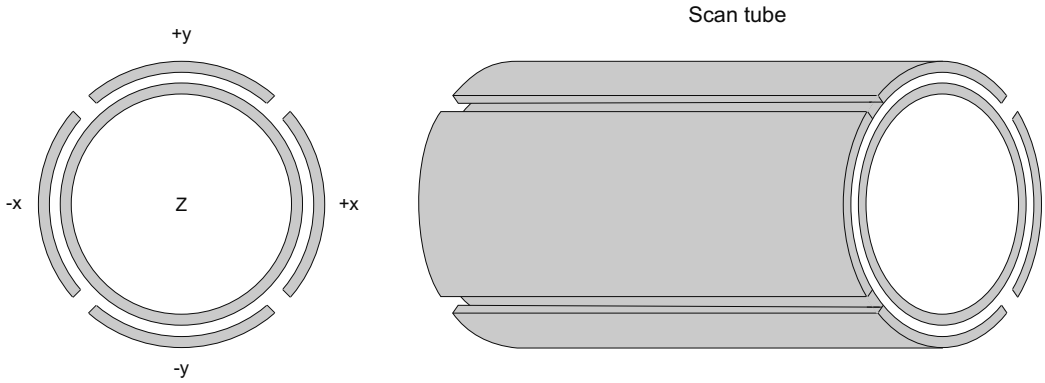

Figure 2.1: Schematic drawing of a scan-tube element used in SPM systems.

a scan-tube) are used to either move the cantilever or, as in the system used in this project, the sample, or even both (sample in x-y and tip in z). When a voltage is applied to the piezoelectric crystals they mechanically deform [78]. In the system used in this project the scan-tube consists of a number of piezo elements (typically five), as shown in figure 2.1, called x,-x,y,-y, and z. These are used to deflect the tube in the corresponding directions [25]. Figure 2.2 outlines the working principle of a typical SPM system. The scan-tube is used to scan the sample in a raster pattern across the desired area of the surface. The readout from the position sensitive photo-detector is subtracted by the set point (the deflection of the cantilever when it interacts with the surface see section 2.2) and sent to a feedback-controller, which changes the signal to the scan tube accordingly, so that the distance between the tip and the surface is kept constant. The changes in height of the scan-tube are then read from the feedback-controller, which then gives the surface topography. The feedback-controller used is either a PID (Proportional–Integral–Derivative) or PI (Proportional–Integral)-controller, depending on the SPM system [32]. The PI/PID controller is used to keep the deflection of the cantilever at the setpoint by changing the piezo element.

Explaining in detail how the PI/PID controller works is beyond the purposes of this thesis and a detailed description can be found in [79]. However, a simple description will be given here for completeness. As the cantilever scans the topography it will at some point encounter a step , e.g. upwards. The cantilever will feel an increased force and to keep the force stable the controller will react by reducing the deflection of the cantilever to reduce the force again. If the PI/PID controller is not properly calibrated a so called ”overshoot” will occur, as drawn in figure 2.3. Before each scan the parameters P, I, and D are therefore adjusted in order to reduce this overshoot. The PID/PI controllers response to topography changes is also dependent on the scanning time: the slower the scanning the more time the system has to adjust to the changes [32] and the smaller the overshoot.

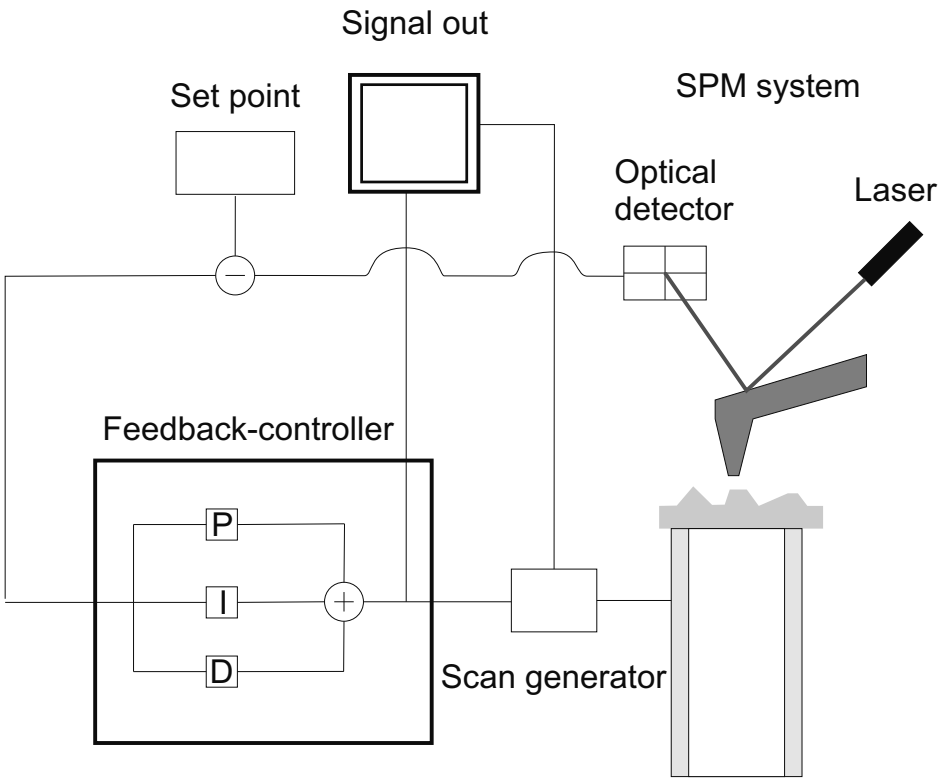

Figure 2.2: Principle of AFM: A scan-tube moves the sample in a raster pattern and a laser beam is reflected on the cantilever. The deflection of the cantilever is detected and the set point is subtracted. The result is fed to a feedback loop which adjusts the piezo element in order to keep the cantilever-sample distance constant. The change of the piezo element is recorded as the topography [14].

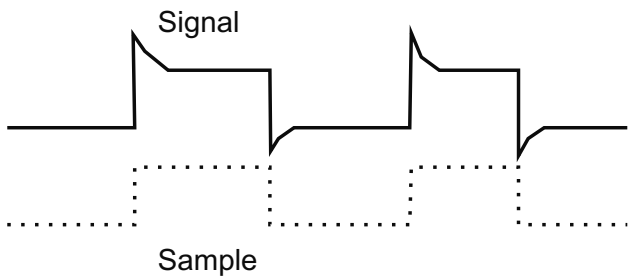

Figure 2.3: Schematic drawing of a topography signal and sample with an effect of the Feedback loop shown.

There are different forces acting between the tip and the surface. The first force acting on the tip as it approaches the surface is the Van der Waals force. Ideally, the tip of the AFM cantilever ends in a single atom. As the tip approaches the surface, this atom at the end of the tip generates an image charge in the surface.

For simplicity it is assumed that the tip atom only has one valence electron and the total charge of the atom is the same as the electron with opposite sign. A schematic drawing of the induced image charge in the surface is then as shown in figure 2.4.

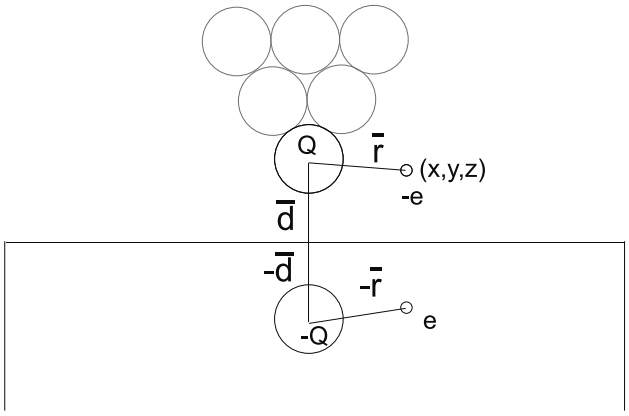

Figure 2.4: Schematic drawing of the end atom of the AFM tip interacting with a surface where d is the distance between the tip and surface.

This image charge gives rise to a potential energy between tip and surface given by [80]:

$$V_{VdW} = -\frac{1}{4\pi\epsilon_0}\frac{e^2}{d} - \frac{1}{4\pi\epsilon_0}\frac{e^2}{2(d+z)} + 2\frac{1}{4\pi\epsilon_0}\frac{e^2}{|2\bar{d}+\bar{r}|}. \tag{2.1}$$

Where e is the elementary charge, ϵ_0 is the vacuum permittivity, $\bar{d} = (0, 0, d)$ is the distance between the surface and the tip, and $\bar{r} = (x, y, z)$ is the distance between the center of the atom and its electron. Expanding equation 2.1 in a Taylor series by terms of $\frac{\bar{r}}{d}$ gives:

$$V_{VdW} \propto -\frac{e^2}{d^3}\Big(\frac{x^2}{2} + \frac{y^2}{2} + z^2\Big). \tag{2.2}$$

As the electron moves more or less at the same distance from the atom, the potential can be written as:

$$V_{VdW} \propto -\frac{C}{d^3}, \tag{2.3}$$

where C is the Van der Waals constant. As the tip further approaches the surface, the surface electrons of the tip and the surface will begin to repel each other. A way to describe the repulsing energy is an exponential function, since the density of the surface electrons decays exponentially with distance from the surface [81]. Thus, the repulsing part will be:

$$V_r \propto e^{-\frac{d}{\alpha}}, \tag{2.4}$$

where α is a constant determined by the electrons interaction. Combining equations 2.3 and 2.4 gives

$$V_{total} \propto -\frac{C}{d^3} + e^{-\frac{d}{\alpha}}. \tag{2.5}$$

This function is plotted in figure 2.5.

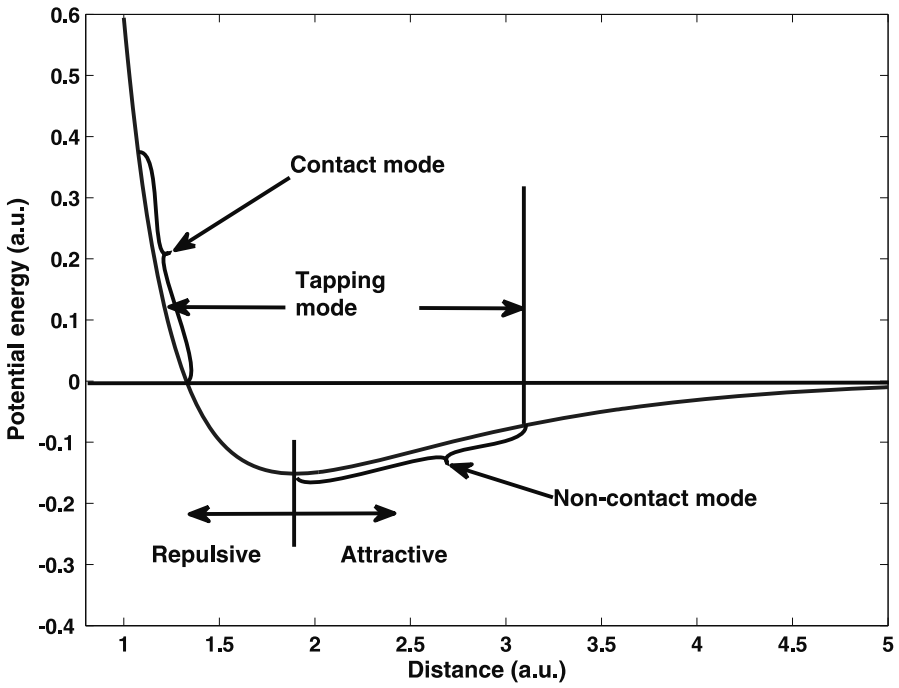

Figure 2.5: Energy potential vs. distance curve for tip surface interaction.

The above is an idealized description of the tip sample interaction. Normally the single atom at the end of the tip is not the only one participating in the interaction (although under the right conditions AFM can be used to obtain atomic resolution [82]). The tip geometry gives rise to two different effects on the topography. First in the vicinity of the surface the tip can be described as a circle (figure 2.6 A). This causes the topography image of samples with sizes less than the tip radius to widen to $w = \sqrt{r \cdot 8 \cdot h}$, where w is measured width, r the radius of curvature of the tip, and h the height of the sample. Further, as the tip normally is attached to a cone at an angle, objects larger than the tip radius of curvature will appear with inclined slopes (figure 2.6 B). As the dimensions of the cantilevers are not well defined (see e.g. [83]) only the sample height can be precisely measured from topography data. Further, as the Van der Waals force is not the only force on the tip, other effects may contribute to the topography, such as capillary forces.

This makes it rather impossible to get the size of the sample in the x,y plane, even if the dimensions of the cantilever were mapped out precisely.

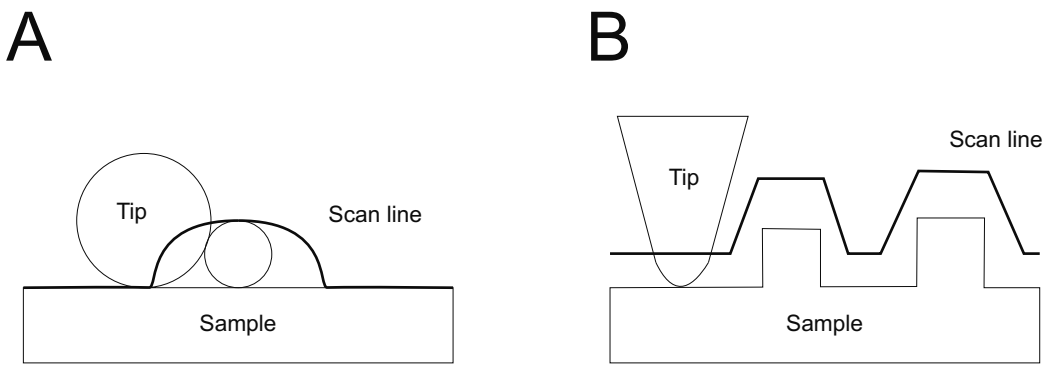

Figure 2.6: Schematic drawings of different tip effects on the recorded topography A) widening of sample size caused by the tip's radius of curvature, B) inclined slopes caused by the interaction between the cone and sample when the scanned objects are larger than the tip's radius of curvature.

Other forces that act on the cantilever are capillary and electrostatic forces. The capillary forces arise from water bound on the surface either from the ambient conditions or from when the sample is deposited on the surface. There are several ways to minimize this force either by operating the tip in vacuum or in liquid or by using a vibrating tip [32]. The capillary force can be a problem if high resolution images are required, as in the case of imaging of single molecules. The electrostatic forces arise from the build up of surface charge on the sample or tip and can create a loss of resolution as one will image the repulsion or attraction of these charges. This force can be minimize by grounding tip and sample [32].

2.2 Operations Modes

Topography data can be obtained in two different ways: when using a vibrating cantilever the mode of operation is called dynamic mode or amplitude modulation, as the scans are done at a fixed vibration amplitude. This mode can further be divided into non-contact and tapping mode. When the cantilever is not vibrating and in contact with the sample the mode of operation is called contact mode.

2.2.1 Contact Mode

In contact mode the tip is so close to the surface that the interaction is described by the repulsive part of the force curve in figure 2.5. This method has two modes of operation; one of constant deflection/force on the cantilever and the other of measured deflection of the cantilever. In constant force mode the force between the tip and the surface is kept constant by a feedback-loop. In the deflection

mode the topography of the surface can be read directly by the photo-detector. An advantage of the constant force mode is that the force the tip exercises on the surface can be controlled (determined by a constant deflection of the cantilever, called set point in section 2.1). The cantilevers used for this mode are long ($> 400\mu$m) and soft (spring contact around 1 Nm^{-1}) compared to the cantilever types used in the other modes. The deflection mode is normally used for making atomic resolution images in ultra high vacuum. It can also scan faster than the constant force mode because the scan-tube movement is not controlled by a feedback-loop [84, 14]. The contact mode does however have some challenges. As the tip is "dragged" across the surface, structures deposited on it and not securely fixed to the surface will have a tendency to be "pushed" by the tip. This dragging can also easily damage soft samples if the appropriate force is not applied. Further if not operated in ultra high vacuum or liquid the capillary forces will play a big role in the tip-sample interaction [32].

2.2.2 Non-Contact Mode

In non-Contact mode, the interaction between the end of the tip and the sample is smaller than in contact mode (10^{-11} N as opposed to 10^{-8} N for contact mode [32]). Here the system measures the change in vibrational amplitude of the cantilever, which is being vibrated at a fixed frequency just above its resonance frequency (see figure 2.7) [14]. In non-contact mode, the interaction force used is the attractive part of the force curve in figure 2.5. When the tip interacts with the surface, the frequency changes and the measured amplitude decreases or increases depending on the interaction (see figure 2.7). The set point, which is here defined as the change in vibration amplitude of the cantilever when it interacts with the surface, determines the average force of the scanning or the average distance of the tip from the surface. As the tip approaches the surface for scanning the resonance frequency decreases and as a result the vibrational amplitude decreases to the set point. The formula for the dependence of the resonance frequency (ω_0) on the force (F) is given by:

$$\omega_0 = \sqrt{\frac{k - \frac{\partial F}{\partial z}}{m^*}}, \tag{2.6}$$

where k is the spring constant of the cantilever, m^* is the effective mass of the cantilever, and z is the distance between the tip and the surface. When the AFM cantilever encounters a bump on the scanned surface its resonance frequency changes to a lower value. This is because, as figure 2.5 shows, the first derivative of the force increases as the distance between the tip and the surface decreases. So the piezo element connected to the feedback-loop responds and moves the surface (or tip) away. The opposite happens when there is a hole in the surface [32]. The cantilevers used for this mode normally have a spring contact around 10-60 Nm^{-1}.

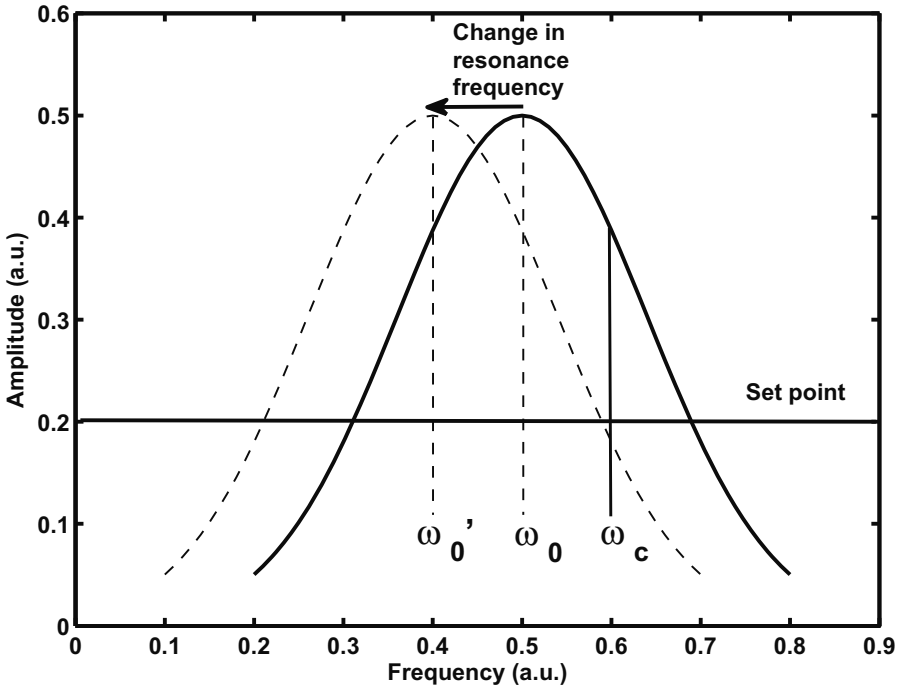

Figure 2.7: Schematic drawing of the resonant frequency shift for the non-contact mode. ω_c is the frequency which drives the cantilever and the set point determines the amplitude where the tip is interacting with the sample. ω_0 is the free resonance frequency and ω_0' is resonance frequency when the tip encounters a bump.

2.2.3 Tapping Mode

The intermediate mode or the tapping mode works almost like the non-contact mode. Here the cantilever is still vibrated, but the tip moves down and ”touches” the surface at maximum amplitude of the vibration i.e. the part of the potential energy curve just as the force becomes repulsive (see figure 2.5). As the system can only measure the changes in the amplitude of the resonance frequency and one wants the tip to ”touch” the surface at maximum amplitude (operating in the repulsive range), one has to set the frequency at which the cantilever is vibrated below the resonance frequency. This means that the resonance peak first moves to the left (increasing the amplitude, see figure 2.5) and then to the right (decreasing the amplitude to the setpoint, see figure 2.5) i.e. the repulsing part of the curve in figure 2.5. So when the tip is interacting with the surface and meets a bump on it, the resonance frequency is shifted to a higher value and of course the other way around with a hole. One advantage of tapping mode over non-contact is that if condensed water is present on the sample surface, the tip will be repelled by the water in non-contact mode as the tip is not in contact with the sample. In tapping

mode, on the other hand, the tip will penetrate the water if the underlying substrate is hard, as shown in figure 2.8. Since the tip is not dragged across the surface in tapping mode as in contact mode, the shape of the tip (i.e. the sharpness) is not so rapidly degraded and if the surface is hard the tip is not damaged by the scanning. The cantilevers used for tapping typically have a spring constant close to $50 - 200$ Nm^{-1}. Further as the tip is not dragged across the surface it does not "push" samples which are not fixed on the surface [32].

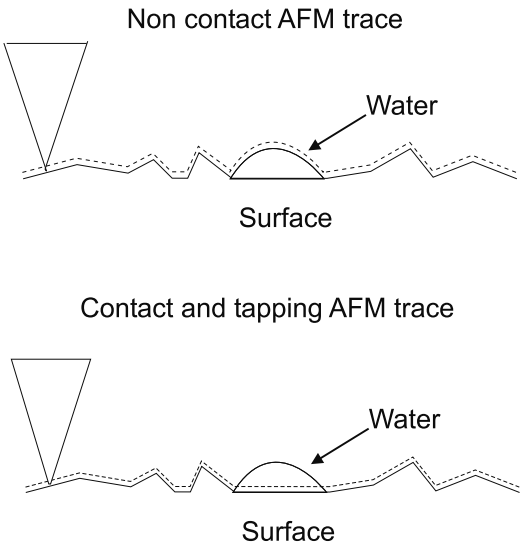

Figure 2.8: Schematic drawing of the effect of condensed water on the AFM image of different scanning modes.

2.3 Concept of Electrostatic Force Microscopy

Electrostatic force microscopy (EFM) or EFM-phase is a scanning probe microscopy method, which can be used to measure different electrical properties of materials on the micro- and nano-scale. The method is a dual scan/pass method which has several applications. The method was first used to map out the conductivity of particles with respect to the supporting substrate [41, 38]. So in the early reports this method is called scanning conductance microscopy [38, 85, 41]. The potential of this method is not yet fully investigated as the method has only been around for a few years. The method can with some modifications also be used to measure surface potential or charge [39]. It utilizes the principle of atomic force microscopy in the dynamic mode.

2.3.1 Principle

Simply put the EFM method can be explained by considering a capacitor, where a conducting substrate with the samples on top acts as one of the plates while the other plate is represented by the AFM cantilever tip, which in this case is covered by a conducting material. The principle of the method is that first a line-scan is made in a dynamic mode (tapping or non-contact). Next, the AFM cantilever is raised several tens of nanometers above the surface. A new line scan is made at this distance (called lift-height), where the cantilever follows the topography of the previous scan. During the second scan the phase of the vibration of the dynamic mode (ϕ) is measured and a potential is applied between the tip and the conducting substrate. Normally the substrate for measuring consists of a heavily doped silicon substrate with a thermally grown layer of oxide (SiO_2) on top. The sample under investigation is placed on the substrate layer. The principle of the setup is shown in figure 2.9.

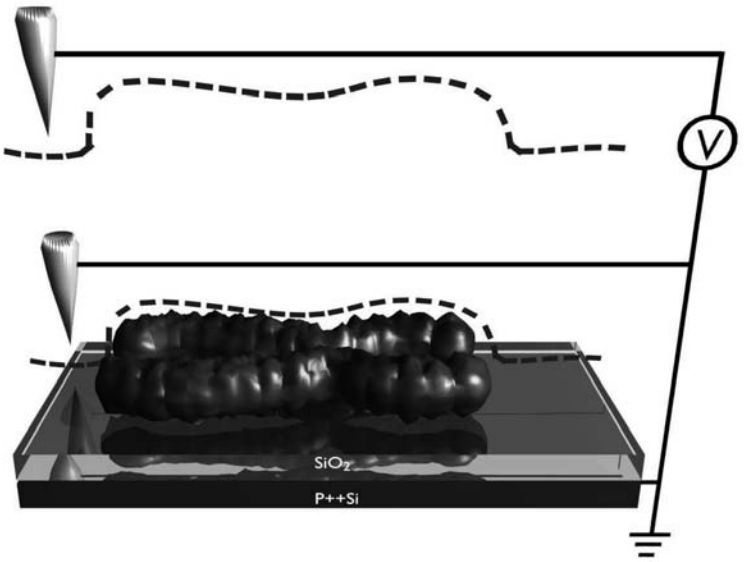

Figure 2.9: Schematic drawing of the principle of EFM on a sample (blue) on a surface.

To investigate the behavior of the system it is assumed that the vibrating AFM tip can be described as a plate that vibrates with respect to a substrate (see figure 2.10).

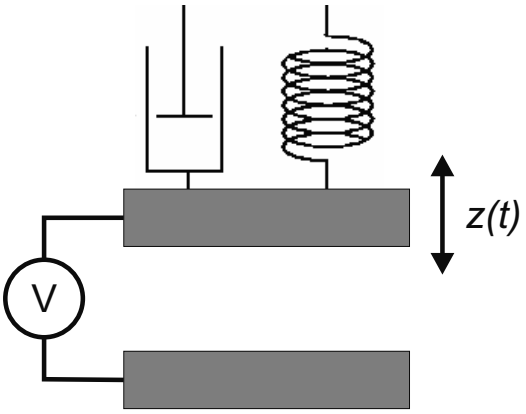

Figure 2.10: Schematic drawing of the tip surface EFM interactions, used for modeling the signal response.

Then the force acting on it is given by Newton's second law as

$$m \cdot \frac{\partial^2 x(t)}{\partial t^2} = F_d\big(t\big) + F_{el}\big(x(t)\big) - k \cdot x(t) - m \cdot \gamma \frac{\partial x(t)}{\partial t}, \tag{2.7}$$

where m is the mass of the cantilever, $x(t)$ the distance between the two plates, t the time, $F_d(t)$ is the force driving the vibration, $F_{el}\big(z(t)\big)$ the electrical force acting on the top plate, k is the spring constant, and γ is the damping factor. If it is assumed that the driving force can be described as $F_d\big(t\big) = F_0 \cdot \exp(i \cdot \omega \cdot t)$ where F_0 is the amplitude of the driving force and ω the angular frequency of it, the position as $x(t) = x_0 \cdot \exp(i \cdot (\omega \cdot t + \phi))$ where ϕ is the phase, x_0 the average distance between the plates, and that the electrical force can be approximated by Taylor expansion series as $F_{el}\big(x(t)\big) = F_{el}\big(x_0\big) + \frac{dF_{el}\big(x_0\big)}{dx}(x(t) - x_0)$ then equation 2.7 becomes

$$-\omega^2 \cdot m \cdot x_0 \cdot \exp(i \cdot (\omega \cdot t + \phi)) = F_0 \cdot \exp(i \cdot \omega \cdot t) +$$

$$F_{el}\big(x_0\big) + \frac{dF_{el}\big(x_0\big)}{dx}(x_0 \cdot \exp(i \cdot (\omega \cdot t + \phi)) - x_0) -$$

$$k \cdot x_0 \cdot \exp(i \cdot (\omega \cdot t + \phi)) - i \cdot m \cdot \omega \cdot \gamma \cdot x_0 \cdot \exp(i \cdot (\omega \cdot t + \phi)). \tag{2.8}$$

The parts of equation 2.8 which contain the exponential terms must be equal as they are time dependent so

$$F_0 \cdot \exp(i \cdot \omega \cdot t) = -\omega^2 \cdot m \cdot x_0 \cdot \exp(i \cdot (\omega \cdot t + \phi)) + k \cdot x_0 \cdot \exp(i \cdot (\omega \cdot t + \phi)) +$$

$$i \cdot m \cdot \omega \cdot \gamma \cdot x_0 \cdot \exp(i \cdot (\omega \cdot t + \phi)) - \frac{dF_{el}\big(x_0\big)}{dx} \cdot x_0 \cdot \exp(i \cdot (\omega \cdot t + \phi)). \tag{2.9}$$

This can be rewritten as

$$\frac{F_0}{m \cdot x_0} = \Big(-\omega^2 + \omega_0^2 + i \cdot \omega \cdot \gamma - \frac{1}{m} \cdot \frac{dF_{el}\big(x_0\big)}{dz} \Big) \cdot \exp(i \cdot \phi), \tag{2.10}$$

where $\omega_0^2 = \frac{k}{m}$. If we define $\frac{F_0}{m \cdot x_0} = D$ and write $\exp(i \cdot \phi)$ as $\cos(\phi) + i \cdot \sin(\phi)$ then the equation becomes

$$D \cdot (\cos(-\phi) + i \cdot \sin(-\phi)) = -\omega^2 + \omega_0^2 + i \cdot \omega \cdot \gamma - \frac{1}{m} \cdot \frac{dF_{el}\big(x_0\big)}{dx}. \tag{2.11}$$

The real and imaginary parts on both sides of the equation must be equal, which gives

$$D \cdot \cos(-\phi) = -\omega^2 + \omega_0^2 - \frac{1}{m} \cdot \frac{dF_{el}\big(x_0\big)}{dx} \tag{2.12}$$

and

$$D \cdot i \cdot \sin(-\phi) = i \cdot \omega \cdot \gamma. \tag{2.13}$$

Combining the two equations one gets

$$\tan \phi = \frac{\omega \cdot \gamma}{\omega_0^2 - \omega^2 - \frac{1}{m} \cdot \frac{dF_{el}\big(x_0\big)}{dz}}. \tag{2.14}$$

Assuming $\omega = \omega_0$, which is a good assumption as the cantilever is vibrated close to its resonance frequency, and defining the quality factor as $Q = \frac{\omega_0}{\gamma}$ equation 2.14 becomes

$$\tan \phi = -\frac{k}{Q \cdot \frac{dF_{el}\big(x_0\big)}{dx}}, \tag{2.15}$$

or

$$\phi = -\tan^{-1}\Big(\frac{k}{Q \cdot \frac{dF_{el}\big(x_0\big)}{dx}}\Big), \tag{2.16}$$

where Q is the quality factor of the cantilever, k the spring constant, and x the cantilever substrate distance. For small phase shifts around the resonance (x_0, ω_0) equation 2.16 can be rewritten by using Taylor expansion as

$$\phi \approx -\frac{Q \cdot \frac{\partial F_{el}}{\partial x}}{k}. \tag{2.17}$$

The derivative of the force can be written as [45]:

$$\frac{\partial F_{el}}{\partial x} = \frac{1}{2} \frac{\partial^2 C_{ts}}{\partial^2 x} \cdot V_s^2, \tag{2.18}$$

where V_s is the potential between the tip (with cantilever) and substrate and C_{ts} is the capacitance between the tip (with cantilever) and the surface [41]. Combining equations 2.16, 2.17, and 2.18 one gets the phase shift as

$$\phi = \tan^{-1}\left(\frac{k \cdot 2}{Q \cdot \frac{\partial^2 C_{ts}}{\partial^2 x} \cdot V_s^2}\right) \approx \frac{Q \cdot \frac{\partial^2 C_{ts}}{\partial^2 x} \cdot V_s^2}{k \cdot 2}. \tag{2.19}$$

Assuming that the contribution to the change in capacitance mainly comes from the tip (see section 2.3.2), then using equation 2.19 it can be seen that changes in the phase can only be caused by changes in the capacitance, i.e. by changes in material composition between the tip and the cantilever. These changes in the phase can be written as

$$\Delta\phi \approx \frac{Q}{k \cdot 2}\left(\frac{\partial^2 C_{ts}}{\partial^2 x} - \frac{\partial^2 C_{tp}}{\partial^2 x}\right) \cdot V_s^2, \tag{2.20}$$

where C_{ts} is the capacitance between the tip and the substrate without a sample inserted and C_{tp} is the capacitance between tip and substrate with the sample introduced.

If it is assumed that the tip is a flat circle (which is a good assumption according to T. S. Jespersen *et al.* [39]) and that the material between the sample and the cantilever is air, the second derivative of the capacitance can be written as

$$\frac{\partial^2 C_{ts}}{\partial^2 x} = \frac{2 \cdot \pi \cdot r_{tip}^2 \cdot \epsilon_0}{x^3},$$

where r_{tip} is the radius of the tip and ϵ_0 is the vacuum permittivity. If the space between the tip and substrate is partly filled with a medium with a different dielectric constant than air (e.g. an oxide layer on top of the conducting substrate) the second derivative of the capacitance becomes [45]

$$\frac{\partial^2 C_{ts}}{\partial^2 x} = \frac{2 \cdot \pi \cdot r_{tip}^2 \cdot \epsilon_0}{(z + d/\epsilon_{SiO_2})^3}, \tag{2.21}$$

where d is the thickness of the medium (in this case the oxide layer) and ϵ_{SiO_2} its dielectric constant. This can of course be expanded to include more that one medium. If we assume that a sample lies on top of the oxide layer the second derivative of the capacitance becomes

$$\frac{\partial^2 C_{tp}}{\partial^2 x} = \frac{2 \cdot \pi \cdot r_{tip}^2 \cdot \epsilon_0}{(z + d/\epsilon_{SiO_2} + h/\epsilon_p)^3}, \tag{2.22}$$

where h is the height of the sample in question and ϵ_p its dielectric constant.

So in order to estimate the dielectric constant of a sample a combination of equations 2.19 and 2.23 will give the shift in phase ($\Delta\phi$) between the bare substrate and the substrate with a sample on as

$$\Delta\phi \approx \frac{Q \cdot V_s^2 \cdot \pi \cdot r_{tip}^2 \cdot \epsilon_0}{k}\Big(\frac{1}{(z + d/\epsilon_{SiO_2})^3} - \frac{1}{(z + d/\epsilon_{SiO_2} + h/\epsilon_p)^3}\Big). \quad (2.23)$$

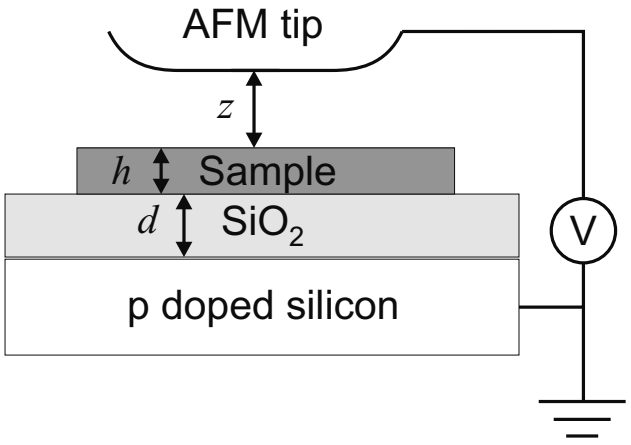

Figure 2.11: Schematic drawing of the EFM-phase method setup with the dimensions of equation 2.23.

2.3.2 Artifacts Effects

The above is of course an ideal description of reality; in a real system the tip is not the only source of electrostatic interaction. The cantilever and the cone of the tip also contribute as is illustrated in figure 2.12, which will result in more parts in equation 2.18.

Theoretical calculations done by J. Colchero *et al.* [42] indicate that the cantilever and cone contribute significantly to the force and hence the phase. Fortunately the calculations also show that these contributions are mostly constant for small changes in height (a few tens of nanometers). Figure 2.13 A shows the size of the force gradient of different parts of the cantilever (beam, cone, tip)-surface interaction for a typical cantilever used in the measurement (see appendix C for the full equations). The same equations can also be used to investigate what will happen if e.g. a sample is added on top of the oxide. Figure 2.13 B shows the same system as in A but now a layer with a thickness of 50 nm and a relative dielectric constant of 6 has been added. Figure 2.13 C shows the differences between figures 2.13 A and 2.13 B. As can be seen the model predicts that the tip makes the biggest contribution to the change of the gradient. The observed effect is that contributions from the cantilever and cone remain close to constant while

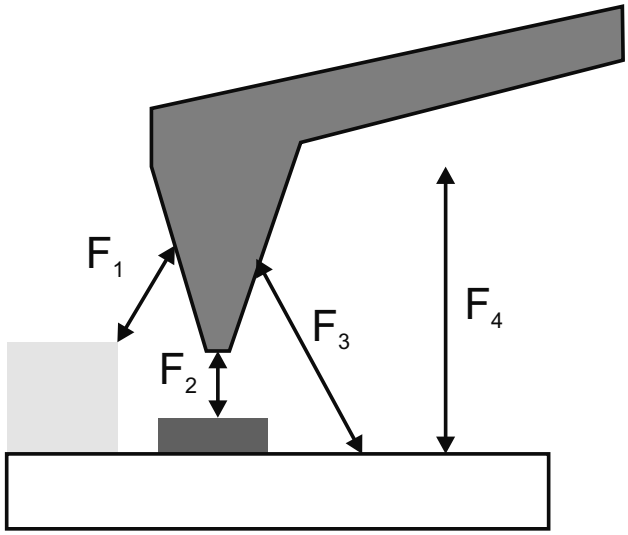

Figure 2.12: Schematic drawing of different electrostatic contributions between the cantilever and sample. In the modeling treatment they are divided into three different type: tip-sample (F_2) cone-sample (F_1 F_3), and cantilever beam-sample (F_4).

the effect on the contribution from the tip changes dramatically with tip-surface distance. This theoretically indicates that the method works. What the graphs also indicate is that within the first tens of nanometers the tip-surface interaction dominates the change in the force and so also the change in the phase. This pinpoints a range for the optimal lift-height in EFM.

Another source of error is the assumption that the tip is a flat disk, which is not completely right. In work done by J. Colchero *et al.* [42] the curvature of the tip is also taken into account in the calculations. Figure 2.14 shows the different force gradients for the flat tip model and tip apex curvature model as a function of distance. As figure 2.14 shows, the flat disk model is far from perfect, especially at distances below 30 nm (off by more than 10 %). At distances of more than 30 nm the error becomes smaller.

This makes it optimal to make the lift height scan at distances of 30-60 nm. This range is based on rather simple theory and is only to be used as a guidance for the working lift-height range.

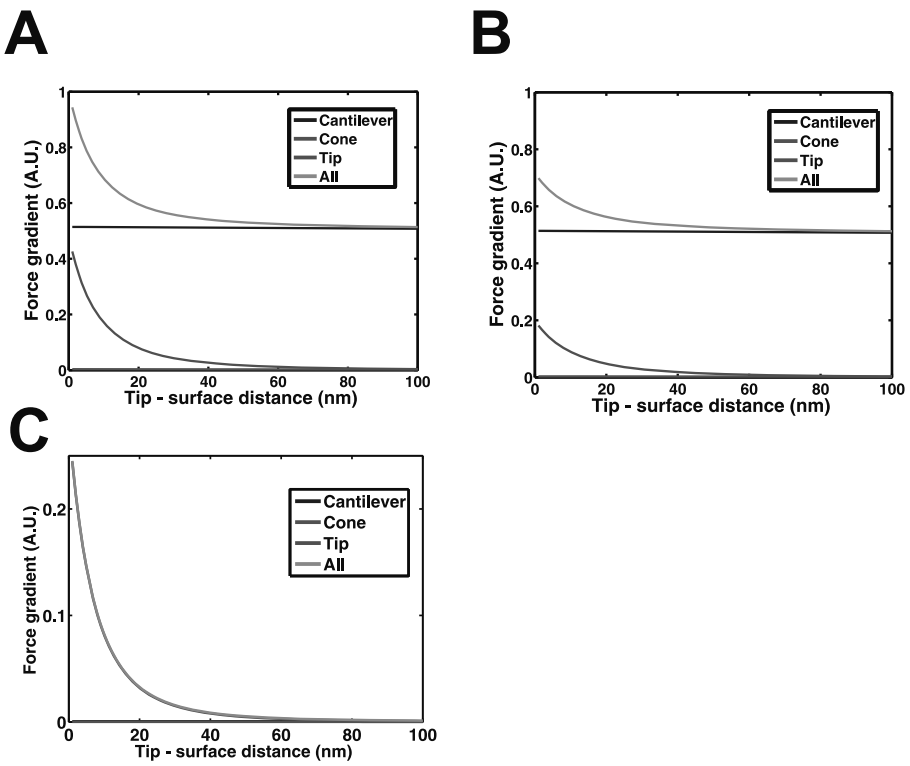

Figure 2.13: Graphs of the different force gradient contributions on the cantilever A) force gradient over bare substrates, B) force gradients over a sample with a dielectric constant of 6 and a thickness of 50 nm, C) the difference between the curves of A and B.

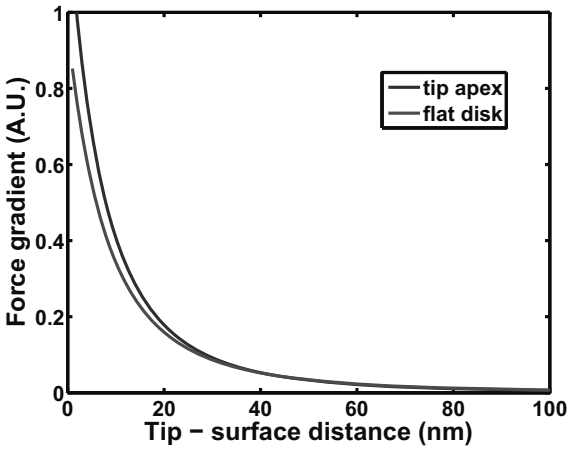

Figure 2.14: Plot of the different force gradients for the flat tip model and tip apex curvature model as a function of distance.

2.4 The Kelvin Probe Microscopy Method

Kelvin probe force microscopy or kelvin probe microscopy (KPM), as it is also known as, was developed in 1991 by M. Nonnenmacher *et al.* [37]. They demonstrated the methods capability to measure contact potential between metal lines on the nanoscale. It has since been used for characterization of transistors [86] and of different types of nano sized electronics based on e.g. carbon nanotubes [87] or organic thin films [88].

2.4.1 Principle

The principle of the KPM method is that a voltage is applied to the AFM cantilever [37]. The potential is applied during non-contact scanning in order to minimize tip sample interactions [88]. Both a DC and an AC voltage are applied to the tip so the total potential difference V_{tot} between the tip and surface is:

$$V_{tot} = -V_S + V_{DCt} + V_{ACt} \cdot \sin(\omega \cdot t), \tag{2.24}$$

where V_S is the local surface potential, V_{DCt} is the DC signal on the tip (plus cantilever), V_{ACt} is the amplitude of the AC signal, and ω is the frequency of the AC signal. If the signal between the cantilever and sample is neglected then $V_S = V_S(x, y)$ where (x, y) is the position of the tip. The frequency of the AC signal is normally much lower than the resonance frequency of the cantilever (a factor of 10) so the two signals (the one caused by the Van der Waals interaction and the one caused by the electrostatic interaction) can be separated from the optical readout of the laser by the photo-detector using a lock-in amplifier[88]. Via the electrostatic forces the setup measures the surface potential, which changes the amplitude of the potential signal. If one assumes that the tip is a plate capacitor then the force (F) between the tip and surface is given by [45, 39, 41]:

$$F = \frac{\frac{\partial C}{\partial z} \cdot V_{tot}^2}{2}, \tag{2.25}$$

where C is the capacitance and z is the distance between the tip and the surface. Combining equation 2.24 and 2.25 one gets;

$$F = \frac{\frac{\partial C}{\partial z}}{2} \cdot \Big(-V_S + V_{DCt} + V_{ACt} \cdot \sin(\omega \cdot t) \Big)^2 =$$

$$\frac{\frac{\partial C}{\partial z}}{2} \cdot \Big((V_{DCt} - V_S)^2 + V_{ACt}^2 \cdot \sin(\omega \cdot t)^2 + 2 \cdot (V_{DCt} - V_S) \cdot V_{ACt} \cdot \sin(\omega \cdot t) \Big), . \tag{2.26}$$

Using Pythagorean identities $\big[\cos^2(x) + \sin^2(x) = 1\big]$ and de Moivre's formula $\big[(\cos(x) + i \cdot \sin(x))^n = \cos(n \cdot x) + i \cdot \sin(n \cdot x)\big]$, $V_{ACt}^2 \cdot \sin(\omega \cdot t)^2$ becomes [88]

$$V_{ACt}^2 \cdot \sin(\omega \cdot t)^2 = V_{ACt}^2 \cdot \ \big(1 - \cos(\omega \cdot t)^2\big) =$$

$$\frac{1}{2} \cdot V_{ACt}^2 \cdot \left(2 - 2 \cdot \cos(\omega \cdot t)^2\right) =$$
$$\frac{1}{2} \cdot V_{ACt}^2 - \frac{1}{2} \cdot V_{ACt}^2 \cdot \cos(2 \cdot \omega \cdot t). \tag{2.27}$$

Equation 2.27 inserted in equation 2.26 gives:

$$F = \Big(\frac{\frac{\partial C}{\partial z}}{2} \cdot \left((V_{DCt} - V_S)^2 + \frac{1}{2} \cdot V_{ACt}^2\right) + \left(2 \cdot (V_{DCt} - V_S) \cdot V_{ACt}\right) \cdot \sin(\omega \cdot t) -$$
$$(\frac{1}{2} \cdot V_{ACt}^2) \cdot \cos(2 \cdot \omega \cdot t)\Big) = \tag{2.28}$$
$$k_1 + k_2 \cdot \sin(\omega \cdot t) + k_3 \cdot \cos(2 \cdot \omega \cdot t), \tag{2.29}$$

where $k_1 = \frac{\frac{\partial C}{\partial z}}{2} \cdot \left((V_{DCt} - V_S)^2 + \frac{1}{2} \cdot V_{ACt}^2\right)$, $k_2 = \frac{\frac{\partial C}{\partial z}}{2} \cdot (2 \cdot (V_{DCt} - V_S) \cdot V_{ACt})$, and $k_3 = -\frac{1}{2} \cdot \frac{\frac{\partial C}{\partial z}}{2} \cdot V_{ACt}^2$. The frequency ω is set by an external oscillator and can therefore be locked by the lock-in amplifier. The signal detected by the lock-in amplifier (the k_2 part) is minimized by varying V_{DCt}. When this signal approaches zero, this corresponds to $V_{DCt} = V_S$ (see equation 2.28) i.e. mapping V_{DCt} vs. the sample surface (x, y) gives $V_S(x, y)$. A schematic drawing of the principle is given in figure 2.15.

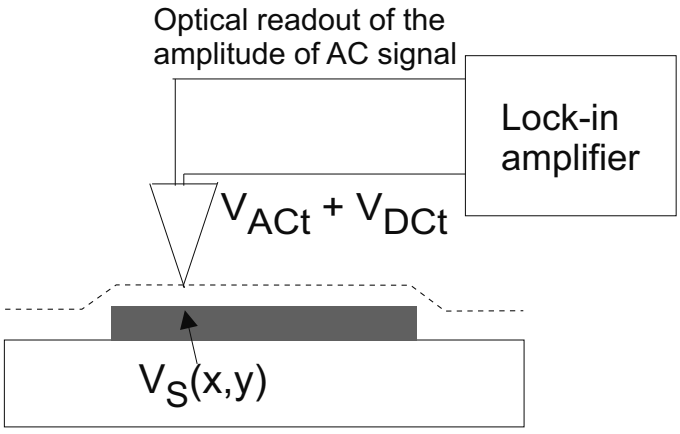

Figure 2.15: The principle of Kelvin probe microscopy (KPM). The lock-in amplifier generates a signal on the tip and the electrostatic tip-surface interaction is readout by the laser. The lock-in amplifier adjusts V_{DCt} to match the surface potential $V - S$.

2.4.2 Artifacts Effects

As with the EFM method described earlier (see chapter 2.3.2) the above is of course an idealized description. In the case of KPM the electrostatic signal from the cantilever and cone are even more profound with EFM [42]. Figure 2.16 shows the theoretically calculated force on the different parts (tip, cone, cantilever) of the AFM probe, based on work done by J. Colchero *et al.* [42].

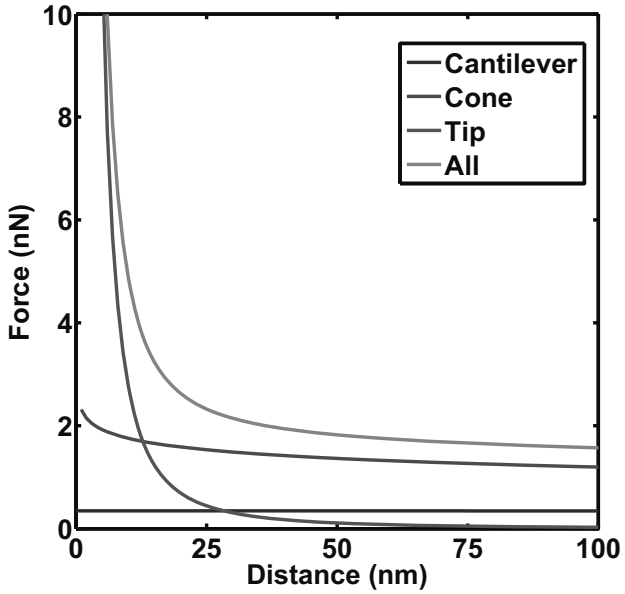

Figure 2.16: Graphs of the force contributions on the AFM probe (tip, cone, and cantilever) at a surface potential of 1V.

The force in equation 2.25 becomes [42, 2]:

$$F_{el} = \frac{1}{2} \sum \frac{\partial C}{\partial z} \cdot V^2,$$

The force from the different contributions is therefore

$$F_{el} = \frac{1}{2}\Big(\frac{\partial C_{ts}}{\partial z} \cdot (V_{DCt} + V_{ACt} \cdot \sin(\omega \cdot t) - V_S(x,y))^2 + \frac{\partial C_{res}}{\partial z} \cdot (V_{DCt} + V_{ACt} \cdot \sin(\omega \cdot t) - V_B)^2 \Big), \tag{2.30}$$

where $\frac{\partial C_{res}}{\partial z}$ is the derivative of the capacitance from cantilever- and cone-sample interaction and V_B is the average surface potential of the whole sample. Using the approach from section 2.4.1 the lock-in amplifier will lock to

$$F_{el}^{\omega} = V_{ACt} \cdot \sin(\omega \cdot t) \cdot \Big(\frac{\partial C_{ts}}{\partial z} \cdot (V_{DCt} - V_S(x,y)) + \frac{\partial C_{res}}{\partial z} \cdot (V_{DCt} - V_B) \Big). \tag{2.31}$$

The measured potential will then become

$$0 = \frac{\partial C_{ts}}{\partial z} \cdot (V_{DCt} - V_S(x,y)) + \frac{\partial C_{res}}{\partial z} \cdot (V_{DCt} - V_B) \Leftrightarrow$$

$$V_{DCt} = \frac{\frac{\partial C_{res}}{\partial z} \cdot V_B + \frac{\partial C_{ts}}{\partial z} \cdot V_S(x,y)}{\frac{\partial C_{res}}{\partial z} + \frac{\partial C_{ts}}{\partial z}}. \tag{2.32}$$

As can be seen from equation 2.32 the readout potential of the KPM method is a weighted average of the background potential and the potential under the tip. Further, no simple mathematical augment can be applied as with EFM in order to get quantitative information, if the potential on the surface is not known beforehand as demonstrated by G. Koley *et al.* [2]. Therefore the potential readout from the KPM method is to be used to get potential differences. Using equation 2.32 and the equations from [42] the measured surface potential V_{DCt} can be plotted as a function of the distance from the surface at different average surface potentials V_B. Figure 2.17 shows the plots of the calculated value of the measured surface potential under the tip as a function of the average surface potential of the whole sample and tip surface distance. For figure 2.17 A the average surface potential V_B is 0.1V with varying surface potentials V_S of 1, 0.8, 0.6, 0.4, 0.2 and figure 2.17 B surface potential at 0.1V with varying average surface potentials V_B of 1, 0.8, 0.6, 0.4, 0.2 Volt.

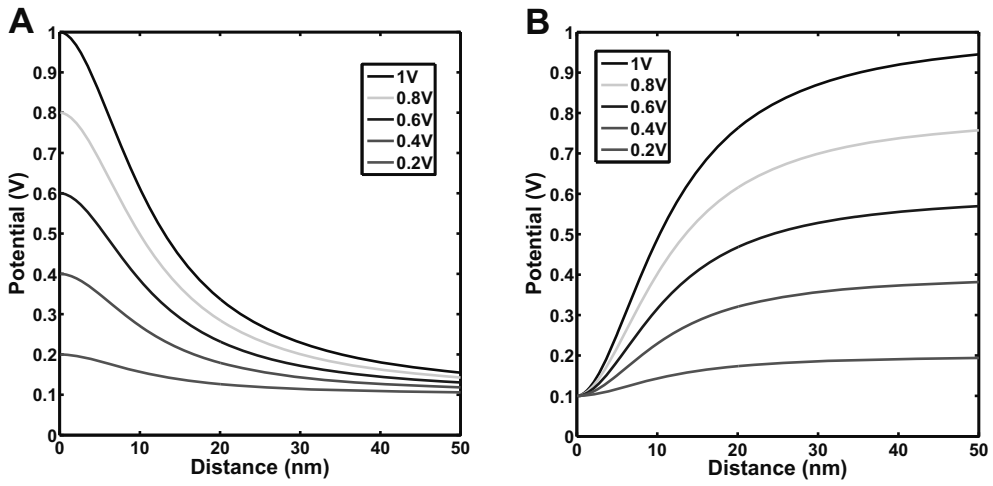

Figure 2.17: Graphs of the measured surface potential V_S under the tip as a function of the average surface potential V_B and tip surface distance A) average surface potential $V_B = 0.1$V with varying surface potentials $V_S = 1$, 0.8, 0.6, 0.4, 0.2 B) surface potential $V_S = 0.1$ V with varying average surface potentials V_S of 1, 0.8, 0.6, 0.4, 0.2 Volts.

Looking at the graphs in figure 2.17 the KPM method should have good resolution as long as the change in topography is small (in the tens of nanometers)

and the difference between surface potential under the tip and the average surface potential V_B is small. But as the tip operates in non-contact mode it has an average distance from the surface of around $5 - 10$ nm [14], so the measured potential V_{DCt} will not be the true value of the surface potential, but rather a combination of the local potential V_S and the average potential V_B. The method is still a very useful tool. It has been used to has been used to measure potential differences in the 10 mV range [89], though interpretation of the data should be done with care.

2.5 Experimental Considerations of EFM and KPM

Both EFM and KPM methods have of course their strengths and weaknesses and as their field of application is overlapping, both can be used to measure (surface) potential differences. A short comparison of the two methods is given here. The measured signal for the two methods depends on the distance of the tip and sample (see equations 2.23 and 2.29). The EFM-phase measured signal has a dependence on the distance as $\frac{1}{r^3}$, while the KPM measured signal goes as $\frac{1}{r^2}$. As mentioned the measured signal originates not only from the tip, but it is also influenced by the cone and beam of the cantilever. These effects are especially an issue if the sample has a height variation. As these effects also follow $\frac{1}{r^3}$ and $\frac{1}{r^2}$ for EFM-phase and KPM respectively, the unwanted signals drop faster for EFM phase ($\frac{1}{r^3}$) than for KPM ($\frac{1}{r^2}$). So when imaging samples with a height variation the EFM-phase method has some advantage. On the other hand, the KPM method has better resolution because it operates much closer to the surface [87, 2]. Another difference between the two methods is that the EFM-phase method is easier to operate, since it has fewer interlinked parameters, which have to be adjusted. The KPM method suffers from the adjustment of the parameters on the lock-in amplifier, such as the setting of the right phase of the reference signal of the lock-in amplifier. The KPM method is faster, as it does not require two scans (an image with the EFM-phase method with a resolution of 512×512 pixels takes more than half an hour at a scan rate of 0.5Hz as opposed to a KPM image that only takes half the time to obtain).

Chapter 3

SPM on Biological Structures

Lab on a chip systems utilizing electrical force for the manipulation of biological samples suffer from the fact that the physical properties (e.g. size, permittivity, conductivity) of biological samples are mostly unknown. In order to optimize these devices the physical properties of the biological material in question need to be measured. The fact that knowledge of the properties is rather limited could stem from their complex structure compared to fabricated solid state samples (nanowires/tubes etc.). This chapter will present the investigation of the physical properties of two different types of biological structures, human chromosomes and diphenylalanine peptide fibers. The chromosomes preparation were carried out in two different ways, with and without polyamine. The polyamine was used to condense the chromosomes even more[90]. The EFM-phase method was used together with AFM topography data in order to get estimates of different physical properties of dipeptide self assembled structures [91] and human chromosomes [92]. Moreover, KPM was used in order to probe electrostatic interactions of protein arrays.

3.1 Support Substrate Preparations for EFM

Substrates were fabricated by the use of four inch heavily doped p silicon wafers. These wafers had a 100 nm oxide layer grown, the oxide on one side was removed by HF and a 20 nm layer of titanium was evaporated on the silicon followed by a 1000 nm layer of gold (see appendix B for the complete process recipe). Figure 3.1 shows a schematic drawing of the different layers of the substrate.

Figure 3.1: Schematic drawing of the fabricated support substrate used in EFM-phase experiments.

3.2 EFM on Chromosomes

Several different SPM methods have already been used on chromosomes. AFM (topography) imaging of stained G band patterns of the chromosomes was used to investigate the possibility of obtaining better resolution of the bands [93]. Near-field scanning optical microscopy measurements of the bands [94] and elasticity investigations of chromosome structure [95] have also been reported. An understanding of the properties of the chromosomes is necessary in order to optimize micro-fluidic devices for sorting. Some work has been carried out in order to investigate mechanical and surface properties of chromosomes [95]. But not much work has been done in order to map out the electrical properties of the chromosomes [96]. This chapter will contain descriptions of different methods which have been used to characterize the electrical properties of human chromosomes. First it will contain a description of the chromosome solution preparation, followed by a description of the results obtained by using the EFM method on metaphase chromosomes fixed on a surface [1].

3.2.1 Sample Preparation

The chromosomes used were human metaphase chromosomes. They were prepared with and without polyamide. When one adds polyamide to the chromosomes a condensation of the chromosomes happens [90]. The reason for this choice was that when the C-TAS project started (see chapter 1.1) knowledge of chromosome movement in micro-systems was limited. During the course of this project it was realized that if it should be possible to optimize any devices based on theoretical considerations the particle shape must be rather simple and condense.

For the first experiments without polyamine added to the chromosome solution the preparation of the solution was done in the following way. First the suspension

[1] The work described in this section was done in collaboration with Jacob Moresco Lange and Linda Boye Jensen.

of chromosomes was prepared from human T-lymphocytes (DSMZ: ACC282) by a variant of the method developed by W. Wray *et al.* [97]. The cells were grown in RPMI-1640 media (Invitrogen: 61870010) supplemented with 10% fetal bovine serum (Sigma: F9665) at 37°C and a 5% CO_2 atmosphere. The cells were arrested in log-phase with 0.06 μg/ml colcemide (Sigma: D1925) for 10 hours and collected at 200g for 10 minutes. After removing the media the cells were washed once with serum free media and collected at 200g for 10 minutes. The media was removed and the pellet was exposed to 75 mM KCl (Sigma: P9327) at 37°C, gently vortexed to resuspend the cells and incubated at 37°C for 20 minutes. The cells were collected at 200g for 10 minutes and washed once with hexylene glycol buffer (1.0M hexylene glycol [Sigma: 112100], 0.5mM $CaCl_2$ [Sigma: 21115] and 0.1mM PIPES buffer at pH 6.7 [Sigma: 80637]) at 37°C before resuspending the cells in fresh hexylene glycol buffer. The cells were added to the substrate were they lysed upon contact. Using droplets of the hexylene glycol buffer resulted in a ”pile” of chromosomes with salt and cell debris residues on the top because of the slow evaporation of hexylene glycol. The sample was lastly washed with deionized water.
As the fixation of chromosomes prepared by this method generates a layer of cell debris on top [66], steps were taken in to order remove this layer or at least minimize it so its effect on the measurement would be as little as possible. Several reports contain descriptions of cleaning the top of chromosomes with either trypsin or pepsin [98, 66, 99]. In this project both trypsin and pepsin were tested. Further, trypsin and pepsin also break down proteins [65]. As chromosomes consist of proteins (histones [27]) one has to be careful not to damage the chromosomes structure, otherwise one would just look at bare DNA. For the trypsin treatment a solution of 2.5 mg/ml in water was used. Treatment times of 5, 10, 15 and 20 seconds were applied. The short treatment time made it difficult to control the reaction and the result was that either the treatment was too short or too long. If the chromosomes had too long treatment they would collapse, as figure 3.2 demonstrates.

For the treatment with pepsin a solution of 1 mg/ml in water was used. Here the treatment times were 5, 10, 15, 20, and 25 minutes based on previous work [66, 98]. Figure 3.3 shows different line profiles of the same chromosome for pepsin treatment of increasing time length.

From the test with trypsin and pepsin it was concluded that pepsin was to be used as it was easier to control compared to trypsin in terms of maintaining the structure of the chromosomes. For the experiments with this type of chromosome preparation a treatment time of 20 minutes with pepsin was chosen. As figure 3.3 shows that at around 25-30 minutes the pepsin start eating the chromosomes structure so a treatment time of 20 minutes was chosen so the chromosomes were not destroyed but as much as possible of the cell debris was removed.

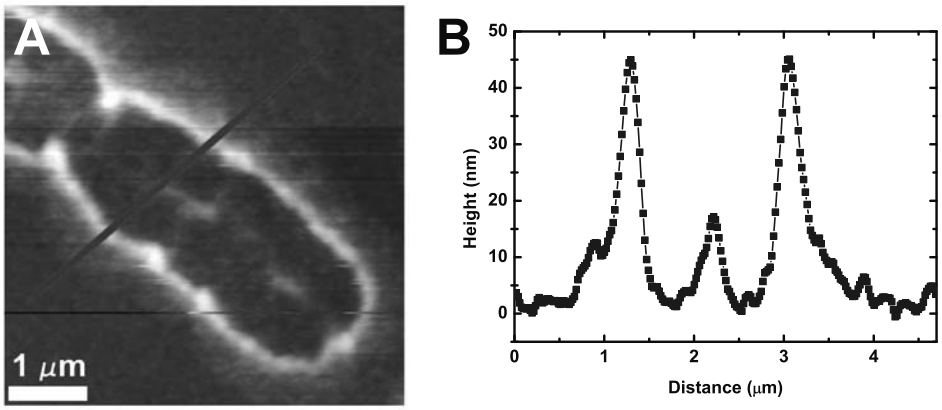

Figure 3.2: A: Topography image of a fixed human chromosome after 20 seconds treatment with a trypsin solution of 2.5 mg/ml in water. B: Line profile from A (blue line).

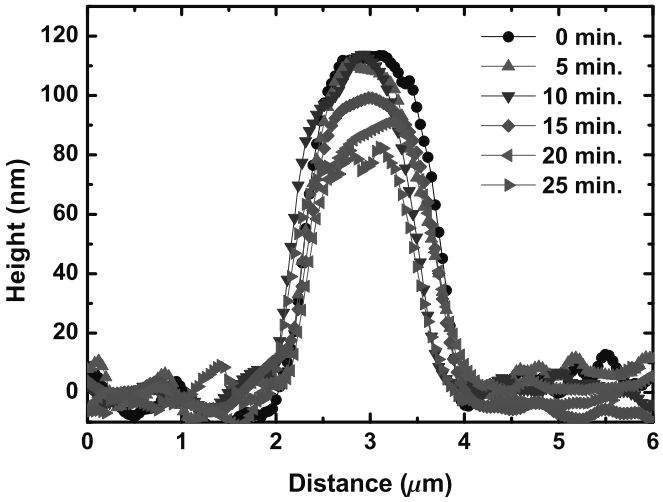

Figure 3.3: Change in topography (line profiles) of a chromosome after pepsin treatments (1 mg/ml in water) of increasing time length of 5, 10, 15, 20, and 25 minutes.

For the chromosomes in polyamine another protocol was used. The suspension of chromosomes was prepared from human T-lymphocytes (Model no. ACC282; DSMZ) as described by L. S. Cram *et al.* [90]. The cells were grown in RPMI-1640 media (Model no. 61870010; Invitrogen) supplemented with 10% fetal bovine serum (Model no. F9665; Sigma). The cells were arrested with 0.1 μg colcemid/ml of culture media for 12-15 hours. The solution was centrifuged at 100 × g for 8 min at 4 $^{\circ}C$. Then 5 ml of Swelling buffer (mix of 55 mM Sodium

nitrate, 55 mM Sodium acetate, and 55 mM Potassium chloride in ratio of 5:2:10) is added to the solution, which is then centrifuged again at 100 $\times$ g for 5 min at room temperature. The media was removed and polyamine buffer (mix of 0.4 M Spermine tetrahydrochloride and Spermidine trihydrochloride) was then added to the rest. For the EFM measurements the solution was resuspended in fixative (methanol/acetic acid $3:1$), which was necessary in order to get sufficient and even spreading of the chromosomes. The sample was lastly washed with deionized water. This sample was not treated with pepsin for cell debris removal, as it is expected that the layer would be minimal as cell debris have been removed by centrifugation.

3.2.2 Measurement

The scanning probe microscopy system used in this project to obtain the data was a CP-II SPM system from Veeco. AFM cantilevers were obtained from Budgetsensors (www.nanoandmore.com, model BS-*Electri*Multi75) which have a platinum coating. Analysis of the obtained data from the SPM system was carried out using the "SPIP" software unless otherwise stated [15].

In order to estimate a value for the dielectric constant of the chromosomes, one needs the value of $\frac{Q\pi r_{tip}^2 \epsilon_0}{k} = K_{can}$ (see equation 2.23), which depends on the characteristics (Q factor, tip radius, and spring constant) of the AFM cantilever used. Previous reports on using EFM for quantifying scanned samples have used the properties of the AFM cantilevers stated by the manufacturer [41, 39]. Unfortunately, these parameters can vary with more that a factor of 2 (see www.budgetsensors.com). So in order to obtain better estimates for the dielectric properties of the scanned samples these parameters were mapped out using two different methods. With the first method the different parameters were measured directly, while with the second method the electrostatic forces were used to get an estimate of the constant K_{can} that depends on the different parameters.

In the first method the tuning of the resonance frequency of the cantilever was measured (see figure 2.7) before and after the data was obtained in order to estimate the quality factor (Q, based on the amplitude of the resonance frequency as a function of frequency $Q = \frac{f_{res}}{\Delta f_{half}}$). The tip curvature was estimated from Scanning Electron Microscopy (SEM) images of the cantilever tip. The spring constant of the cantilever was measured by deflecting the cantilever in question with another cantilever (reference) with a well defined spring constant using the CP-II laser deflector readout. The principle of the setup is shown in figure 3.4.

The spring constant is estimated by the following formula according to A. Torii *et al.* [100]

$$k = k_l \cdot \frac{1 - c_s}{c_s}, \tag{3.1}$$

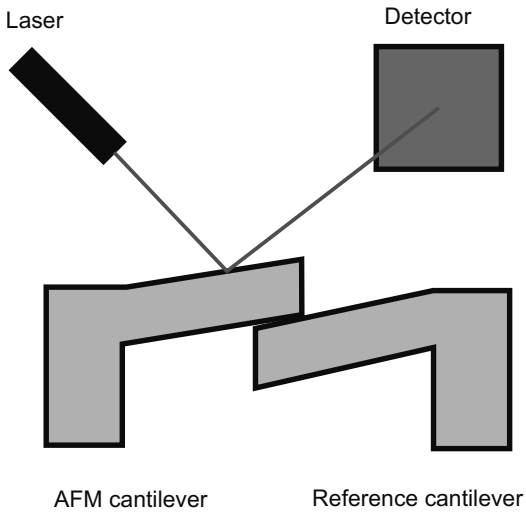

Figure 3.4: Sketch of the working principle behind direct measurement of the spring constant of the AFM cantilever. It is deflected by the use of another (reference) cantilever and the deflection is measured.

where k_l is the spring constant of the reference cantilever and c_s is slope of the force curve. The SPM system's piezo element is used for the deflection of the AFM cantilevers. The procedure is: first a calibration curve of the piezo element is obtained on a solid surface. The AFM cantilever is then deflected by three other reference cantilevers with different spring constants and force curves are obtained. A typical force curve is shown in figure 3.5. The slopes of the obtained force curves are divided by the slope of the calibration force curve in order to get the real slope. The AFM cantilevers spring constant is then found by equation 3.1 from each of the reference cantilevers and an average spring constant of the AFM cantilever can be found.

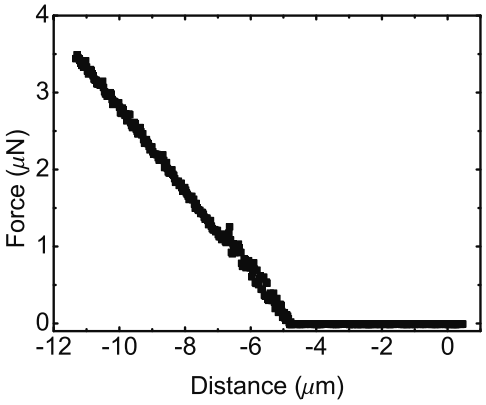

Figure 3.5: Force distance curve of an AFM cantilever being deflected by another cantilever.

Here four AFM cantilevers were investigated. Table 3.1 shows the different

Number	1	2	3	4
K_{can} ($\frac{C^2m^2}{J^2} \cdot 10^{-24}$)	1.87	1.90	9.89	8.08
Error ($\mp \cdot 10^{-25}$)	7.39	0.79	12.74	1.86

Table 3.1: Table of the different K_{can} estimated by measuring the tip radius, the Q-factor, and the spring constant of the AFM cantilever. Used when analyzing EFM data obtained from chromosomes prepared without polyamine.

k_{can} values obtained by the first method and used to analyze EFM data obtained from chromosomes prepared without polyamine.

The second method was developed, as obtaining the values for tip radius, the Q-factor, and the spring constant of the AFM cantilever separately is a rather time consuming process. This method uses the principle that one only needs to know the value of K_{can} in order to estimate the dielectric constant of the sample. The method estimates K_{can} by varying the tip height over the surface as well as the potential between the tip and backgate. The method works by raising the tip one step at a time over the surface and then varying the potential. This is continued for some steps. The raised steps used in the project were 10 nm, 30 nm, 50 nm, 100 nm, and 150 nm. The potential was varied in steps of 1 V from zero to 10 V. According to the theory derived in section 2.3 applied to just the tip over the substrate the phase is

$$\phi \approx \frac{Q\pi r_{tip}^2 \epsilon_0}{k} \frac{1}{(z + d/\epsilon_{SiO_2})^3} \cdot V_s^2 = K_{can} \frac{1}{(z + d/\epsilon_{SiO_2})^3} \cdot V_s^2. \tag{3.2}$$

As discussed in section 2.3.2 the lift phase is not only depending on the tip-substrate interaction, but also on the cone- and cantilever-substrate interaction. As stated in that section these contributions are mostly constant so measuring the lift phase at different potentials and height over the surface one can get an estimate of the constant K_{can} by the slope of figure 3.6.

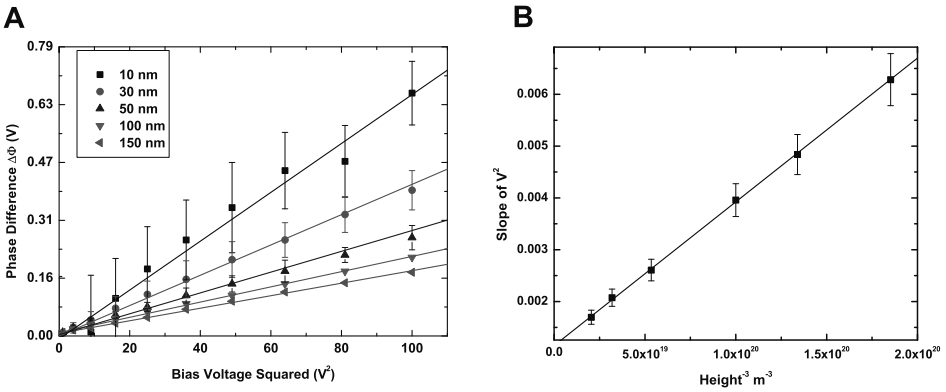

Figure 3.6: A) plot of phase change measured relative to the surface (surface tip distance equal zero) as a function of potential change between the tip and substrate at different distances over the surface. B) plot of the slopes of the different lines from A as a function of the height to the minus third.

Figure 3.6 A shows a typical plot of phase change measured relative to the surface (surface tip distance equal zero) as a function of potential change between the tip and substrate at different distances over the surface. Figure 3.6 B shows the plot of the slopes of the different lines from figure 3.6 A as a function of the height to the minus third. The slope of figure 3.6 B gives the constant K_{can}, as equation 3.2 implies.

Number	1	2	3	4	5
K_{can} ($\frac{C^2m^2}{J^2} \cdot 10^{-23}$)	1.1	1.3	10.1	0.8	2.7
Error ($\mp \cdot 10^{-24}$)	2.29	1.18	12.81	0.82	0.75

Table 3.2: Table of the different K_{can} values measured varying the height and potential and used when analyzing EFM data obtained from polyamine buffer prepared chromosomes.

Table 3.2 gives different values of K_{can} for the different AFM cantilevers used in this project. One can calculate an average value of the K_{can} for the AFM cantilever used from the properties given by the manufacturer [83] and the average values of the quality factor (120) found from the previous method. Cantilever 3 from table 3.2 might have been damage as it is a factor 5-10 higher that the rest.

However using the values of the properties of the cantilever from the producer gives that is value is possible for the cantilever. This gives a range for K_{can} of $1.58 \cdot 10^{-23}$ to $3.475 \cdot 10^{-23} \frac{C^2 m^2}{J^2}$, which fits well with the values of table 3.2. To compare the two methods, they were applied to the same cantilever (number 5 in table 3.2). The first method gave a value for K_{can} of $2.186 \cdot 10^{-23} \frac{C^2 m^2}{J^2}$ with a variation of $\pm 5.315 \cdot 10^{-24} \frac{C^2 m^2}{J^2}$ due to the uncertainties on the measuring of the different constants. The second method gave a K_{can} of $2.769 \cdot 10^{-23} \frac{C^2 m^2}{J^2}$. Although the average values for K_{can} of the two methods are different, due to the uncertainties of the measuring methods they are within range of each other.

3.2.3 Optimization of Scan Parameters

In order to optimize the scan parameters investigations were made in order to determine the effect of the different parameters (scan rate, potential between the tip and backgate, and lift height). The scan rate was set to 0.6 Hz, as at this rate the trace and retrace of the topography signal was similar. For the potential it can be deduced from formulas 2.20 and 2.23 that it needs to be as high as possible in order to get a good signal as possible. Further the value of the potential also depends on the thickness of the oxide layer. If the oxide layer is too thick it will dominate the phase signal while if it is too thin there will be a chance of electrical discharge between the tip and the backgate making holes in the oxide. In the experiments made during this thesis the thickness of the oxide layer was chosen based on the works of others which had used this method in the past [87, 41, 85, 39]. One could have chosen to optimize the relation between the applied potential between the tip and backgate as well as lift height, but in this project it was decided not to investigate this. Test scans at different potentials and scan heights showed that at lift heights of $30 - 40$ nm applied potentials between the tip and backgate of $3 - 4$ V made holes in the substrate indicating that electrical discharge between the tip and the backgate occurred. For lift heights of $50 - 60$ nm potentials between the tip and backgate of $3 - 4$ V did not made the same holes in the substrate. For this reason the potential used if the lift heights were $30 - 40$ nm was to 2 V while for lift heights of $50 - 60$ a potential of 4 V was used.

According to equations 2.20 and 2.23 the lift height needs to be as low as possible in order to get the best signal change when scanning different samples. However the phase signal will have some crosstalk between the topography phase and the EFM phase if the tip is too close to the substrate and sample. The way this cross talk was minimized was that the phase at the surface was compared with the phase at different lift heights until the features of the non lift height image disappeared. An example of the optimization of the lift height is shown in figure 3.7, where the phase at different heights on a dipeptide tube is plotted. As the graphs of the figure show, the dip on the right side is visible until a lift height of 60 nm is used.

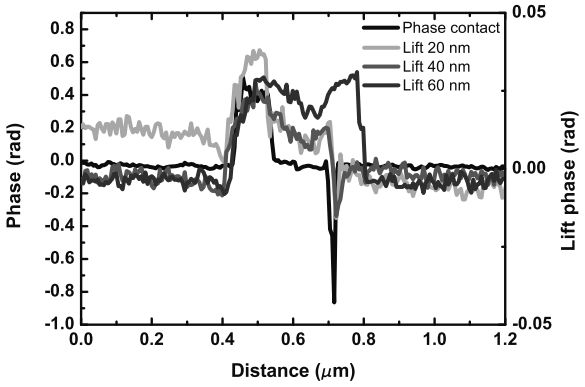

Figure 3.7: Line profiles of a dipeptide tube at different lift heights (non, 20 nm, 40 nm, and 60 nm).

With this procedure it is of course not totally safe to assume that the crosstalk of the different phase signals is eliminated. However, as the features of the topography phase do not show clearly they are probably minimized enough that one can use the data for some analysis.

3.2.4 Results and Discussion

All SPM images shown in the first part of this section were obtained at 512×512 pixels. The scan rate was 0.6 Hz, the potential applied during the lift-height scan was 2 V, and the lift-height 30 nm (over the set point see section 2.2.2). The stated values were found by optimization of the different parameters in order to get the best signal to noise ratio as described in section 3.2.3.

Figure 3.8 and 3.9 show histograms of the dimensions (length, width, and height) of chromosomes prepared without and with polyamine.

Figure 3.8 A shows the histogram of the length of the chromosomes prepared without polyamine estimated from topography images. As can be seen there exists quite a spread of the length from 2 to 7 μm with no clear trend. For the width and height the estimated sizes are more uniform with less spread.

Figure 3.9 shows histograms of the dimensions (length, width, and height) of the polyamine buffered prepared chromosomes.

As can be from figure 3.9 A, B, and C the total spread in size is not as for the polyamine buffer prepared chromosomes big as for the non polyamine prepared ones. The length varies from around 1.5 to 4 μm, while for the non polyamine prepared ones the variation is from 2 to 7.5 μm. However, for the width and height

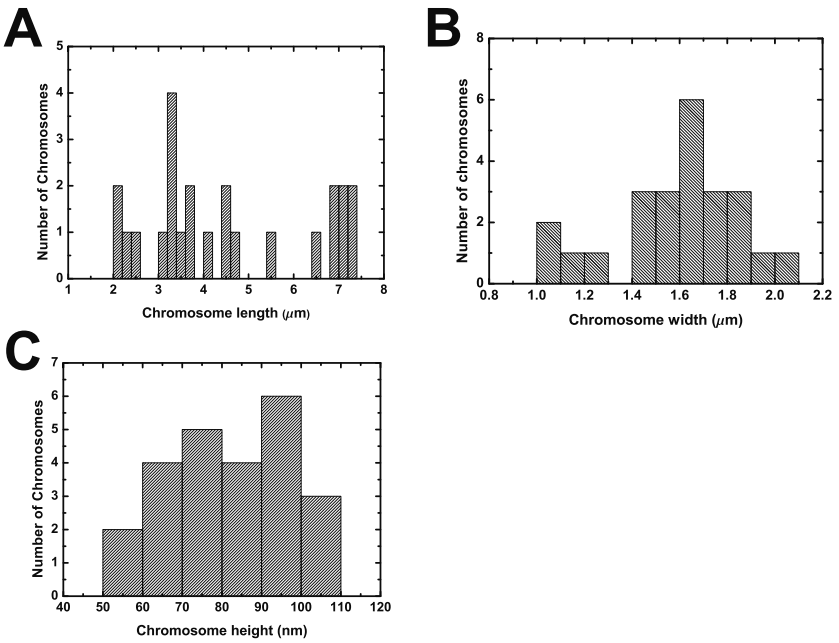

Figure 3.8: Histograms of the dimensions of chromosomes prepared without polyamine: A length: B width: C height.

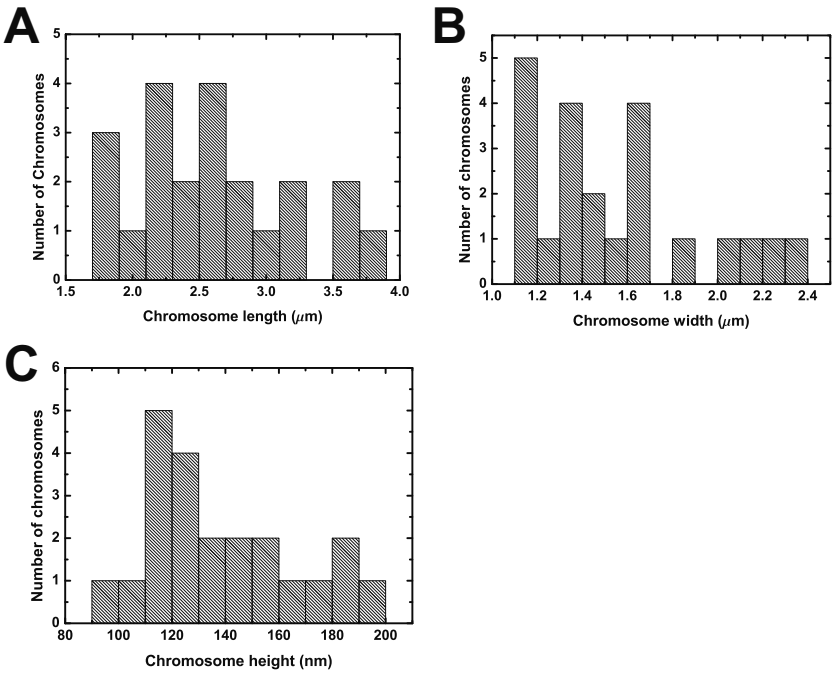

Figure 3.9: Histograms of the dimensions of the polyamine buffered prepared chromosomes: A length: B width: C height.

the spread is more even for the polyamine prepared ones, they are a bit higher while the width is in the same range.

These dimensions of course do not represent the true dimensions of the chromosomes as the tip convolution makes estimates of the length and width hard. As the chromosome structure is soft [101], the exact height depends on the force used. The force depends on the spring constant of the cantilever, and as this can vary with an order of magnitude [83] it can be hard to estimate the exact size of the chromosomes. However, the average values have been used in this thesis for some theoretical calculations on the chromosome movement under an electrical force (see chapter 4). This decision can be defended from the fact that given the cantilever dimension, the tip convolution is not expected to change the chromosome dimensions by more than 1-2 μm, which is small enough to account for the size variations in any case found in these biological objects.

Figure 3.10 A shows a typical topography image of a sample with some chromosomes on a surface. Figure 3.10 B shows the phase lift-mode (EFM) image of the same sample while figure 3.10 C shows the phase shift obtained during a topography scan.

The phase shift in lift mode and the phase shift during the topography are shown in figure 3.10 B and C. There doesn't seem to be an overlap of the two signals, although one cannot be certain.

Topography and lift mode phase images of different chromosomes with different cantilevers were obtained under ambient conditions. The phase shift in lift mode and the corresponding chromosome height for each chromosome were obtained by taking the average across the middle of two of the arms of the chromosome (10 pixel to each side of the grey line in figure 3.10 A and B). Using equations 2.21, 2.22, and 2.23 the dielectric constant was estimated for each of the chromosomes. The chromosomes were investigated with different cantilevers with relatively uniform resonance frequencies (± 15 kHz). Five of the chromosomes were mapped out twice with a cantilever with a relatively higher (around 3 times higher or 265.1 kHz) resonance frequency. This was done in order to check if the dielectric constant changed due to the frequency of the cantilever.

Figure 3.11 shows the different dielectric constants obtained for different chromosomes with respect to their height. The error bars are calculated on the background of measurement uncertainties of the spring constant, the quality factor, the tip radius, and the oxide thickness. These have been calculated to be $\pm 5\%$ to $\pm 8\%$. Uncertainty values found for the lift-height and the sample height were $\pm 1\%$, and for the potential difference an uncertainty of $\pm 5\%$ was chosen.

As figure 3.11 shows, the value for the dielectric constant is 10 (± 4). Moreover

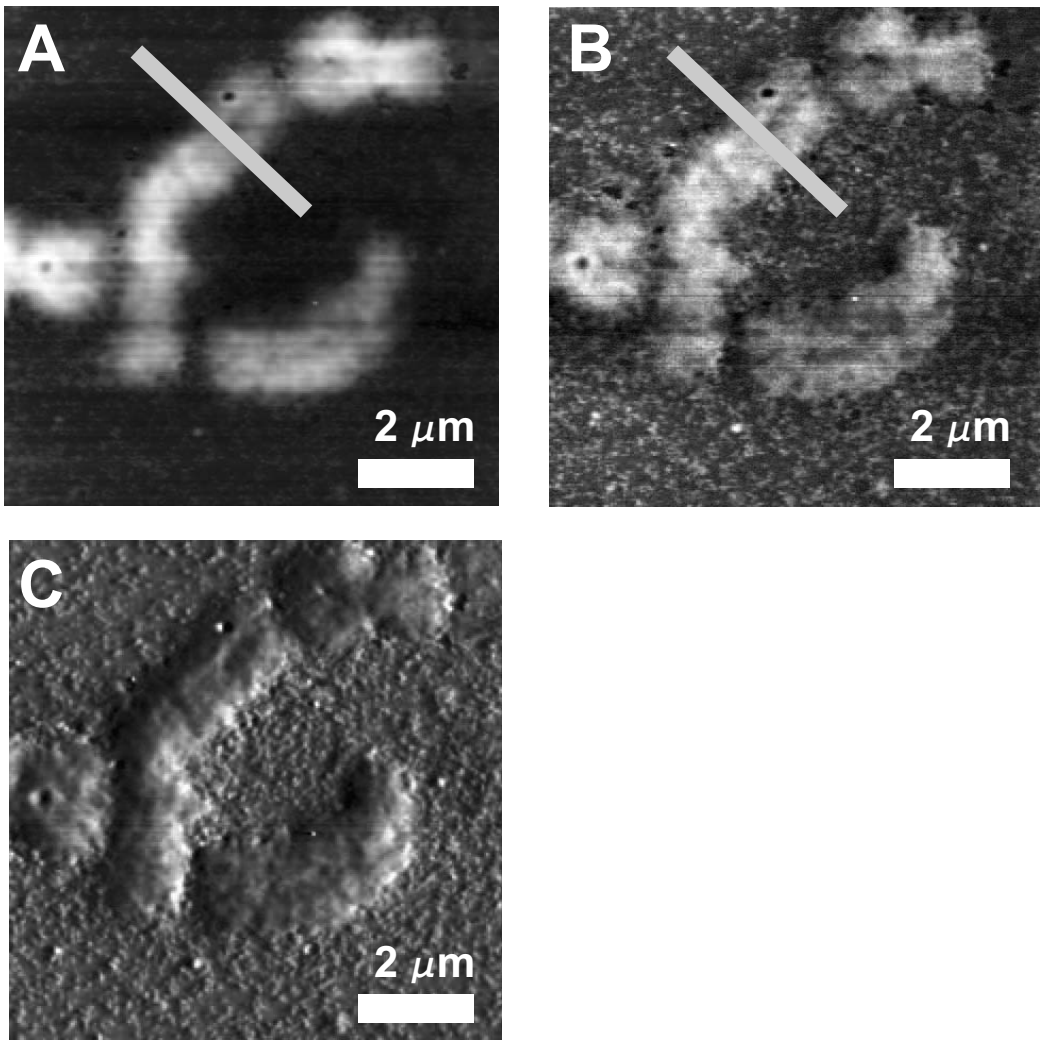

Figure 3.10: A) Topography image of chromosomes dispersed on a SiO_2 surface with back-gate; B) Phase shift image in lift-mode of the same chromosomes as in A. The grey line is used to calculate the average height and lift phase for the chromosomes; C) phase shift image of the same chromosomes as in A.

the dielectric constant does not seem to vary with the chromosomes height or the cantilever resonance frequency. The flat curve of the dielectric constant for different chromosome heights indicates that no artifacts influence the measurements. The spread in the values of the dielectric constant can be contributed to different effects. First of all, a chromosome is not a uniform material. On the contrary, it is composed of a complex mixture of proteins and DNA and the dielectric constant may depend on the DNA-protein ratio at the point of measurement. This could give rise to the variation in the dielectric constant. Another thing which will influence the result is that the tip is not exactly flat but rather a bit curved. However,

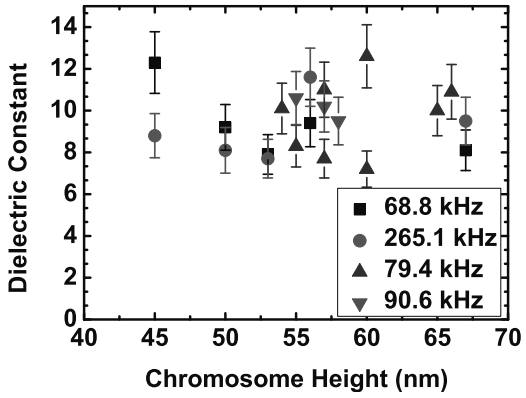

Figure 3.11: Measured dielectric constant of different chromosomes as a function of the height of the chromosome in question.

according to other researchers (C. Staii *et al.* [41] and T. S. Jespersen *et al.* [39]), who have reported good agreement between this assumption (flat tip) and experimental observations when investigating nanoparticles, this does not seem to be an important source of error. Finally, the sample preparation may also affect the chromosomal integrity, which could influence the measured dielectric constant. For example the chromosomes suspension contains other biological material like the layer of cell debris. This layer is not uniform and its thickness is small (around 5 nm) compared to the chromosomes, making it hard to predict the impact it will have on the measured data.

The images shown in the second part of this section were obtained at 512×512 pixels. The scan rate was 0.5 Hz, the potential applied during the lift-height scan was 3 V, and the lift-height 100 nm. The stated values were found by optimization of the different parameters in order to get the best signal to noise ratio.All experiments were done under ambient conditions. Measurements and analysis were carried out on 20 chromosomes.

As mentioned earlier (section 1.1) it was during the course of this project decided that another type of buffer (polyamine) prepared chromosomes were to be used. Therefore another set of experiments was carried out on human chromosomes based on this buffer. During this set of experiments a MATLAB$^{\mathrm{tm}}$ (see appendix D.1) program was developed by Sonia M. Buckley. The program was based on the idea that the line profile averages were not precise enough. Figure 3.12 a) shows a typical topography image of a sample with some chromosomes on a surface. The chromosomes are around $100 - 200$ nm in height and a few μm long and wide. Figure 3.12 b) shows the phase lift-mode (EFM) image of the

same sample.

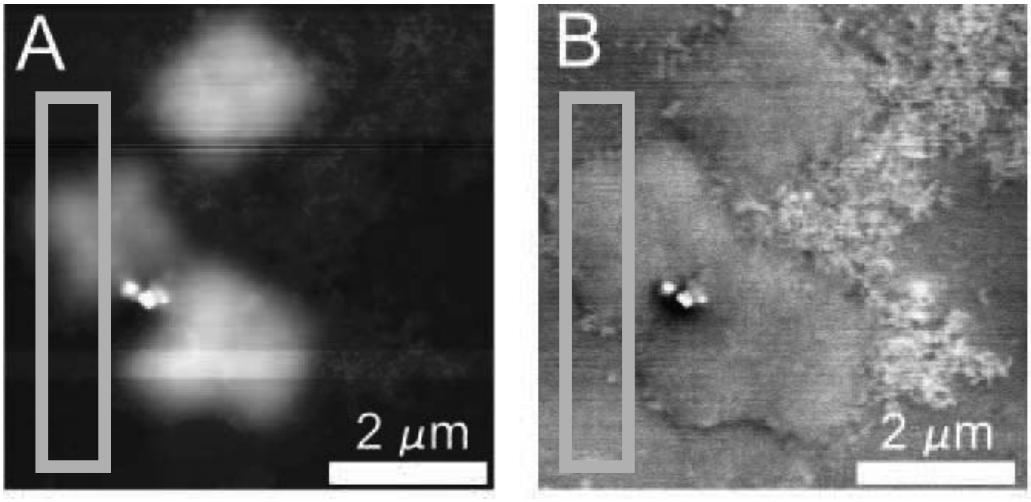

Figure 3.12: A) Topography image of chromosomes dispersed on a SiO_2 surface with back-gate; B) Phase shift image in lift-mode of the same chromosomes as in A. The images are reproduced using SPIP[15].

To extract the topography and lift phase shift, the data was analyzed with the Matlab^{tm} program. The program averages a selected area of the images of the height and the phase change between the substrate and sample. Further, the variation in the height and the phase change with respect to the average was used to calculate the uncertainties. The grey squares in figure 3.12 A and B show a typical area of analysis. The program calculated an average value for the dielectric constant using equation 2.23 to 8.4 with an uncertainty of +5/-2.4 and average uncertainty of 1.4. The maximum value found was 11.7 with an uncertainty of 1.7, while the lowest value found was 6.8 with an uncertainty of 0.8.

The program was also used on some of the previous measurements on chromosomes without the polyamine buffer. It gave an increase in the dielectric constant varying from 0.2 to 0.4 depending on the chromosome. This was not followed further as there were no experiments done with these chromosomes and the differences were in any case within the uncertainty.

3.3 EFM on Peptide Superstructures

This section describes the work done on dipeptides by EFM-phase [1].

[1]The work described in this section was done in collaboration with Jason Jensen and Jaime Castillo.

3.3.1 Sample Preparation

For the EFM experiments, several different types of peptide superstructures were used: Hollow peptide tubes, silver filled peptide tubes, silver wires, and peptide particles. The peptide solution was prepared by dissolving the lyophilized form of the diphenylalanine (Bachem (Cat. No. G-2925, Germany) in 1, 1, 1, 3, 3, 3-hexafluoro-2-propanol (HFIP) (Fluka Cat. No. 52517) at a final concentration of 100 mg/mL. Peptide stock solution was diluted in distilled water to a final concentration of 2 mg/mL. For the casting of silver nanowires inside the peptide nanotubes an aliquot of 10 μL of a boiling solution of AgNO3 (Aldrich Cat. No. 204390) was added to 90 μL of a peptide nanotubes solution (aged for 1 night). After this 6 μL of a 1% solution of citric acid (SigmaAldrich Cat. No. C83155) was added until a final concentration of 0.038% was reached to serve as a reducing agent [102]. For the enzymatic degradation of the peptide nanotubes the silver peptide nanotubes were incubated with Proteinase K (SigmaAldrich cat. No. P6556) at a final concentration of 100 μg/mL for 1 hour at $37°$C. The solutions with the peptides and silver wires were then added onto the fabricated substrates.

For the peptide particles a fresh stock solution was prepared by dissolving the lyophilized form of the Boc-Phe-Phe-OH peptide (Bachem) in 1, 1, 1, 3, 3, 3-hexafluoro-2-propanol (HFP) (Fluka Cat. No. 52517) at a concentration of 50 mg/mL. Then the peptide stock solution was diluted in 50 $\%$ ethanol to a concentration of 10 mg$/$mL[22]. The solution with the peptides particle was then added onto the fabricated substrates.

3.3.2 Measurements

The measurements were performed as described in section 3.2.2, with the same experimental setup and type of cantilevers.

In order to obtain the dielectric properties of the peptides, the properties of the AFM cantilever (Q factor, tip radius, and spring constant) were mapped out as described in section 3.2.2.

3.3.3 Results and Discussion

All SPM images shown in this section were obtained at 512×512 pixels. The scan rate was 0.4 Hz, the potential applied during the lift-height scan was 4 V, and the lift-height 60 nm (over the set point see section 2.2.2). The stated values were found by optimization of the different parameters in order to get the best signal to noise ratio.

A total of 22 polypeptide tubes were scanned and their topography height was in the range of 50 to 190 nm. A topography scan and a lift phase scan of a single

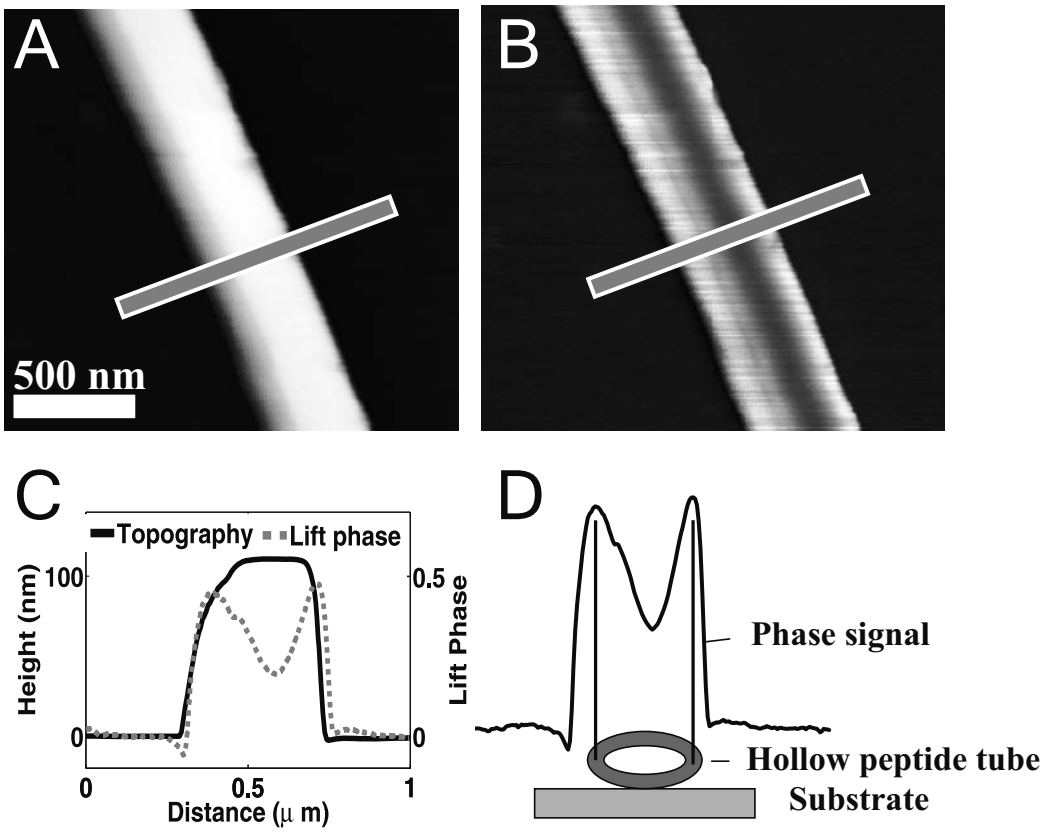

Figure 3.13: A) Topography image of a peptide tube; B) lift phase image of a peptide tube; C) the grey line profile from A and B; D) sketch of the expected hollow structure of the peptide nanotube as interpreted by the lift phase signal.

hollow peptide nanotube are shown in figures 3.13 A and B respectively, while line profiles outlined in these figures are plotted in figure 3.13 C. A dip in the phase line profile is observed in the center of the peptide nanotubes. From equation 2.18 the dip in the phase can be explained by a change in the capacitance between the tip and substrate, which in turn from equation 2.23 indicates a change in the dielectric properties of the tube. Such a change can be attributed to the presence of hollow tubes, as shown in figure 3.13 D, since in that case the permittivity of the tubes would decrease in the middle, where air is present. This conclusion is supported also by the work of M. Reches *et al.* [13] and Y. Song *et al.* [103], who indeed report that the tubes are hollow. Figure 3.14 shows the size of the dip in phase as a function of the tube height.

An indication of the phase decreasing as a function of the different fiber height is illustrated in figure 3.14. As seen, the scanned fibers' phase signal down to around 60 nm in height showed the same change in shape as shown in figure 3.13 C. For fibers with a smaller diameter the dip began to be unobservable, most likely

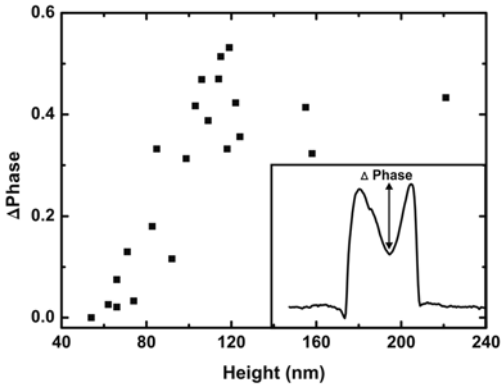

Figure 3.14: Graph of the size of the dip in phase as a function of the tube height. The inset shows how the change in the dip was measured.

due to the dimensions of the AFM tip, as the radius is around 25 nm. The same plot was made with the dip as a function of tube width (diameter), but showed no clear trend, probably caused by the angle of the AFM tip, which makes width assessment difficult [32]. The phase amplitude varied from around 0.2 to 0.65 radians with respect to the substrate. Various comparisons were made between the different measured values for the phase amplitude and fiber dimensions, but no clear trends were identified. This is due to the fact that the self assembling process produces structures with different wall thicknesses.

Figures 3.15 A and B show the height and width distribution of the measured peptide tubes. As can be seen from the distribution the heights of the measured peptide tubes are in the range of around 100 nm while the width of the tubes is more spread out, probably caused by tip convolution.

In order to estimate the dielectric constant of the fibers equation 2.23 was used for the hollow peptide fiber data, mimicking the work done by Staii *et al.* [41] with poly [ethylene oxide] nanofibers. Due to the peptide fibers hollow structure the maximum change in the lift phase was used for fibers (see figure 3.13 D) of various heights. Table 3.3 shows the variation in height and dielectric constant for 9 peptide tubes.

Petide nr.	1	2	3	4	5	6	7	8	9
Height (nm)	106	118	119	98	103	85	158	115	83
Dielectric constant	6.4	23.4	4.9	2.1	5.5	8.7	13.8	2.2	1.9

Table 3.3: Table of the height of 10 different peptide tubes as well as the estimated value of a dielectric constant based on equation 2.23.

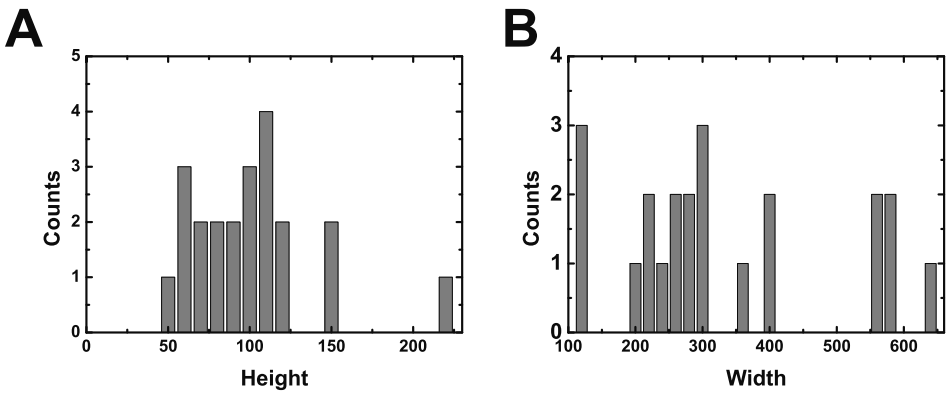

Figure 3.15: Distribution of size of peptide tubes. A) the height distribution of the of the tubes, B) the width distribution of the tubes.

As can be seen from table 3.3 there does not seem to be any clear trend in the dielectric constant nor any dependency on the height of the peptide tube. This suggests that equation 2.23 is not suitable for describing the dielectric properties of these peptide tubes. An explanation for this could be that the wall of the peptide tube is porous, as suggested by theoretical studies done by Y. Song *et al.* [103]. Another reason could be that the model with only oxide, peptide and air in well defined layers is not describing the situation. As several electron microscope pictures show, the peptide tube cross-section structure is far from round but comes in various shapes [103]. This makes it impossible to estimate the exact material composition under the tip.

A second experiment was performed in order to check whether or not equation 2.23 was applicable. According to equation 2.23 the phase signal divided by the square of the voltage should be a constant number. Therefore several scans were made on three different peptide tubes (heights of 85, 115 and 129 nm) with constant scan parameters with the exception of the voltage between the tip and the backgate. This was varied from -4 V to 4 V in steps of 1 V. The results are summarized in table 3.4.

height	potential (V)	-4	-3	-2	-1	0	1	2	3	4
85 nm	Phase/V^2 $\cdot 10^3$	1.5	1.4	1.5	1.8	none	1.8	1.5	1.3	1.4
115 nm	Phase/V^2 $\cdot 10^3$	1.3	1.3	1.4	1.1	none	1.5	1.2	1.3	1.1
129 nm	Phase/V^2 $\cdot 10^3$	0.8	0.7	0.6	1.2	none	0.3	0.8	0.9	0.8

Table 3.4: Table of the phase change of 3 different peptide tubes divided by the potential squared.

The table shows that the phase/voltage^2 signal is not constant with voltage

but varies in some cases significantly. This suggest that there is some other effect that causes equation 2.23 to not be valid. This could be for example the presence of a surface potential on the sample or impurities causing significant noise in the signal.

A simulation of the change in the phase was done in MATLAB$^{\mathrm{tm}}$ and is shown in figure 3.16. Using equation 2.23 one can describe the phase (capacitance) as

$$\phi \approx \frac{Q\pi r_{tip}^2 \epsilon_0 V^2}{k} \frac{1}{(x + t/\epsilon_{SiO_2} + i/\epsilon_{cav} + h_1/\epsilon_p)^3}, \tag{3.3}$$

where ϵ_{cav} is the permittivity of cavity of the tube, i is the height of the cavity, and h_1 is the total thickness of walls of the tube at the tip. Further $h = h_1 + i$ where h is the total height of the tube. Using equation 3.3 one can plot the expected lift phase change for a tube.

Figure 3.16 D shows the expected lift phase signal, plotted with MATLAB$^{\mathrm{tm}}$. Using equation 2.18 one can explain the dip in the phase as caused by a change in the capacitance between the tip and substrate, which in turn from equation 2.23 indicates a change in the dielectric properties of the tube. Such a change can be attributed to the presence of a change in the material composition, as sketched in figure 3.16 D, since in that case the permittivity of the tubes would change in the middle, where another material is present. Using equation 2.23 one can describe the change in phase (capacitance) as

$$\Delta\phi \approx \frac{Q\pi r_{tip}^2 \epsilon_0 V^2}{k} \frac{1}{(x + t/\epsilon_{SiO_2} + i/\epsilon_{cav} + h_1/\epsilon_p)^3}, \tag{3.4}$$

where ϵ_{cav} is the permittivity of the cavity of the tube, i is the height of the cavity, and h_1 is the total thickness of walls of the tube at the tip. Further $h = h_1 + i$ where h is the total height of the tube. If the peptide is modeled as a perfect cylindrical wall with inner radius of r_{in} and outer radius r_{out} then it can be shown with Matlab that the phase minimum will appear at the center of the tube while the phase maximum at the interface between the inner and outer cylinder. Using the recorded AFM data with this information we can extract the values for the inner and outer radii of the tubes and the maximum and minimum phase for a given tube. It is then easy to reconstruct the phase signal for various values of particle permittivity and determine those values that show the best agreement with the recorded data. For the signal of figure 3.16, the extracted permittivity value was between 5 and 7, when one assumes that the cavity of the tubes has a permittivity of 80. The value for the dielectric constant of the cavity was chosen based on the fact that the tube is known to be hydrophilic on the inside [104], so we can assume that water could be trapped inside the cavity. The value extracted for the dielectric constant of the peptide wall seems to be within the limits others have found for protein/peptide materials [105]. It should be noted that a direct calculation of the

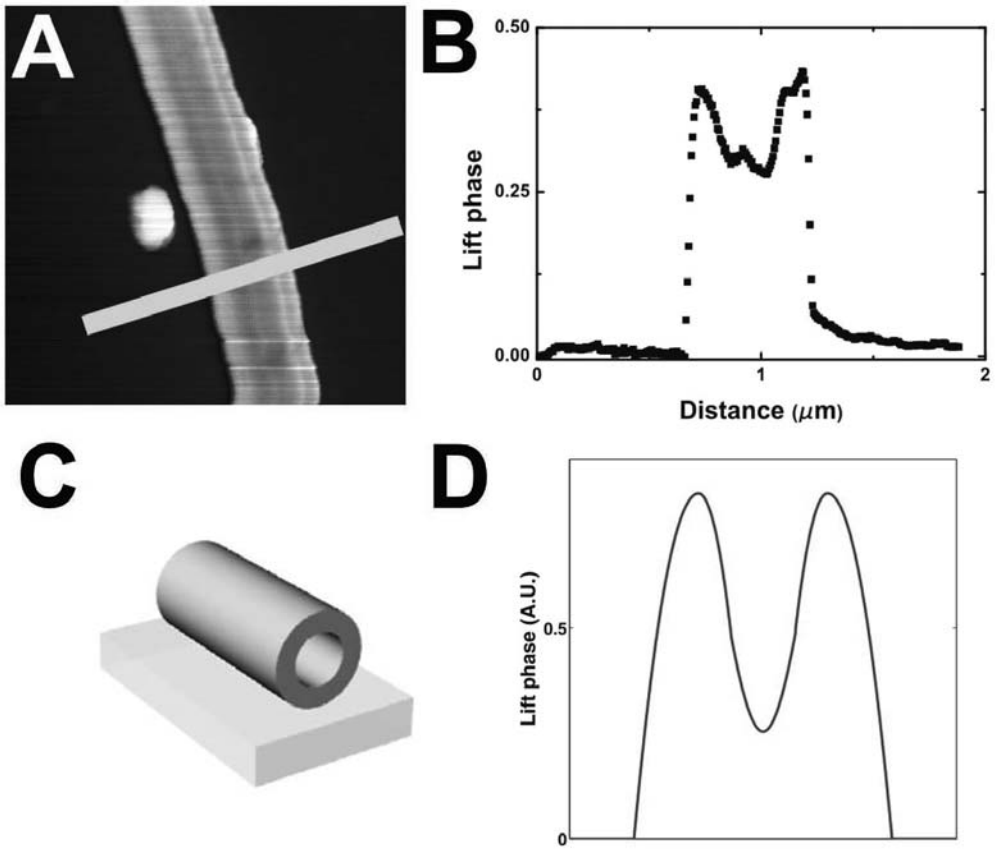

Figure 3.16: A) The topography image of a peptide tube; B) The lift phase image of a peptide tube; C) the line profile indicated by the grey bars in A plotted together with the expected phase signal from a cylinder with outer radius of 100 nm, inner radius of 50 nm, ϵ_{cav} of 80, and ϵ_p of 6; D) schematic cross sectional drawing of the expected hollow structure of the peptide as interpreted by the lift phase signal, using MATLAB$^{\mathrm{tm}}$.

peptide wall permittivity using recorded data at the location of the minimum and maximum phase signal also gives the same range of permittivity values, i.e. 5 to 7. The hollow tube explanation for the observed phase signal is also supported by the work of M. Reches *et al.* [13] and Y. Song *et al.* [103], where they show with TEM that the tubes formed by the fabrication method described in the Materials and Methods section are indeed hollow. Comparing this signal with the one in figure 3.13 C and figure 3.16 B, which are good representations of the phase signal from all scanned peptides it is seen that they only on average look the same as the simulated line profile in figure 3.16, but there are some differences: it can be seen that the measured line profiles are not symmetric, and that in the center of the tube the change in signal is rather sharp compared to the simulated one. This is as discussed earlier probably caused by the tubes being far from perfect cylinders.

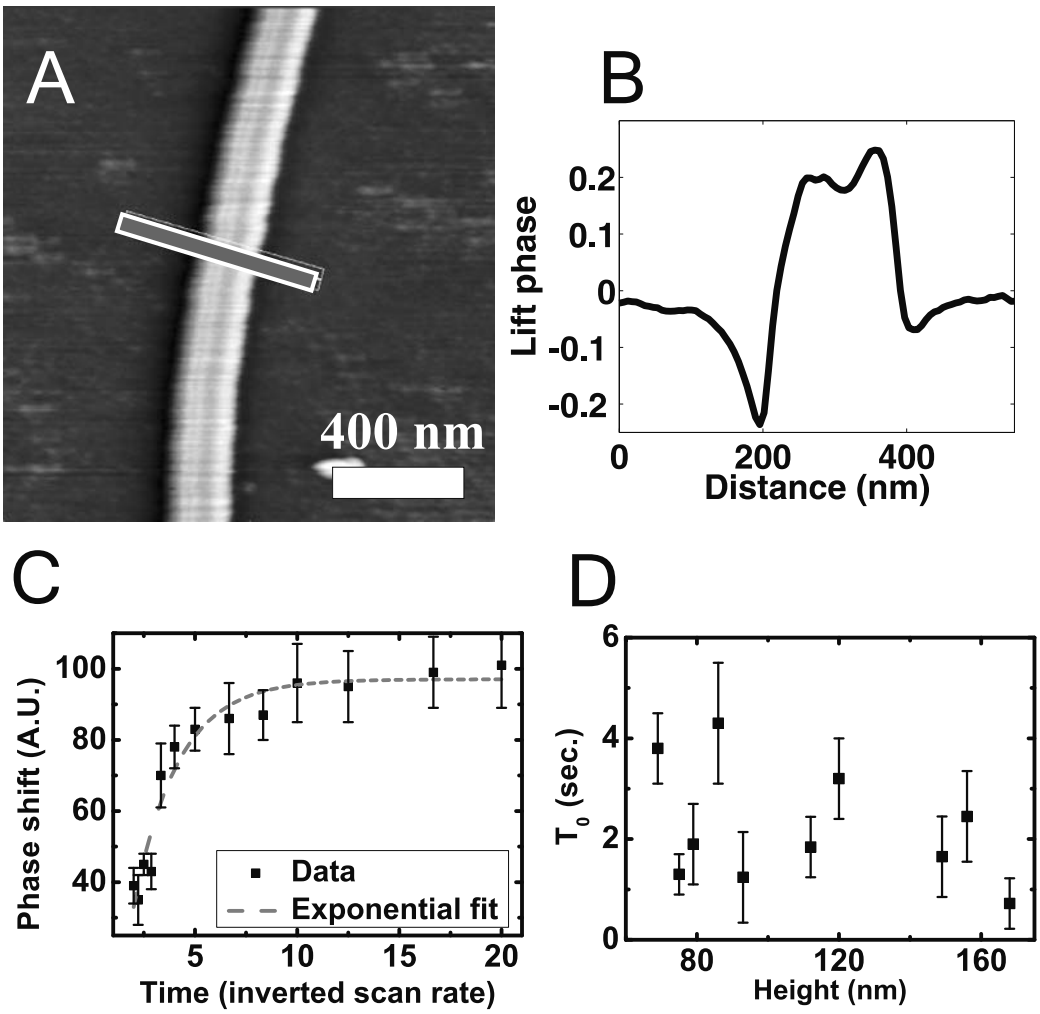

Figure 3.17: A) Lift phase image of a silver filled peptide B) the grey line profile from A C) change in the lift phase as a function of the inverted scan rate for a silver filled peptide tube D) the mean lifetime of different tubes as a function of their height.

A total of 34 silver filled peptide tubes were scanned and their topography height was in the range of 70 to 170 nm. The lift phase for a silver-filled peptide tube is shown in figure 3.17 A, while figure 3.17 B shows the line profile illustrated by the gray line in figure 3.17 A. The phase shift for the silver-filled peptide tube resembles the signal which Staii *et al.* [41] measured for conducting Pan.HCSA/PEO nanofibers using the EFM method, indication that the silver-filled peptide tubes have similar electrical properties.

Figure 3.18 shows the height distribution of the silver filled peptide tubes. As can be seen from the graph the average size is around 120 nm. The signal in figure 3.17 B shows a negative-positive phase shift response. Staii *et al.* [41] explanation for this behavior is the existence of an additional attractive force, which interacts

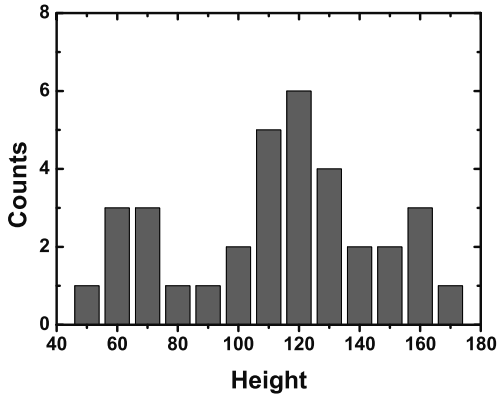

Figure 3.18: Height distribution of silver filled peptide tubes.

between the tip and the silver filled tube, as the tip approaches the tube. Another cause for this negative-positive phase response might be the structure of the tube itself, since the wall of the tube could cause the negative part while the silver in the middle could cause the positive part. In order to investigate this effect further we have plotted the amplitude of the negative part of the phase signal as a function of the inverted scan rate (shown in figure 3.17 C). An exponential decaying function

$$\phi = A_m\big(1 - \exp(\frac{t}{T_0})\big), \tag{3.5}$$

where A_m is a constant and t the inverted scan rate has been fitted to the data and the mean lifetime, T_0, for some of the silver filled peptide tubes has been plotted as a function of their height in figure 3.17 D. This response resembles the charging of a capacitor. Figure 3.17 C therefore suggests that the initial dip in the phase is due to the insulating-conducting structure of the tube. As the AFM tip approaches the silver-filled peptide, a capacitor is formed by the AFM tip and the silver inside the tube, with the wall of the tube acting as the dielectric. Due to the applied voltage (the AFM tip on the one side and a potential on the silver due to the capacitor formed by the backgate and the silver) this capacitor is charging while the AFM tip scans the peptide with the dip size depending on the scan rate.

12 silver wires were scanned during the experiments with a topography height in the range of 30 to 80 nm. The lift phase for a pure silver wire is shown in figure 3.19 A, while figure 3.19 B shows the line profile illustrated by the gray line in figure 3.19 A. Figure 3.19 B shows the lift phase of the silver wire fabricated from the peptide as described by M. Reches *et al.* [13]. The phase shift follows relatively well the topography, as expected for a solid and conducting material [41]. As the silver wires are made inside the peptide shell their topography height tends to be smaller compared to the peptide structures. The typical phase signals

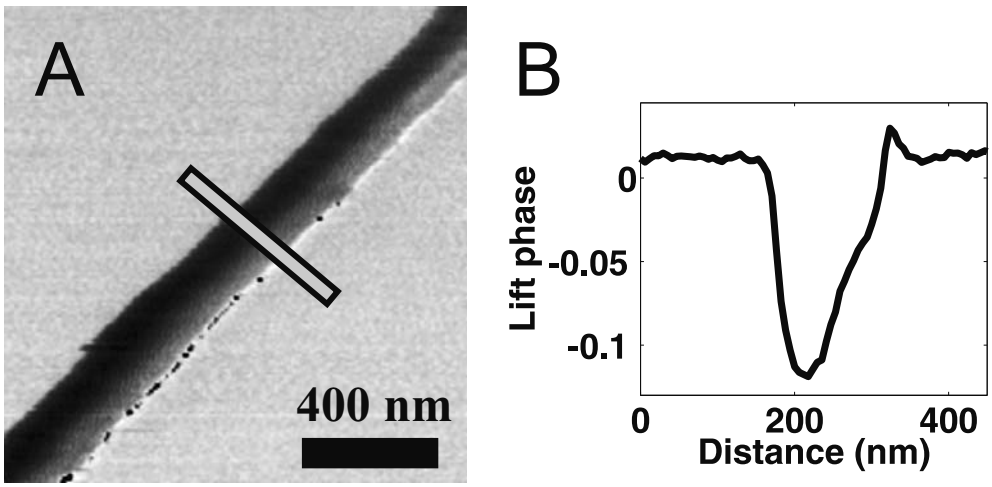

Figure 3.19: A) Lift phase image of a silver wire B) the grey line profile from B.

for the silver wires are of the same amplitude as the peptide tubes making the ratio between the height of the sample and the phase shift a possible way to distinguish between the two types of samples. This seems to hold with the theory of equations 2.22 and 2.23 since silver has a high dielectric constant while the peptide is an insulating material.

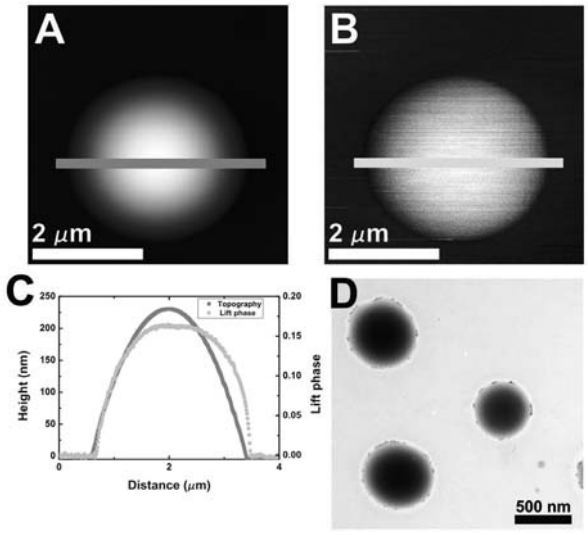

Figure 3.20: A) Topography image of a peptide particle; B) the lift phase image of the same peptide sphere; C) the line profile indicated by the white bars in A and B plotted together; D) TEM image of different peptide particles.

In the second series of experiments a total of 18 EFM scans were carried out on peptide particles, while TEM images were obtained from 30 peptide particles. The topography scanning gave a height for the particles of 25 to 540 nm, while TEM images gave a width of 65 to 650 nm. A typical topography image is shown in figure 3.20 A, while a lift phase image is shown in figure 3.20 B. Figure 3.20 C shows the line profile from figures 3.20 A and B. There exists no dip in the phase signal as has been observed with the tubes (figure 3.16), indicating a solid particle. Figure 3.20 D shows a TEM image of a typical peptide particle. The TEM images also indicate that the peptide particles are solid objects compared to the peptide tubes.

The particles seem to have a radically different signal compared to the peptide tube structures. This indicates that the formation of the particles also occurs differently so they might not form sheets but instead condensate to the particle structures [13, 103].

3.4 KPM on Proteins

Kelvin probe microscopy was carried out on proteins, however as these experiments did not show anything conclusive. So the description of these experiments are in appendix E.

3.5 Summary

In summary we have used EFM to investigate electrical properties of chromosomes fixed on a surface. From estimating the properties of the AFM cantilever (quality factor, spring constant, and tip radius) and from the measured phase shift and by use of the assumption that the tip and surface act as a parallel plate capacitor, we have estimated the value of the dielectric constant of the fixed polyamine buffer chromosomes to be around 8.4 with an average uncertainty of ± 1.4.

It has also been shown that the EFM method can be used to distinguish between three different types of structures (hollow and silver-filled peptides, and silver wires) fabricated using peptides. We have shown that it is possible to detect the geometric structure of hollow peptides using EFM. Further the dip in lift phase for the hollow tubes can be qualitatively explained by previously reported theoretical considerations [39], [41]. Also investigations of the signal from the silver filled tubes shows an exponential behavior with scan rate, which may be explained by charging of a capacitor formed between the AFM tip and the silver core of the peptide tube with the peptide wall acting as the dielectric. Therefore this method

seems to be a promising tool for the characterization of self-assembled micro-devices using peptides.

Chapter 4

Electrical Manipulation of Biological Structures

As stated in chapter 1 the goal of this project is to find an optimal mechanism for sorting of biological material in general and chromosomes in particular. In order to fully utilize the electrical sorting of the material in question its electrical properties must be mapped out. This chapter will contain a description of the methods used in order to test if manipulation of human chromosomes using electrical forces is possible [1]. The fabrication and packaging of the flow systems or chips described in this chapter can be found in appendices A.1.3, B and B.3.

4.1 Introduction

Dielectrophoresis can be applied to sort samples based on their different parameters such as size or dielectric properties [43]. The investigations carried out with SPM indicate that there does not exist any large variation in the dielectric constant (chapter 3) between different chromosomes, but there seems to be a spread in the size distribution. This make either DEP or bumper arrays a possible method to use for manipulation of individual chromosomes. DEP has successfully been used to sort between spherical particles with diameters of 216 nm and 557 nm [43]. It has also been used to sort between the Tobacco Mosaic Virus and the Herpes Simplex Virus [106]. It seems therefore quite plausible that DEP may be a good method to test for the separation of chromosomes, for which the measured size differences are between a few hundred nanometers up to 1 to 2 μm (see chapter 2). As bumper arrays have so far have only been proven on spherical particles [59] it was decided to concentrate the experimental efforts on DEP alone.

[1] The work described in this section was done in collaboration with Sonia Buckley, Jacob Moresco Lange and Maria Dimaki.

4.2 Theory

The flow profile in a micro-fluidic channel is determined by the type of method used to drive the flow and is laminar due to system dimension restrictions which give rise to a low Reynolds number [48]. In these investigations a pressure driven flow is used, which based on the Navier-Stokes equation gives rise to parabolic velocity [48].

The basic equation for flow in a micro-fluidic system is the Navier-Stokes equation [48], which is derived from Newton's second law and is for incompressible fluids given by [48]

$$\rho_m(\frac{\partial v_l}{\partial t} + v_l \cdot \nabla v_l) = -\nabla p_l + \eta \nabla^2 v_l + \rho_l g + f_o, \tag{4.1}$$

where ρ_m is the density of the liquid, v_l is the velocity of the liquid, p_l is the applied pressure, η is the viscosity of the liquid, g is the acceleration of gravity, and f_o is other force densities acting on liquid. In this project it is assumed that f_o is zero. This is not exactly true as the electric fields applied to the liquids will have some effects [48], but the effect is small and is neglected. Further, as the time window at which the experiments are performed is in the range of some minutes the acceleration of gravity will also be neglected. This equation can be used to calculate the flow profile of the liquid, which in the case of the DEP experiments will be a parabolic flow profile as pressure is driving the flow. The viscous drag is applied on particles in the liquid [48]. Using equation 4.1 the viscous (or stokes) drag can be calculated on a spherical particle [48]

$$F_d = 6\pi\eta a_r(v_l - v_p), \tag{4.2}$$

where a_r is the radius of the particle and v_p is the particle's velocity.

4.3 Dielectrophoresis Manipulation

In this section a microfluidic closed channel design reported by N. Demierre *et al.* [16] for dielectrophoretic deflection is used to investigate DEP effects on polyamine buffer prepared human chromosomes. Figure 4.1 shows a schematic drawing of the electrodes layout in the channel system.

As reports from N. Demierre *et al.* [16] and R. Tornay *et al.* [107] show, this design is rather versatile. It can be used for position focusing of particles or particle flow exchange. The design (see figure 4.1) is such that the generated electrical field is almost uniform in the z direction. That means that the electrical force on the particles can easily be calculated from its position in the x and y direction, which can be determined by an optical microscope image. The determination of the particle's position in the z direction because of the uniformity of the electric

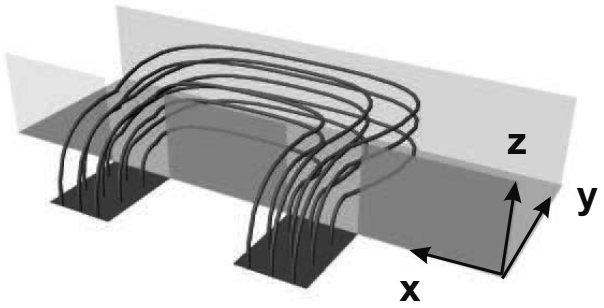

Figure 4.1: Schematic drawing of the electrical field lines (blue) in the fluidic channel with the electrodes (black squares) in the close channel flow design made by N. Demierre *et al.* [16].

field lines in this direction.

Usually, DEP experiments are carried out on open channel system [3] by placing a droplet of the solution onto the electrodes and gently blowing it off before the microscopic investigation. Although this setup is much simpler than the closed channel system, it is not suitable for performing frequency sweeps on samples whose dielectrophoretic behavior is largely unknown. There are three main reasons for this: 1) Unless covered by a cover slip (which introduces other experimental problems) the droplet on top of the electrodes makes top side optical microscope imaging impossible. 2) Even by using an inverted microscope, the droplet in air evaporates with rates depending on the solution in use, which introduces some other forces to the system that can be much larger than the DEP forces 3) Due to the limited time frame for such an experiment not a large frequency range can be examined per experiment, i.e. more than one experiment on different chips is needed to make a full frequency sweep. Despite these arguments, early experiments done by Maria Dimaki on the chromosomes were actually carried out with open channel electrodes. These experiments were largely unsuccessful, as there were indications of positive DEP on the chromosomes but with a very low yield that mostly pointed to random assembly. Therefore, the closed channel system with a flow was chosen in order not to trap but only observe the dielectrophoretic response of the chromosomes with the objective of finding the right parameters, i.e. frequency and voltage, for use in an actual trapping experiment with other electrodes.

4.3.1 1^{st} Generation Chip

To test the system a design was first made which contained two sets of electrodes. The channel split after the electrodes into two outlets. The layout is shown in figure 4.2.

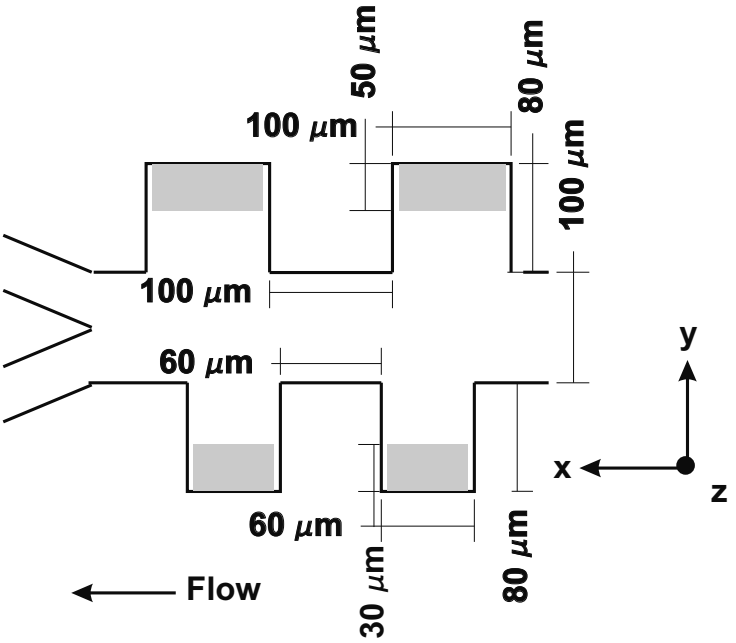

Figure 4.2: Schematic drawing of the first system design for manipulating chromosomes. The grey areas represent the electrodes. The height of the channel structure was 30 μm.

Using the system shown in figure 4.2 the chromosomes can be diverted enough to exit from only one outlet. Moreover, if both positive and negative DEP was observed then chromosomes exhibiting the one or the other behavior can be separated. The dimensions of this setup were chosen based on the literature [16]. However, once the system was tested with beads it became evident that the flow inside the main channel was too "irregular" because of the large channel openings for the electrodes. Therefore the beads, which follow the flow lines (confirmed by COMSOL$^{\text{tm}}$ simulations and shown in figure 4.3), were moving too much in the "y" direction. As the DEP forces on small particles tend to also be rather small, it was not expected that this system would be capable of distinguishing between DEP induced movement in the y direction and normal flow. Therefore, another design with only one set of electrodes on one side of the main channel was fabricated for the experiments.

The following section will present a theoretical calculation for the potential inside the channel that generates the dielectrophoretic force and investigate how this voltage is dependent on the geometry of the system. The optimization of the system dimensions is solely based on maximizing the dielectrophoretic force at

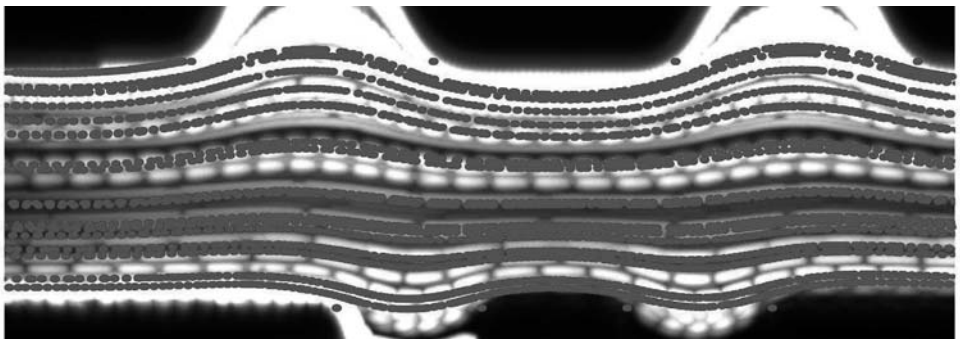

Figure 4.3: A comparison between the COMSOL$^{\text{tm}}$ simulation of the flow lines (red points) and the actual trajectory path of the beads (white points).

a given voltage and does not consider minimizing the ”irregular” flow due to the side channels containing the electrodes. This should also be taken into account for future optimization of the design.

4.3.2 2^{nd} Generation Chip

The geometry in question is shown in figure 4.4. The system consists of one main channel and two access channels for electrodes, each containing an electrode.

In order to determine the electric field or the potential drop in the channel the resistance of the different parts of the system in figure 4.4 needs to be described. If the system between the electrodes is described as a circuit with three resistors (two from the access channels and one from the main channel, see figure 4.4) then the voltage in the channel will be (using Kirchhoff's circuit laws)

$$V = I(R_{ch} + 2R_{ac}), \tag{4.3}$$

where V is the potential applied to the electrodes, I the current, R_{ch} the resistance in the main channel, and R_{ac} the resistance of the access channel. Using Kirchhoff's circuit laws the potential drop V_{eff} in the main channel is given as

$$V_{eff} = IR_{ch}. \tag{4.4}$$

Substituting equation 4.4 into equation 4.3 gives to

$$V = \frac{V_{eff}}{R_{ch}}(R_{ch} + 2R_{ac}) \Leftrightarrow V_{eff} = V\frac{R_{ch}}{R_{ch} + 2R_{ac}}. \tag{4.5}$$

The resistances in the different channels need to be determined in order to calculate the potential in the channel.

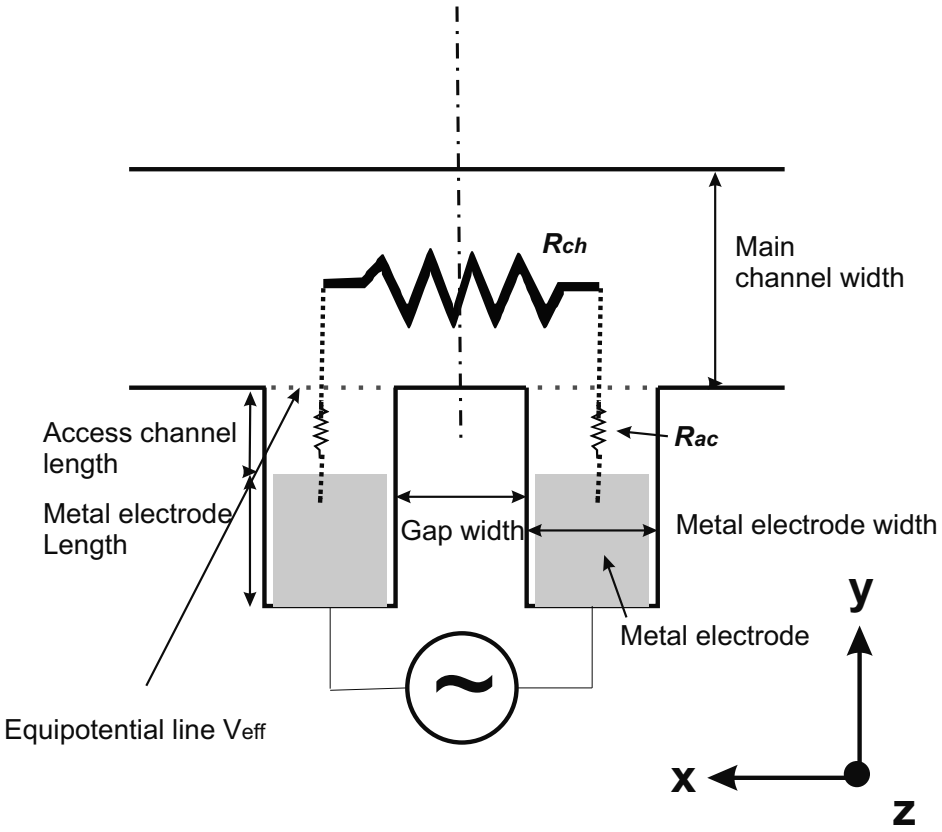

Figure 4.4: Schematic drawing of the second channel geometry used for chromosome manipulation. The height of the channel structure was 30 µm. Where R_{ch} is the resistance in the channel and R_{ac} is the resistance of the access channel. The equipotential line is the border between the main channel and access channels.

The resistance in the main channel, R_{ch}, can be described by the cell constant [16], as

$$R_{ch} = \frac{\kappa_z}{\sigma_m}, \tag{4.6}$$

where κ_z is the cell constant of the system and σ_m is the conductivity of the medium, in this case the liquid in the channel. As the cell constant is invariant in conformal mapping [16], it can be defined using the parallel plate capacitor geometry (see section A and figure A.1 E). The cell constant is given as

$$\kappa_z = \frac{L_s}{A_e},$$

where L_s is the distance between the area of electrodes and A_e is the area of the electrodes. So in the parallel capacitor geometry (w space) the cell constant is given as

$$\kappa_z = \kappa_w = \frac{|w_e|}{|w_d|}\frac{2}{h_s}, \tag{4.7}$$

where w_e is the length of the electrodes, w_d is the distance between the electrodes, h_s (unchanged through the transformation) is the height of the system, and the factor 2 arises from the symmetry argument (see appendix A). As described earlier w_d and w_e can be substituted with the complete elliptic integrals of the first kind $K(k)$ and $K(\sqrt{1-k^2})$. Using equations 4.6 and 4.7 the channel resistance is thus given as

$$R_{ch} = \frac{2}{\sigma_m h_s} \frac{|w_e|}{|w_d|}. \tag{4.8}$$

To estimate the resistance in the access channels the theory described in appendix A for the electric field is used. The geometry can be described in the same way as in appendix A, a channel with an electrode at the bottom. According to work done by N. Demierre *et al.* [16] one cannot just look at the cell constant as was done in the calculation of the channel resistance. Their work shows that the calculation of the resistance of the access channels using the cell constant is off by almost a factor 2. This is caused by the electric field distribution being nonuniform at the interface (equipotential line) between the access channels and the main channel. Figure 4.5 shows a simulation of the size of the electric field along the equipotential line. As can be seen from figure 4.5 the field is far from uniform, which is supported by the work by N. Demierre *et al.* [16].

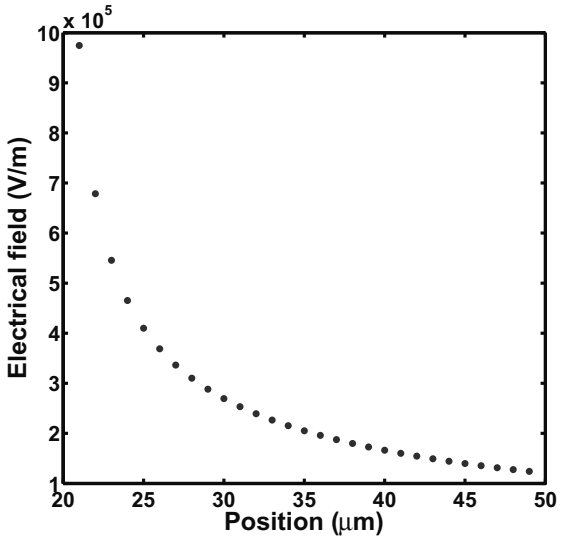

Figure 4.5: MATLAB$^{\mathrm{tm}}$ simulation of the size of the electric field along the equipotential line between the main channel and an access channel (see figure 4.4).

Figure 4.6 shows a simulation of the size of the electric field at the equipotential line in the direction of the system height (z direction) between the main

channel and an access channel. As can be seen the size of the electric field vary much less in this direction.

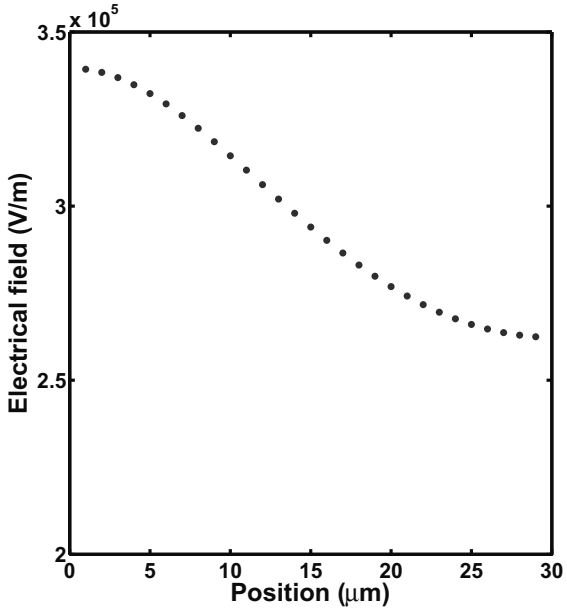

Figure 4.6: MATLAB$^{\mathrm{tm}}$ simulation of the size of the electric field at the equipotential line (see figure 4.4) in the direction of the system height between the main channel and an access channel (z direction).

In order to estimate R_{ac} we start with Ohm's law [45]:

$$R_{ac} = \frac{\Delta V_{ac}}{I} = \frac{\Delta V_{ac}}{h_s \cdot \sigma_m \int E_{ch}(x)dx}, \tag{4.9}$$

where ΔV_{ac} is the average potential drop from the electrode to the boundary, I is the current, and $E_{ch}(x)$ is the electric field along the boundary, obtained from the field in the channel. Here it is assumed that the distribution varies along the boundary in the x direction, but is constant in the z direction. ΔV_{ac} is obtained as a weighted average of the current density or electric field along the boundary [16]

$$\Delta V_{ac} = \frac{\int E_{ac}(x)\Delta V(x)dx}{\int E_{ac}(x)dx}, \tag{4.10}$$

where $\Delta V(x)$ is obtained from the current density along the boundary ($j_{ch} = E_{ch}(x)\sigma_m$) as

$$\Delta V(x) = h_s E_{ch}(x)\sigma_m dx R_{dx}, \tag{4.11}$$

and R_{dx} is given as

$$R_{dx} = \frac{\kappa_{ac}}{\sigma_m dx}. \tag{4.12}$$

κ_{ac} is similar to κ_z above but without the symmetry argument. Combining equations 4.9, 4.10, 4.11, and 4.12 the resistance of the access channel becomes

$$R_{ac} = \frac{\kappa_{ac}}{\sigma_m} \frac{\int E_{ch}^2 dx}{(\int E_{ch} dx)^2}. \tag{4.13}$$

The DEP force in the channel can now be optimized by maximizing V_{eff}.

4.3.3 Experimental Setup

The optical microscope setup used for the DEP deflection measurements was the same and with the same settings as is described in section A.1.3. Figure 4.7 shows a schematic drawing of the experimental setup for the DEP experiments on chromosomes. It consists of a function generator, an amplifier, and the flow system in its holder.

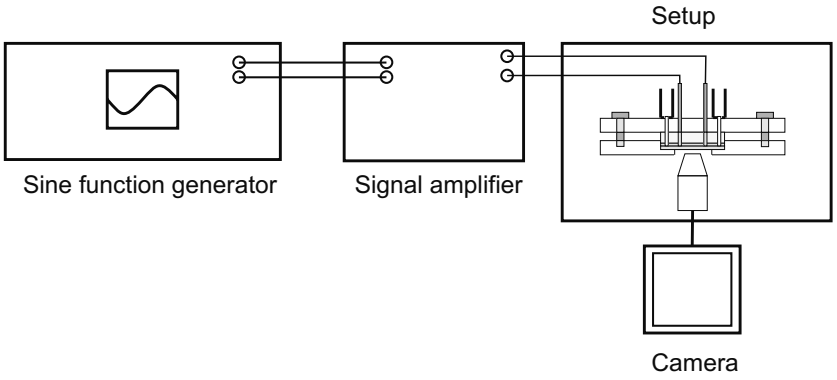

Figure 4.7: Schematic drawing of the experimental setup for the DEP experiments on chromosomes.

For driving the flow through the system a Chemix N300C syringe pump was used, while for generating the electrical signal a Tabor Electronics 50MHz Function Generator 8550 with an ENI RF Power Amplifier model 310L working as signal amplifier was used.

The layout of the flow system is the same as in appendix A.1.3 (the length of the channel, layout of liquid connections and electrode pads). The electrodes should be in the center of the channel as sketched in figure 4.8.

Polyvinylpyrrolidone (PVP) (Sigma: P5288) was mixed with the chromosome solution to obtain a concentration of 0.1% by weight per volume. The chip was then mounted on the microscope and the function generator and signal amplifier were connected to the electrodes. The solution was then injected into the chip by the pump. Chromosomes were then localized in the channel and a potential was applied while the velocity and deflection of the chromosomes were recorded with

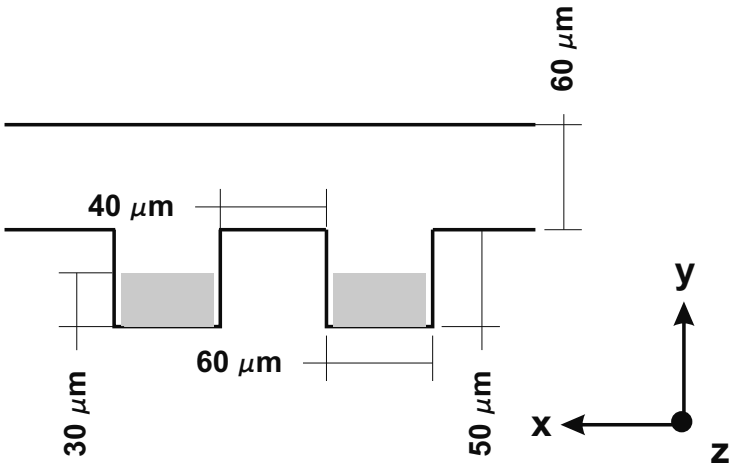

Figure 4.8: Schematic drawing of the final flow system design for manipulating chromosomes. The grey areas represent the electrodes. The height of the channel structure was 30 μm (see appendix B and B.3).

the CCD camera. The images were analyzed with ImageJ in order to obtain the velocity and the deflection. The frequency was swept between 500 kHz and 25 MHz, in steps of 500 kHz, while the applied amplitude of the sinusoidal signal was 20 V or 30 V peak to peak. The chip along with dimensions is shown in figure 4.8. The channel is 60 μm wide and 10 mm long with a height of 30 μm. The access channels are 60 μm wide and 50 μm long with a pitch of 40 μm. The experiments were made with two chromosome solutions, with conductivities of 0.12 S/m and 0.06 S/m. These were measured by a calibrated conductivity meter (CDM210 Radiometer).

A COMSOL$^{\mathrm{tm}}$ simulation was made in order to estimate the gradient of the electrical field squared $\nabla|E|^2$. This is shown in figure 4.9 in the xy plane in the middle of the channel, where most chromosomes are expected to be found due to the parabolic flow profile. The dielectrophoretic force on the chromosomes will moreover depend on the chromosome dimensions and dielectric properties, their orientation and the frequency of the applied sinusoidal signal.

Further, a comparison between the COMSOL$^{\mathrm{tm}}$ and MATLAB$^{\mathrm{tm}}$ simulations of the gradient of the electrical field squared was made along a line in the middle of the channel in the y direction shown in figure 4.10. This showed that the analytical method gives very precise results as the difference between the MATLAB$^{\mathrm{tm}}$ (analytical) and the COMSOL$^{\mathrm{tm}}$ (numerical) simulations is very small.

For the theoretical calculations of the chromosomes, the average dimensions for length, width and thickness (as measured by AFM) were used. Based on measurements on 15 chromosomes the length was found to be $l = 2.83$ μm, the width $w = 2.17$ μm and the thickness $h = 500$ nm. Equations 1.8 and 1.7 were used

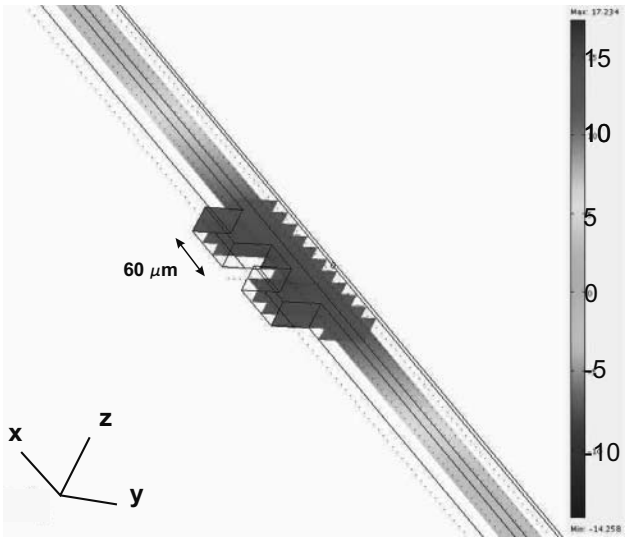

Figure 4.9: COMSOL$^{\mathrm{tm}}$ simulation of the logarithm of the gradient of the electrical field squared in the area of the electrodes.

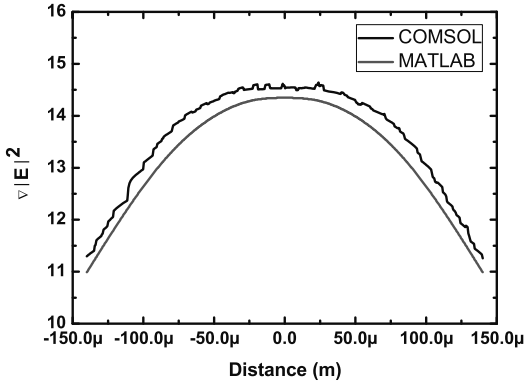

Figure 4.10: Simulation of the gradient of the electrical field squared in the middle of the system made with both COMSOL$^{\mathrm{tm}}$ and MATLAB$^{\mathrm{tm}}$.

to determine the depolarization factors and the Claussius-Mossoti factor (CMF) respectively for each of the axes of the ellipsoid and the preferred orientation at each frequency was calculated by finding the sign of the torque and using table 5.1 in [44].

The torque along any of the three axes is given by [44]

$$\langle T \rangle_1 = \frac{2}{3}\pi \cdot l_1 l_2 l_3 \epsilon_m \epsilon_0 (L_3 - L_2) E_{0,2} E_{0,3} \mathrm{Re}\{f_{cm,2} f_{cm,3}\}, \tag{4.14}$$

where $E_{0,i}$ is the electric field along the i axis and $f_{cm,i}$ is the CMF along the i axis as calculated by equation 1.7. Which means that the sign of the torque is determined by the sign of the factor $(L_3 - L_2)\mathrm{Re}\{f_{cm,2}f_{cm,3}\}$, where L_i are the depolarization factors along the i axis as calculated by equation 1.8 and a convention for a right-handed coordinate system, i.e. 1→2→3→1.

For the movement of the chromosomes under the influence of a DEP force, a friction factor for movement parallel to each of the three orientation axes was calculated. It was assumed that alignment to the relevant axis of the ellipsoid happens faster than the translational movement. The friction coefficient f_i was calculated as [108]

$$f_i = \frac{16\pi\eta}{A + l_i^2 A_i}, \tag{4.15}$$

where η is the viscosity of the solution and l_i are each of the semiaxes for the ellipsoid, i.e. $l/2$, $w/2$, and $h/2$. A and A_i are given by the elliptic integrals

$$A = \int_0^\infty \frac{ds}{\sqrt{(s + l_1^2)(s + l_2^2)(s + l_3^2)}} \tag{4.16}$$

and

$$A_i = \int_0^\infty \frac{ds}{(s + l_i^2)\sqrt{(s + l_1^2)(s + l_2^2)(s + l_3^2)}}. \tag{4.17}$$

s is the integral variable. The elliptic integrals were calculated using Maple$^{\mathrm{tm}}$.

4.3.4 Results

For the experiments with a chromosome solution with a conductivity of 0.06 S/m a voltage of 30 V peak to peak was used, while for the experiments with a chromosome solution with a conductivity of 0.12 S/m a voltage of 20 V peak to peak was used.

First, simple tests were made to see if the system could move chromosomes at all due to the applied voltage by turning the electrical field on and off sequentially. Figure 4.11 A shows chromosomes pass by the electrodes when no field is applied between them. Figure 4.11 B shows chromosomes passing the electrodes after a signal of 1 MHz with an amplitude of 15 V is applied to the electrodes. From this figure, as well as several other data sets taken but not shown here, it was concluded that there was a force on the chromosomes when the field was on. That force can be attributed to DEP.

As it was now established that the applied voltage affected the trajectories of the chromosomes compared to trajectories taken without an applied voltage, the experiments continued by investigating the frequency dependency of the resulting trajectory.

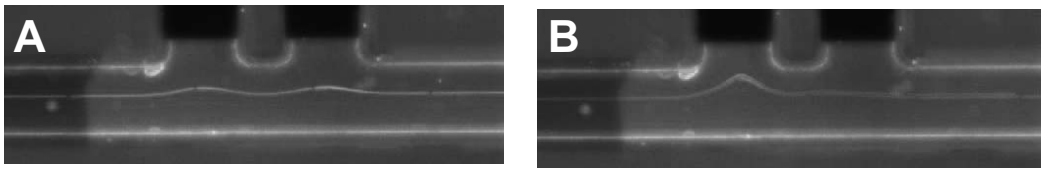

Figure 4.11: Stacks of images of chromosomes passing the electrodes in a liquid with a conductivity of 0.6 S/m, A) stack of 5 images of chromosomes passing the electrodes with no field applied. B) stack of 5 images with where a field of 1 MHz with an amplitude of 15 V later.

Figure 4.12 shows images of 3 experiments done at 100 kHz, 1 MHz and 3 MHz. The flow in these experiments was from left to right, as is shown by the arrow in the figure. The superimposed curves (with a dot as symbol) show the simulated trajectory path of chromosomes assuming no DEP force is acting on them. These trajectories were taken at different heights in the channel, i.e. at a height of 5 μm and a height of 15 μm. As the channel is 30 μm in height (z direction), these two trajectories correspond to a low and a high liquid velocity. This is due to the parabolic profile of the flow velocity [48]. When no field is present, these trajectories are the same in the xy plane, therefore only one of them is shown.

By comparing the theoretical no field trajectories to those recorded by the camera it is relatively easy to see that positive DEP occurs at all tested frequencies. The degree to which a certain trajectory is affected by the field depends on the initial position of the chromosome inside the channel. the closest to the middle the chromosome is (both in terms of channel width and in terms of channel height) the less it is affected by the DEP force. This is one of the reasons that chromosomes seemingly starting from the same xy position are affected differently by the DEP force.

Experiments were done at higher frequencies, too, with positive DEP observed up to 25 MHz, however, due to limitations of the used frequency generator, data taken at frequencies over 10 MHz are not reliable and are therefore not shown.

When the solution with a conductivity of 0.12 S/m was used, the results were strikingly different, as can be seen in figure 4.13. The figure shows 4 experiments taken at 1, 6, 7 and 10 MHz. The superimposed lines are again theoretically calculated.

Figure 4.13 shows that for frequencies below 7 MHz no difference can be observed between the recorded trajectories and the theoretically calculated non-field trajectories, whereas negative DEP occurs at frequencies from 7 MHz and above. This can be interpreted as two things: 1) Positive or negative DEP occur below 7 MHz, but the movement of the chromosomes due to the DEP force is too small (due to a small Claussius Mossoti factor) to be noticed 2) There is no DEP force

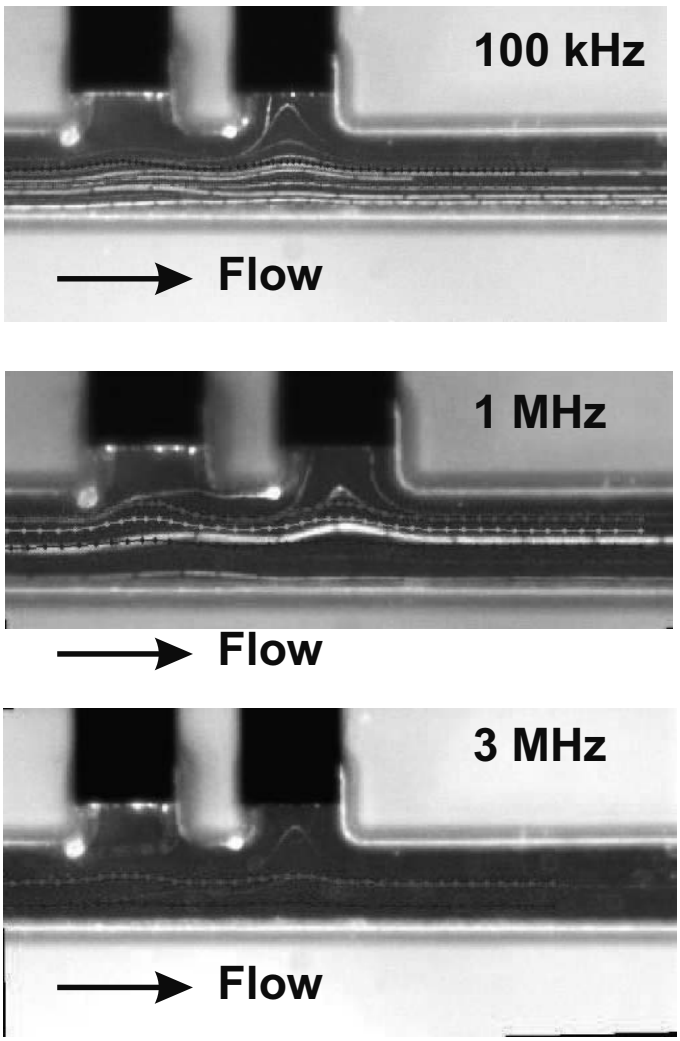

Figure 4.12: Stacked images of the trajectories of chromosomes at 3 different frequencies for a solution with a conductivity of 0.06 S/m. The theoretically calculated trajectories for non-field conditions are superimposed to guide the eye.

on the chromosomes at all at frequencies under 7 MHz.

Based on these results, an investigation was done in order to estimate the dielectric properties of the chromosomes in solution. By looking at equation 1.7 one can summarize the conditions for positive and negative DEP as a function of the dielectric properties as in table 4.1.

Using table 4.1 and considering the results summarized in figures 4.12 and 4.13 we can conclude the following:

1. $\sigma_p > 0.06$ S/m, as only +ve DEP was observed for a solution with a conductivity of 0.06 S/m

	$\epsilon_p < \epsilon_m$	$\epsilon_p > \epsilon_m$
$\sigma_p < \sigma_m$	-ve DEP all frequencies	-ve DEP at low frequencies +ve DEP at high frequencies
$\sigma_p > \sigma_m$	+ve DEP at low frequencies -ve DEP at high frequencies	+ve DEP all frequencies

Table 4.1: DEP behavior of a homogeneous sphere for the various combinations of particle and dielectric properties of the solution.

2. $\epsilon_p < \epsilon_m$ as only -ve DEP was observed for a solution with a conductivity of 0.12 S/m

As the buffer is greatly diluted with distilled water, the relative permittivity of the buffer is going to be set equal to that of water, i.e. 78.4. Moreover, the relative permittivity of the chromosomes in dry condition was measured by AFM to be 8.4 (see section 3.2.4). This is expected to be larger for chromosomes in liquid, which means that the relative permittivity of the chromosomes in liquid should be in the range of $8.4 < \epsilon_p < 78.4$.

To further narrow down the range for the conductivity and permittivity of the chromosomes theoretical calculations of the chromosome's Claussius Mossoti factor (CMF) and trajectory were done for permittivities in the above range and conductivities from 0.06 S/m up to 10 S/m at the frequency of 1 MHz and a buffer conductivity of 0.12 S/m. The first observation was that in the range of the investigated permittivities, no difference in the CMF for the investigated conductivities was observed. Therefore, a permittivity of 40 was used for further calculations. Furthermore, if the conductivity of the chromosomes was above 0.31 S/m, the CMF was large enough to alter the trajectory of the chromosome substantially from the non-field situation. As this was not observed experimentally, it was concluded that the conductivity of the chromosomes must be in the range of $0.06 < \sigma_p < 0.31$ S/m.

To confirm that the simulation program gives correct trajectories a video of the movement of chromosomes without a field present was also taken and the program was used in order to calculate the trajectories. The result, shown in figure 4.14, confirms that the calculation reproduces the recorded trajectories well.

4.4 Summary

We have here presented a preliminary study of the electrical properties of human chromosomes using DEP. A DEP flow system based on the design by N. Demierre *et al.* [16] was used in the experiments. Comparison between the MATLAB$^{\mathrm{tm}}$ (analytical) and the COMSOL$^{\mathrm{tm}}$ (numerical) showed very little difference. From the experiments combined with an appropriate theoretical representation of a chromosome we estimated the conductivity to be in the range of $0.060 < \sigma_p < 0.310$ S/m. Finally, it has been shown that it is possible to manipulate human chromosomes in a micro-fluidic system by DEP, which opens up the very exciting possibility of chromosome trapping and sorting by this method.

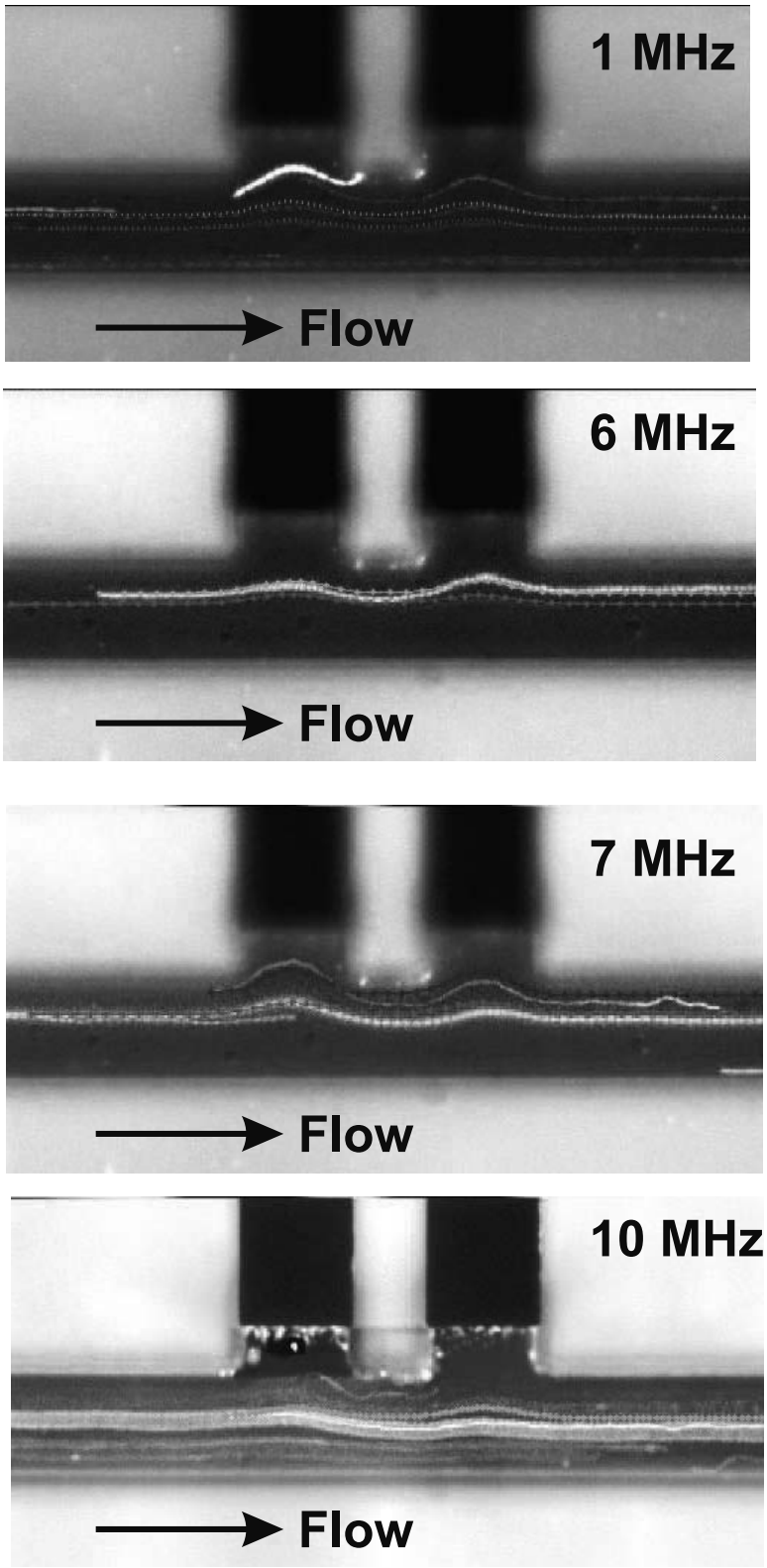

Figure 4.13: Stacked images of the trajectories of chromosomes at 4 different frequencies with a solution with a conductivity of 0.12 S/m. The theoretically calculated trajectories for non-field conditions are superimposed to guide the eye. While for 1 and 6 MHz no observable difference between the non-field and the DEP affected trajectories can be seen, the 7 and 10 MHz images show some tendencies towards a negative DEP.

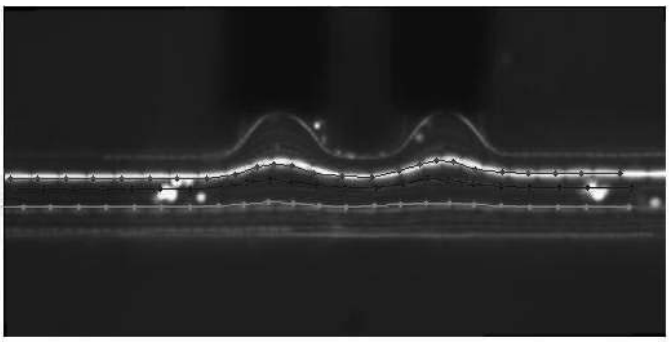

Figure 4.14: Image of chromosomes moving under no electrical field. Superimposed are the calculated theoretical trajectories under the same conditions.

Chapter 5

Conclusion and Outlook

5.1 Conclusion

The primary objective of this project was to find a suitable method for sorting human chromosomes and investigate dipeptide superstructures. Based on a literature investigation, the method chosen was dielectrophoresis. In order to investigate the potential of using DEP to sort human chromosomes, it was necessary to map some physical parameter like permittivity and conductivity of the chromosomes.

It was demonstrated that the EFM-phase could indeed be used to investigate the dielectric properties of chromosomes as well as other solid biological samples. For these measurements a simple method for the determination of the needed cantilever properties for quantitative analysis was developed. Using the EFM-phase method an estimate of the dielectric constant of the fixed chromosomes was found to be around 8.4 with an average uncertainty of ± 1.4.

The EFM-phase method was also applied to different dipeptide superstructures, to distinguish between three different types of structures (hollow and silver-filled peptides, and silver wires) fabricated using peptides. The method was further able to map the cavity of the peptide tubes down to around 50-60 nm (limited by the cantilever tip). The EFM-phase method did not yield any dielectric constant of the dipeptide structures which was due to their complex superstructures. However, this method seems to be a promising tool for the characterization of self-assembled peptides for use in microdevices.

A preliminary study of the electrical properties of human chromosomes using DEP was also conducted. A DEP flow system based on the design by N. Demierre *et al.* [16] was fabricated. As this DEP system is a closed system, liquid drying during experiments can be avoided, making the experiments more reliable and

controllable. The experiments together with theoretical simulations estimated the conductivity of polyamine buffer chromosomes in the range of $0.060 < \sigma_p < 0.31$ S/m. Finally, it was shown that it is possible to manipulate human chromosomes in a micro-fluidic system by DEP.

5.2 Outlook

This project has shown that a combination of SPM techniques and DEP can be used to characterize certain biological samples. This method can also be applied to other types of samples, biological or not, whose dielectric properties are unknown. For this purpose a new DEP experimental chip should be fabricated using the simulations of section 4.3.2 to maximize the DEP force on the particles. This chip should be used on pre-sorted human chromosomes in order to check if the dielectric properties of chromosomes are an universal material constant or if they change from chromosome to chromosome. Finally, it will be interesting to fabricate a chip that can sort chromosomes according to size (which is also a type sorting).

The EFM-phase method shows interesting applications in characterizing samples (polymer blends, bio-composites, nano-particle mixtures, etc.) with a minimum size of a few hundred nanometers with a material variation. As composite materials (e.g. carbon nanotubes embedded in polymer matric) are a fast growing research field, the EFM-phase method ability to distinguish between different layers could be a valuable tool for understanding the performance of these materials (T. S. Jespersen *et al.* [1]). Other SPM techniques can be applied to biological and other samples for mapping different properties, e.g. force distance curves for investigating their mechanical properties, conducting AFM for mapping the conductivity.

Bibliography

[1] T. S. Jespersen and J. Nygård. Mapping of individual carbon nanotubes in polymer/nanotube composites using electrostatic force microscopy. *Applied Physics Letters*, 90:183108–1–3, 2007.

[2] G. Koley and M. G. Spencer. Cantilever effects on the measurement of eletrostatic potentials by scanning kelvin probe microscopy. *Applied Physics Letters*, 79(4):545–547, 2001.

[3] R. Krupke, F. Hennrich, and M. M. Kappes H. v. Löhneysen. Separation of metallic from semiconducting single-walled carbon nanotubes. *Science*, 301:344–347, 2003.

[4] C. Prinz, J. O. Tegenfeldt, R. H. Austin, E. C: Cox, and J. C. Sturm. Bacterial chromosome extraction and isolation. *Lab on a chip*, 2:207–212, 2002.

[5] B. G. Hawkins, Y. A. Syed A. E. Smith, and B. J. Kirby. Continuous-flow particle separation by 3d insulative dielectrophoresis using coherently shaped, dc-biased, ac electric fields. *Analytical Chemisty*, 79 (19):7291–7300, 2007.

[6] S. Banerjee, B. White, L. Huang, B. J. Rego, S. O'Brien, and I. P. Herman. Precise postitioning of carbon nanotubes by ac dielectrophoresis using floating posts. *Applied Physics A*, 86:415–419, 2007.

[7] S. Kapishnikov, V. Kantsler, and V. Steinberg. Continuous particle size separation and size sorting using ultrasound in a microchannel. *Journal of Statistical Mechanics: Theory and Experiment*, 2006.

[8] A. Nilsson, F. Petersson, H. Jönsson, and T. Laurell. Acoustic control of suspended particles in micro fluidic chips. *Lab on a Chip*, 4:131–135, 2004.

[9] F. Petersson, C. Holm A. Nilsson, H. Jönsson, and T. Laurell. Continuous separation of lipid particles from erythrocytes by means of laminar flow and acoustic standing wave forces. *Lab on a Chip*, 5:20–22, 2005.

[10] M. Evander, L. Johansson, T. Lilliehorn, M. Lindvall J. Piskur, S. Johansson, M. Almqvist, T. Laurell, and J. Nilsson. Noninvasive acoustic cell trapping in a microfluidic perfusion system for online bioassays. *Analytical Chemistry*, 79:2984–2991, 2007.

[11] J. A. Davis, D. W. Inglis, K. J. Morton, D. A. Lawrence, L. R. Huang, S. Y. Chou, J. C. Sturm, and R. H. Austin. Deterministic hydrodynamics: Taking blood apart. *Proceedings of the National Academy of Sciences*, 103 (40):14779–14784, 2006.

[12] http://cmgm.stanford.edu/biochem/biochem201/.

[13] M. Reches and E. Gazit. Casting metal nanowires within discrete self-assembled peptide nanotubes. *Science*, 300:625–627, 2003.

[14] Veeco, Veeco Metrology 112 Robin Hill Road, Santa Barbara CA 93117. *CP-II User's guide Part II: Advanced techniques*, 2004.

[15] http://www.imagemet.com/.

[16] N. Demierre, T. Braschler, P. Linderholm, U. Seger, H. v. Lintel, and P. Renaud. Characterization and optimation of liquid electrodes for lateral dielectrophoresis. *Lab on a Chip*, 7:355–365, 2007.

[17] J. H. Scofield. Frequency-domain description of a lock-in amplifier. *American Journal of Physics*, 62 (2):129–133, 1994.

[18] J.C. Murray S.M. Moghimi and, A.C. Hunter and. Long-circulating and target specific nanoparticles: theory to practice,. *Pharmacol. Reviews*, 53:Long–circulating, 2001.

[19] E. Gazit. *The formation of aromatic dipeptide nanotubes (ADNT). In Plenty of room for biology at the bottom. An introduction to bionanotechnology*. Imperial College Pres, London, 2007.

[20] M. Yemini, M. Reches, J. Rishpon, and E. Gazit. Novel electrochemical biosensing platform using self-assembled peptide nanotubes. *Nano Letters*, 5(1):183–186, 2005.

[21] S. Zhang, D. M. Marini, W. Hwang, and S. Santoso. Design of nanostructured biological materials through self-assembly of peptides and proteins. *chemical Biology*, 6:865–871, 2002.

[22] L. Adler-Abramovich and E. Gazit. Controlled patterning of peptide nanotubes and nanospheres using inkjet printing technology. *Journal of Peptide Science*, 14:217–223, 2008.

[23] M. Reches and E. Gazit. Biological and chemical decoration of peptide nanostructures via biotin-avidin interactions. *Journal of Nanoscience and Nanotechnology*, 7:2239–2245, 2007.

[24] J. Lewis and M. Raff and K. Roberts and J. D. Watson B. Alberts and, D. Bray and. *The Cell*. Garland publishing inc., 1994.

[25] B. Bhushan, editor. *Handbook of Nanotechnology*. Springer, first edition, 2004.

[26] F. Kremer and A. Schönhals. *Broadband Dielectric Spectroscopy*. Springer, 2003.

[27] T. Strachan and A. P. Read. *Human Molecular Genetics*. Garland Science, 3 edition, 2004.

[28] J. R. Macdonald. Impedance spectroscopy. *Annals of Biomedical Engineering*, 20:289–305, 1992.

[29] F. Fang and Y. F. Zhang. Dc electrical conductivity of au nanoparticle/chloroform and toluene suspensions. *JOURNAL OF MATERIALS SCIENCE*, 40:2979–2980, 2005.

[30] D. Holmes, D. Pettigrew, C. H. Reccius, J. D. Gwyer, C. v. Berkel, J. Hollow, D. E. Davies, and H. Morgan. Leukocyte analysis and differentiation using high speed microfluidic single cell impedance cytometry. *Lab on a Chip*, 9:2881–2889, 2009.

[31] Peter Goodhew, John Mumphreys, and Richard Beanland. *Electron Microscopy and Analysis*. Taylor & Francis, third edition, 2001.

[32] *Scanning Probe Microscopy and Spectroscopy - Methods and Applications*. Cambridge University Press, 1984. Book on the theory of SPM microscopy including AFM/SFM.

[33] H.-J. Butt, B. Cappella, and M. Kappl. Force measurements with the atomic force microscope: Technique, interpretation and applications. *Suface Science Reports*, 59:1–152, 2005.

[34] M. D. Croitoru, G. Bertsche, D. P. Kern, C. Burkhardt, S. Bauerdick, S. Sahakalkan, and S. Roth. Visualization and in situ contacting of carbon nanotubes in a scanning electron microscope. *The Journal of Vacuum Science Technology B*, 23 (6):521–531, 2005.

[35] C. Roduit, S. Sekatski, G. Dietler, S. Catsicas, F. Lafont, and S. Kasas. Stiffness tomography by atomic force microscopy. *Biophysical Journal*, 97:674–677, 2009.

[36] http://www.veeco.com/pdfs/appnotes/.

[37] M. Nonnenmacher, M. P. O'Boyle, and H. K. Wickramasinghe. Kelvin probe force microscopy. *Physical Review Letters*, 58(25):2921–2923, 1991.

[38] M. Bockrath, N. Markovic, A. Shepard, M. Tinkham, L. Gurevich, L. P. Kouwenhoven, M. W. Wu, and L. L. Sohn. Scanned conductance microscopy of cabon nanotubes and λ-dna. *Nano Letters*, 2(3):187–190, 2002.

[39] T. S. Jespersen and J. Nygård. Charge trapping in carbon nanotube loops demonstrated by electrostatic force microscopy. *Nano Letters*, 5(9):1838–1841, 2005.

[40] E. Mikamo-Satoh, F. Yamada, A. Takagi, T. Matsumoto, and T. Kawai. Electrostatic force microscopy: imaging dna and protein polarizations one by one. *Nanotechnology*, 20:145102, 2009.

[41] C. Staii, A. T. Johnson Jr., and N. J. Pinto. Quantitive analysis of scanning conductance microscopy. *Nano Letters*, 4(5):859–862, 2004.

[42] J. Colchero, A. Gil, and A. M. Baró. Resolution enhancement and improved data interpretation in electrostatic force microscopy. *Physical Review B*, 64:245403(1–11), 2001.

[43] Hywel Morgan and Nicolas G. Green. *AC Electrokinetics: colloids and naoparticles*. Research Studies Press LTD., 1 edition, 2003.

[44] T. B. Jones. *Electromechanics of Particles*. Cambridge University Press, 1995.

[45] David J. Griffiths. *Introduction to Electrodynamics*. Prentice Hall, 3 edition, 1999.

[46] H. Morgan and N. G. Green. Dielectrophoresis manipulation of rod-shaped viral particles. *Journal of Electrostatics*, 42:279–293, 1997.

[47] M. Dimaki and P. Bøggild. Dielectrophoresis of carbon nanotubes using microelectrodes: a numerical study. *Nanotechnology*, 15:1095–1102, 2004.

[48] Henrik Bruus. *Theoretical Microfluidics*. Oxford University Press, 1 edition, 2008.

[49] Y. Seger-Sauli, M. Panayiotou, S. Schnydrig, M. Jordan, and P. Renaud. Temperature measurements in microfluidic systems: Heat dissipation of negative dielectrophoresis barriers. *Electrophoresis*, 26:2239–2246, 2005.

[50] Z. Wang, O. Hansen, P. K. Petersen, A. Rogeberg, J. P. Kutter, D. D. Bang, and A. Wolff. Dielectrophoresis microsystem with integrated flow cytometers for on-line monitoring of sorting efficiency. *Electrophoresis*, 27 (24):5081–5092, 2006.

[51] U. Seger, S. Gawad, R. Johann, A. Bertsch, and P. Renaud. Cell immersion and cell dipping in microfluidic devices. *Lab on a Chip*, 4:148–151, 2003.

[52] T. Müller, G. Gradl, S. Howitz, S. Shirley, Th. Schnelle, and G. Fuhr. A 3-d microelectrode system for handling and caging single cells and particles. *Biosensors and Bioelectronics*, 14:247–256, 1999.

[53] D. C. Duffy, J. C. McDonald, O. J. A. Schueller, and G. M. Whitesides. Rapid prototyping of microfluidic systems in poly(dimethylsiloxane). *Analytical Chemisty*, 70 (23):4974–4984, 1998.

[54] S. Golan, D. Elata, and U. Dinnar. Hybrid dielectrophoresis devices that employ electrically floating electrodes. *Sensors and Actuators A*, 142:138–146, 2008.

[55] K. Yasuda, S.-I. Umemura, and K. Takeda. concentration and fractionation of small particles in liquid by ultrasound. *Japanese Journal of Applied Physics*, 34:2715–2720, 1995.

[56] G. Whitworth and W. T. Coakley. Particle column formation in a stationary ultrasonic field. *Journal of Acoustical Society of America*, 91 (1):79–85, 1992.

[57] T. Laurell, P. Petersson, and A. Nilsson. Chip integrated strategies for acoustic separation and manipulation of cells and particles. *Chemical Society Reviews*, 36:492–506, 2006.

[58] U. Simu T. Lilliehorn, M. Nilsson, M. Almqvist, T. Stepinski, T. Laurell, and S. Johansson J. Nilsson. Trapping of microparticles in the near field of an ultrasonic transducer. *Ultrasonics*, 43:293–303, 2005.

[59] L. R. Huang, E. C. Cox, R. H. Austin, and J. C. Sturm. Continuous particle separation through deterministic lateral displacement. *Science*, 304:987–990, 2004.

[60] D. W. Inglis, J. A. Davis, R. H. Austin, and J. C. Sturm. Critical particle size for fractionation by deterministic lateral displacement. *Lab on a Chip*, 6:655–658, 2006.

[61] Y. Li, C. Dalton, H. J. Crabtree, G. Nilsson, and K. V. I. S. Kaler. Continuous dielectrophoretic cell separation microfluidic device. *Lab on a Chip*, 7:239–248, 2007.

[62] C. E. Ford, K. W. Jones, P. E. Polani, J. C. Dealmeida, and J. H. Briggs. A sex-chromosome anomaly in a case of gonadal dysgenesis (turners syndrome). *Lancet*, 1(APR4):711–713, 1959.

[63] P. C. Nowell and D. A. Hungerford. Minute chromosome in human chronic granulocytic leukemia. *Science*, 132(3438):1497, 1960.

[64] R. R. Sinden. *DNA Structure and Function*. Academic Press, 1994.

[65] A. T. Summers. *Chromosomes: Organization and Function*. Blackwell Publishing, 2001.

[66] J. Tamayo and M. Miles. Human chromosome structure studied by scanning force microscopy after an enzymatic digestion of the covering cell material. *Ultramicroscopy*, 82:245–251, 2000.

[67] C. A. Janeway Jr., P. Travers, M. Walport, and M. J. Shlomchik. *Immunobiology*. Garland Publishing, 2001.

[68] A. Miller and J. Tanner. *Essentials of Chemical Biology: structure and dynamics of biological macromolecules*. Wiley, 2008.

[69] S. Scanlon and A. Aggeli. Self-assembling peptide nanotubes. *Nano Today*, 3 (3-4):22–30, 2008.

[70] L. Adler-Abramovich, M. Reches, V. L. Sedman, S. Allen, S. J. B. Tendler, and E. Gazit. Thermal and chemical stability of diphenylalanine peptide nanotubes: Implications for nanotechnological applications. *Langmuir*, 22:1313–1320, 2006.

[71] J. D. Hartgerink, E. Beniash, and S. I. Stupp. Peptide-amphiphile nanofibers: A versatile scaffold for the preparation of self-assembling materials. *Proceedings of the National Academy of Sciences*, 99 (8):5133–5138, 2002.

[72] G. Dresselhaus M.S. Dresselhaus and Ph. Avouris, editors. *Carbon Nanotubes*. Springer, 2000.

[73] M. Xue, S. Guo, X. S. Zhao, and T. Cao. Fabrication of ultrafine protein arrays on easy-fabricated metallic nanostructures. *Scripta Materialia*, 58:554–557, 2008.

[74] Y. J. Oh, W. Jo, S. Kim, S. Park, and Y. S. Kim. Nanoscale observation of local bound charges of patterned protein arrays by scanning force microscopy. *Nanotechnology*, 19:365302, 2008.

[75] K. Wadu-Mesthrige, N. A. Amro, J. C. Garno, S. Xu, and G. Liu. Fabrication of nanometer-sized protein patterns using atomic force microscopy and selective immobilization. *Biophysical Journal*, 80:1891–1899, 2001.

[76] J. R. Kenseth, J. A. Harnisch, V. W. Jones, and M. D. Porter. Investigation of approaches for the fabrication of protein patterns by scanning probe lithography. *Langmuir*, 17:4104–4112, 2001.

[77] P. Roca-Cusachs, I. Almendros, R. Sunyer, N. Gavara, R. Farré, and D. Navajas. Rheology of passive and adhesion-activated neutrophils probed by atomic force microscopy. *Biophysical Journal*, 91:3508–3518, 2006.

[78] S. M. Hues, C. F. Draper, K. P. Lee, and R. J. Colton. Effect of pzt and pmn actuator hysteresis and creep on nanoindentation measurements using force microscopy. *Review of Scientific Instruments*, 65(5):1561–1565, 1994.

[79] B. G. Lipták. *Instrument Engineers' Handbook Process Control*. CRC Press LLC, 1999.

[80] I. Chorkendoff and J. W. Niemantsverdriet. *Concepts of Modern Catalysis and Kinetics*. Wiley-VCH Verlag GmbH & Co., 2003. Book on surface science by I. Chorkendoff and J. W. Niemantsverdriet.

[81] Stephen R. Elliott. *The Physics and Chemistry of Solids*. Wiley, 2000.

[82] Y. Sugimoto, P. Pou, M. Abe, P. Jelinek, R. Pérez, S. Morita, and O. Custance. Chemical identification of individual surface atoms by atomic force microscopy. *Nature*, 446:65–67, 2007.

[83] http://www.budgetsensors.com/.

[84] http://stm2.nrl.navy.mil/how-afm/how-afm.html. Website on theory of AFM.

[85] Y. Zhou, M. Freitag, J. Hone, C. Staii, N. J. Pinto, and A. G. MacDiarmid. Fabrication and electrical characterization of polyaniline-based nanofibers with diameter below 30 nm. *Applied Physics Letters*, 83(18):8800–8803, 2003.

[86] H. O. Jacobs, H. F. Knapp, S. Müller, and A. Stemmer. Surface potential mapping: A qualitative material contrast in spm. *Ultramicroscopy*, 69:39–49, 1997.

[87] A. Bachtold, M. S. Fuhrer, S. Plyasunov, M. Forero, E. H. Anderson, A. Zettl, and P. L. McEuen. Scanned probe microscopy of electronic transport in carbon nanotubes. *Physical Review Letters*, 84(26):6082–6085, 2000.

[88] V. Palermo, M. Palma, and P. Samorì. Electronic characterization of organic thin films by kelvin probe force microscopy. *Advanced Materials*, 18:145–164, 2006.

[89] S. Kitamura and M. Iwatsuki. High-resolution imaging of contact potential difference with ultrahigh vacuum noncontact atomic force microscope. *Applied Physics Letters*, 72 (24):3154–3156, 2002.

[90] L. S. Cram, C. S. Bell, and J. J. Fawcett. Chromosome sorting and genomics. *Methods in Cell Science*, 24:27–35, 2002.

[91] C. H. Clausen, J. Jensen, J. Castillo, M. Dimaki, and W. E. Svendsen. Qualitative mapping of structurally different dipeptide nanotubes. *Nano Letters*, 8(11):4066–4069, 2008.

[92] C. H. Clausen, J. M. Lange, L. B. Jensen, P. J. Shah, M. I. Dimaki, and W. E. Svendsen. Scanning conductance microscopy investigations on fixed human chromosomes. *Biotechniques*, 44(2):225–228, 2008.

[93] J. Tamayo. Structure of human chromosomes studied by atomic force microscopy part ii. relationship between structure and cytogenetic bands. *Journal of Structural Biology*, 141:189–197, 2003.

[94] M. H. P. Moers, W. H. J. Kalle, A. G. T. Ruiter, J. C. A. G. Wiegant, A. K. Raap, J. Greve, B. G. De Grooth, and N. F. Van Hulst. Fluorescence *in situ* hybridization on human metaphase chromosomes detected by near-field scanning optical microscopy. *Journal of Microscopy*, 182:40–45, 1996.

[95] K. Nomura, O. Hoshi, D. Fukushi, T. Ushiki, and K. Kawabata H. Haga. Visualization of elasticity distribution of single human chromosomes by scanning probe microscopy. *Japanese Journal of Applied Physics*, 44 (7B):5421–5424, 2005.

[96] T. Inoue, K. Takahashi, and H. Yokoyama. Integrated microfluidics for chromosome engineering - preparation, transportation and manipulation. *Archives of Histology and Cytology*, 65(5):465–471, 2002.

[97] W. Wray and E. Stubblefield. A new method for the rapid isolation of chromosomes, mitotic apparatus, or nuclei from mammalian fibroblasts at near neutral ph. *Experimental Cell Research*, 59:469–478, 1970.

[98] J. Tamayo. Structure of human chromosomes studied by atomic force microscopy. *Journal of Structural Biology*, 141:198–207, 2003.

[99] O. Hoshi and T. Ushiki. Three-dimensional structure of g-banded human metaphase chromosomes observed by atomic force microscopy. *Archives of Histology and Cytology*, 64 (5):475–482, 2001.

[100] A. Torii, M. Sasaki, K. Hane, and S. Okuma. A method for determining the spring contant of cantilevers ofr atomic force microscopy. *Measurement Science and Technology*, 7:179–184, 1996.

[101] W. Fritzsche. Salt-dependent chromosome viscoelasticity characterized by scanning force microscopy-based volume measurements. *Microscopy Research and Technique*, 44:357–362, 1999.

[102] L. O. Tjernberg, J. Naslund, F. Lindqvist, J. Johansson, A. R. Karlstrom, J. Thyberg, L. Terenius, and C. Nordstedt. Arrest of β-amyloid fibril formation by a pentapeptide ligand. *Journal Biological Chemistry*, 271(15):8545–8548, 1996.

[103] Y. Song, S. R. Challa, C. J. Medforth, R. K. Watt Y. Qiu, J. E. Miller D. Pena, F. van Swol, and J. A. Shelnutt. Synthesis of peptide-nanotube platium-nanoparticle composites. *Chemical Communications*, pages 1044–1045, 2004.

[104] M. Reches and E. Gazit. Molecular self-assembly of peptide nanostructures: Mechanism of association and potential uses. *Current Nanoscience*, 2:105–111, 2006.

[105] G. Löffler, H. Schreiber, and O. Steinhauser. Calculation of the dielectric properties of a protein and its solvent: Theory and a case study. *Journal of Molecular Biology*, 270:520–534, 1997.

[106] H. Morgan, M. P. Hughes, and N. G. Green. Separation of submicron bioparticles by dielectrophoresis. *Biophysical Journal*, 77:516–525, 1999.

[107] R. Tornay, T. Braschler, N. Demierre, B. Steitz, A. Finka, H. Hofmann, J. A. Hubbell, and P. Renaud. Dielectrophoresis-based particle exchanger for the manipulation and surface functionalization of particles. *Lab on a Chip*, 8:267–273, 2007.

[108] W. T. Winter and M. E. Welland. Dielectrophoresis of non-spherical. *Journal of Physics D: Applied Physics*, 42:1–6, 2009.

[109] P. Linderholm and P. Renaud. Comment on ”ac frequency characteristics of coplanar impedance sensors as design parameters” by jongin hong, dae sung yoon, sung kwan kim, tae song kim, sanghyo kim, eugene y. pak, and kwangsoo no, lab chip, 2005, 5, 270. *Lab on a Chip*, 5:1416–1417, 2005.

[110] R. Schinzinger and P. A. A. Laura. *Conformal Mapping: Methods and Applications*. Elsevier, 1991.

[111] E. B. Saff and A. D. Snider. *Fundamentals of Complex analysis of Mathematics, Science, and Engineering*. Prentice Hall, second edition, 1993.

[112] K. J. Binns, P. J. Lawrenson, and C. W. Trowbridge. *The Analytical and Numerical Solution of Electric and Magnetic Fields*. Wiley, 1992.

[113] R. J. Hunter. *Zeta Potential in Colloid Science*. Acadmic Press INC, London, 1988.

[114] S. R. Deshiikan and K. D. Papadopoulos. Modified booth equation for the calculation of zeta potential. *Colloid Polymer Science*, 276:117–124, 1998.

[115] http://rsbweb.nih.gov/ij/.

[116] T. B. Jones. Liquid dielectrophoresis on the microscale. *Journal of Electrostatics*, 51-52:290–299, 2001.

[117] R. S. Kane, S. Takayama, E. Ostuni, D. E. Ingber, and G. M. Whitesides. Patterning proteins and cells using soft lithography. *Biomaterials*, 20:2363–2376, 1999.

[118] A. Bernard, E. Delamarche, H. Schmid, B. Michel, H. R. Bosshard, and H. Biebuyck. Printing patterns of proteins. *Langmuir 1998*, 14:2225–2229, 1998.

[119] J. L. Tan, J. Tien, and C. S. Chen. Microcontact printing of proteins on mixed self-assembled monolayers. *Langmuir*, 18:519–523, 2002.

[120] C. D. James, R. C. Davis, L. Kam, H. G. Craighead, M. Isaacson, J. N. Turner, and W. Shain. Patterned protein layers on solid substrates by thin stamp microcontact printing. *Langmuir*, 14:741–744, 1998.

[121] S. D. Senturia. *Microsystem Design*. Springer, 2001.

[122] http://www.dowcorning.com/applications/search/products/.

[123] X. Ye, H. Liu, Y. Ding, H. Li, and B. Lu. Research on the molding process for high quality pdms molds. *Microelectronic Engineering*, 86:310–313, 2009.

[124] A. Holmberg, A. Blomstergren, O. Nord, M. Lukacs, J. Lundeberg, and M. Uhlén. The biotin-streptavidin interaction can be reversibly broken using water at elevated temperatures. *Electrophoresis*, 26:501–510, 2005.

[125] J. O. Foley, E. Fu, L. J. Gamble, and P. Yager. Microcontact printed antibodies on gold surfaces: Function, uniformity, and silicone contamination. *Langmuir*, 24:3628–3635, 2008.

[126] J. P. Renault, A. Bernard, A. Bietsch, B. Michel, H. R. Bosshard, E. Delamarche, M. Kreiter, B. Hecht, and U. P. Wild. Fabricating arrays of single protein molecules on glass using microcontact printing. *Journal of Physical Chemistry*, 107:703–711, 2003.

[127] M. E. Browning-Kelley, K. Wadu-Mesthrige, V. Hari, and G. Y. Liu. Atomic force microscopic study of specific antigen/antibody binding. *Langmuir*, 13:343–350, 1997.

[128] J. Castillo, S. Tanzi, M Dimaki, and W. Svendsen. Manipulation of self-assembly amyloid peptide nanotubes by dielectrophoresis. *Electrophoresis*, 29:5026–5032, 2008.

[129] N. B. Sopher, Z. R. Abrams, M. Reches, E. Gazit, and Y. Hanein. Integrating peptide nanotubes in micro-fabrication processes. *Journal fo Micromechanics and Microengineering*, 17:2360–2365, 2007.

[130] K. Haubert, T. Drierb, and D. Beebe. Pdms bonding by means of a portable, low-cost corona system. *Lab on a chip*, 6:1548–1549, 2006.

Appendix A

Electrical Field of Planar Electrodes

In standard cleanroom fabrication of microfluidic systems the electrodes are normally defined on a plane (bottom or top of a liquid channel) making the calculation of the electric field not a straight forward task. In order to determine an analytical expression for the electrical field with this electrode geometry in the channels conformal mapping is used [16]. It is assumed that the electric field is invariant in the height of the channel. This is not precisely true as there will be some variation with height depending on the electrode distance from the main channel. The geometry is defined in the z-plane (as a complex number, $z = x+iy$) [109]. For the transformation of electrical fields it goes that the potential function is invariant under the transformation (as it is a potential difference) [110], so

$$\Phi_z(x, y) = \Psi_w(n, m), \tag{A.1}$$

where Φ_z are the potential in the device geometry, $x(n, m)$, $y(n, m)$ are the coordinates, Ψ_w is potential in the transformed geometry, and $n(x, y)$, $m(x, y)$ are the coordinates in w space with $w = n + im$. So using equation A.1 the derivatives of Φ_z with respect to x, y become (using the chain rule[111])

$$\begin{aligned}\frac{\partial \Phi_z}{\partial x} &= \frac{\partial \Psi_w}{\partial n}\frac{\partial n}{\partial x} + \frac{\partial \Psi_w}{\partial m}\frac{\partial m}{\partial x} \\ \frac{\partial \Phi_z}{\partial y} &= \frac{\partial \Psi_w}{\partial n}\frac{\partial n}{\partial y} + \frac{\partial \Psi_w}{\partial m}\frac{\partial m}{\partial y}.\end{aligned} \tag{A.2}$$

In order to obtain the electric field one needs the gradient of the potential[45]. As a complex geometry is used the complex gradients (∇_c) of Φ_z and Ψ_w are needed[110]

$$\begin{aligned}\nabla_c \Phi_z &= \frac{\partial \Phi_z}{\partial x} + i\frac{\partial \Phi_z}{\partial y} \\ \nabla_c \Psi_w &= \frac{\partial \Psi_w}{\partial n} + i\frac{\partial \Psi_w}{\partial m}.\end{aligned} \tag{A.3}$$

Inserting equations A.2 into the first equation A.3 one gets

$$\nabla_c \Phi_z = E_z = (\frac{\partial \Psi_w}{\partial n}\frac{\partial n}{\partial x} + \frac{\partial \Psi_w}{\partial m}\frac{\partial m}{\partial x}) + i(\frac{\partial \Psi_w}{\partial n}\frac{\partial n}{\partial y} + \frac{\partial \Psi_w}{\partial m}\frac{\partial m}{\partial y}),$$

where E_z is the electric field in z space. Using the Cauchy-Riemann equations (see [111] p. 58), one can get rid of the y dependence and the electric field then becomes

$$E_z = (\frac{\partial \Psi_w}{\partial n}\frac{\partial n}{\partial x} + \frac{\partial \Psi_w}{\partial m}\frac{\partial m}{\partial x}) + i(-\frac{\partial \Psi_w}{\partial n}\frac{\partial m}{\partial x} + \frac{\partial \Psi_w}{\partial m}\frac{\partial n}{\partial x}) =$$

$$(\frac{\partial \Psi_w}{\partial n} + i\frac{\partial \Psi_w}{\partial m})(\frac{\partial n}{\partial x} - i\frac{\partial m}{\partial x}). \tag{A.4}$$

The first term of equation A.4 is the electric field in the w geometry, while the second term is the complex conjugate derivative of w with respect to z (see [111] p. 58). The equation can then be written as

$$E_z = E_w \overline{\frac{dw}{dz}}. \tag{A.5}$$

This can be done for any number of transformations. There will be three transformations needed (see explanation later) so the electric field can be written as

$$E_z = E_w \overline{\frac{dw}{dv}\frac{dv}{du}\frac{du}{dz}}, \tag{A.6}$$

where v and u are the complex coordinates in two other planes.

As the potential is invariant under the transformations a parallel plate capacitor will be the starting system [109, 16]. The field is then given as [45]

$$E_w = \frac{V}{w_d}, \tag{A.7}$$

where E_w is the electric field in the w space, V is the potential difference, and w_d is the distance between the plates in the w space. As the channel is made from an insulating material (SU-8 and Pyrex) it is assumed that the field is confined in the channel and therefore can be described as a two dimensional system as sketched in figure A.1 A. In order to transform the planar electrode system in to a parallel plate capacitor geometry three transformations and a symmetry argument are used. The transformations of the electric field are sketched in figure A.1.

First as the field is symmetric (in the z geometry) between the electrodes, only half of the geometry has to be transformed (see figure A.1 B). A sinh transformation is then done in order to map the electrodes on one axis with no wall confinement meaning that the geometry ($u(z)$) does not have any wall at the top

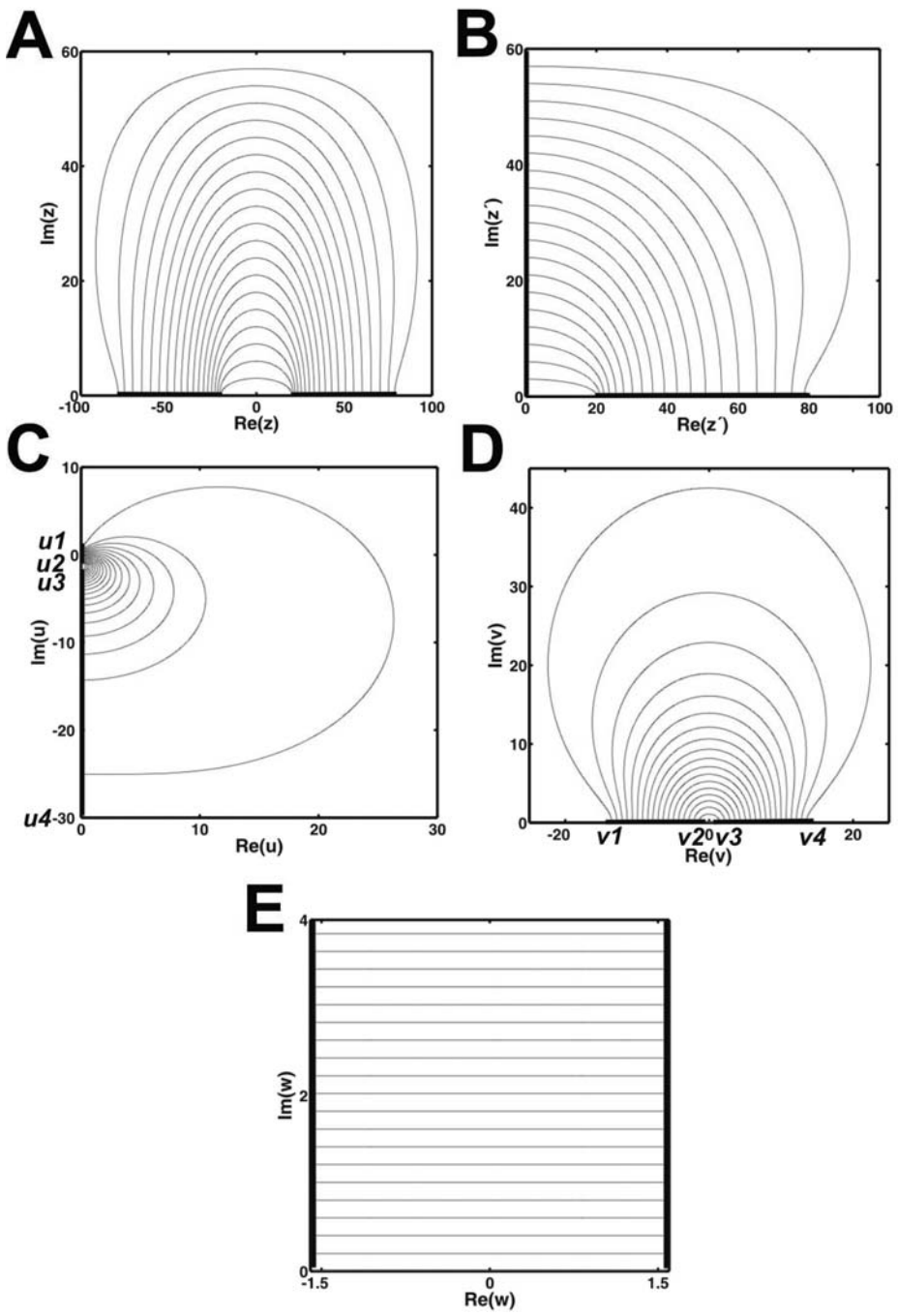

Figure A.1: A) The electric field distribution of the main channel B) the electric field distribution using a symmetry argument C) sinh transformation transform the geometry in z´ space into u space where the system does not have any confinement D) the Möbius transformation transforms the uneven sized electrodes in a space where the electrodes are even size E) the Schwartz-Christoffel transformation transforms the electrodes into a parallel plate capacitor system.

and the field expands in principle to infinity. This is shown in figure A.1 C. The sinh transformation is given as [16]

$$u(z) = \sinh\big(\frac{\pi(z(x,y) - ia_w/2)}{a_w}\big), \tag{A.8}$$

where a_w is the width of the channel. The derivative $\frac{du}{dz}$ is given as

$$\frac{\pi}{a_w}\cosh\big(\frac{\pi(z(x,y) - ia_w/2)}{a_w}\big). \tag{A.9}$$

Next as shown in figure A.1 D a Möbius transformation is used to transform the electrode into a plane where they have the same size [16] in order to use a Schwartz-Christoffel transformation to get a plate capacitor geometry. The Möbius transformation is given as

$$v(u) = \frac{Au(z) + b}{Cu(z) + D}, \tag{A.10}$$

where A, b, C, and D are constants. Equation A.10 can be rewritten to

$$v(u) = A\frac{u(z) + B}{Cu(z) + D}, \tag{A.11}$$

where $B = \frac{b}{A}$. The constant A can by looking at equations A.6 and A.7 be set to 1 as it cancels out in the transformation. B, C, and D need to be determined. For the determination of the constants, we use that the electrodes need to be transformed to a geometry without confinement as well as same size electrodes. Further, in order to make the last transformation simpler the coordinates of the corners of the electrodes in v space will be defined as $v1 = -v4$, $v2 = -1$, $v3 = 1$, and $v4 = 1/k$ (see figure A.1 D), where k^2 is defined as the modulus of the elliptic integral of the first kind [16]. The corners of the electrodes in the u plane are defined as $u1$, $u2$, $u3$, and $u4$, see figure A.1 C. These conditions give rise to 3 equations. In order for the electrodes in v space to have the same size and be symmetric around zero three confinements will have to be fulfilled, namely:

$$\frac{u_1 + B}{Cu_1 + D,} = -\frac{u_4 + B}{Cu_4 + D}, \tag{A.12}$$

$$\frac{u_2 + B}{Cu_2 + D} = -1, \tag{A.13}$$

$$\frac{u_3 + B}{Cu_3 + D} = 1. \tag{A.14}$$

Further equation A.12 is a second order equation which will give two solutions: either $|v_1|, |v_4| > |v_2|, |v_3|$ or $|v_1|, |v_4| < |v_2|, |v_3|$. In order to make the Schwartz-Christoffel transformation simpler the solution which gives $|v_1|, |v_4| > |v_2|, |v_3|$ is chosen, which gives $k < 1$. From equation A.14, D is determined as

$$D = u_3(1 - C) + B, \tag{A.15}$$

as a function of B and C. While equations A.13 and A.15 give B as

$$B = (u_3(C - 1) - u_2(1 + C))/2, \tag{A.16}$$

as a function of C. Using equations A.12, A.15, and A.16 one gets the equation for C as

$$\frac{u_1 + (u_3(C-1) - u_2(1+C))/2}{Cu_1 + u_3(1-C) + (u_3(C-1) - u_2(1+C))/2} = -\frac{u_4 + (u_3(C-1) - u_2(1+C))/2}{Cu_4 + u_3(1-C) + (u_3(C-1) - u_2(1+C))/2}, \tag{A.17}$$

which results is C to be

$$C = \frac{u_3^2 + u_2^2 - u_4u_2 - u_1u_3 - u_4u_3 - u_1u_2 + 2u_1u_4}{u_4u_2 + u_1u_2 - u_4u_3 - u_1u_3 + u_3^2 - u_2^2} - \frac{2\sqrt{(u_3 - u_4)(u_2 - u_4)(u_3u_2 - u_1u_2 - u_1u_3 + u_1^2))}}{u_4u_2 + u_1u_2 - u_4u_3 - u_1u_3 + u_3^2 - u_2^2}. \tag{A.18}$$

The derivative of this transformation is

$$\frac{dv}{du} = \frac{D - BC}{(D + Cu)^2}. \tag{A.19}$$

The last transformation (Schwartz-Christoffel transformation) is done in order to get a planar plate system without confinement[16]. Figure A.1 E shows the electric field distribution and channel geometry of the parallel plate capacitor. The Schwartz-Christoffel transformation for this system is given as (see [112] p. 150 for a full definition)

$$\frac{dw}{dv} = S(v - v1)^{-\alpha_1/\pi}(v - v2)^{-\alpha_2/\pi}(v - v3)^{-\alpha_3/\pi}(v - v4)^{-\alpha_4/\pi}, \tag{A.20}$$

where S is a constant and $v1$, $v2$, $v3$, and $v4$ are the coordinates of the electrodes in the transformed geometry (see figure A.1 B) and α_1, α_2, α_3, and α_4 are the angle of the corners between the coordinates of the electrodes in w space, see figure A.1 E. The defined coordinates of the corners of the electrodes in v space are as mentioned before $v1 = -v4$, $v2 = -1$, $v3 = 1$, and $v4 = 1/k$. Inserting this into equation A.20 and using that all the angles are orthogonal equation A.20 becomes

$$\frac{dw}{dv} = S(v + 1/k)^{-1/2}(v + 1)^{-1/2}(v - 1)^{-1/2}(v - 1/k)^{-1/2} =$$

$$S((v^2+1/k+v+v/k)(v^2+1/k-v-v/k))^{-1/2} =$$
$$S(v^4+v^2/k-v^3-v^3/k+v^2/k+1/k^2-v/k-v/k^2+v^3+v/k-v^2-$$
$$v^2/k+v^3/k+v/k^2-v^2/k-v^2/k^2)^{-1/2} =$$
$$S(v^4+1/k^2-v^2-v^2/k^2)^{-1/2} = S(k^2(k^2v^4+1-v^2k^2-v^2))^{-1/2} =$$
$$S\cdot k\frac{1}{((1-v^2)(1-k^2v^2))^{1/2}}. \tag{A.21}$$

The constant S determines the scale and rotation of the geometry of the system in the w plane [110]. Looking at equations A.6 and A.7 one realizes that the constant $S\cdot k$ cancels out in the transformation and will therefore in the following calculations be set equal to 1.

In order to make calculations using the electric field feasible, determining the w space as a function of v space is necessary. So integrating equation A.21 with respect to v one gets

$$w = \int \frac{1}{((1-v^2)(1-k^2v^2))^{1/2}}dv + KC, \tag{A.22}$$

where KC is a constant. As there is no analytical solution to equation A.22, it can only be evaluated for specific cases. Equation A.22 can be written as a defined integral as

$$w = \int_{v_{x2}}^{v_{x1}} \frac{1}{((1-tt^2)(1-k^2tt^2))^{1/2}}dtt, \tag{A.23}$$

where tt is the integral value and v_{x1} and v_{x2} are coordinates in the v space. Equation A.23 is defined as the elliptic integral of the first kind [112]. As stated above the transformation to v space is defined so that coordinates of the corners of the electrodes in v space are given as $v1=-v4$, $v2=-1$, $v3=1$, and $v4=1/k$. To get the dimensions (distance and size of the plates) of the parallel plate capacitor in w space these values are used in equation A.23 so the distance between the plates is given as

$$w_d = \int_{-1}^{1} \frac{1}{((1-tt^2)(1-k^2tt^2))^{1/2}}dtt. \tag{A.24}$$

This can be rewritten as

$$w_d = \int_{-1}^{1} \frac{1}{((1-tt^2)(1-k^2tt^2))^{1/2}}dtt = 2\cdot\int_{0}^{1} \frac{1}{((1-tt^2)(1-k^2tt^2))^{1/2}}dtt. \tag{A.25}$$

This integral is defined as the complete elliptic integral of the first kind [110] and its solutions are given as $K(k)$, with k as the modulus. So the distance between the two plates can be described using the distance in v space as

$$w_d = 2\cdot K(k) = 2\cdot\int_{0}^{1} \frac{1}{((1-tt^2)(1-k^2tt^2))^{1/2}}dtt, \tag{A.26}$$

where w_d is the distance between the plates. Looking at figure A.1 D the length of the plates (w_e) in the w space using the coordinates of the electrodes in v space is given as

$$w_e = \int_1^{1/k} \frac{1}{((1-tt^2)(1-k^2tt^2))^{1/2}} dtt, \tag{A.27}$$

where w_e is the length of the plates in w space plane. Equation A.27 can be rewritten as

$$w_e = \int_0^{1/k} \frac{1}{((1-tt^2)(1-k^2tt^2))^{1/2}} dtt -$$
$$\int_0^{1} \frac{1}{((1-tt^2)(1-k^2tt^2))^{1/2}} dtt = K(\sqrt{1-k^2}), \tag{A.28}$$

where $\sqrt{1-k^2}$ is called the complementary modulus.

The full equation for the transformation for the electric field is then given as (see equations A.6, A.4, A.9, A.19, A.21, and A.25)

$$E_z = \frac{1}{2}\frac{V}{2K(k^2)}\cdot$$

$$\overline{\frac{1}{((1-v^2)(1-k^2v^2))^{1/2}} \frac{D-BC}{(D+Cu)^2} \frac{\pi}{a_w} \cosh\left(\frac{\pi(z(x,y)-ia_w/2)}{a_w}\right)}, \tag{A.29}$$

where the factor $\frac{1}{2}$ is due to the symmetry argument.

A.1 Electromobility Estimation of Chromosomes

To describe particle movement under the influence of an electrical field the properties of the particles (as well as the liquid) must be known. One technique that can be used is electrophoresis; the electromobility of the particles can be calculated with this method. In this section an estimate of an average electromobility of metaphase chromosomes was made by using a micro-fluidic chip mounted on a microscope.

A.1.1 Theory

Particles moving in a liquid under an applied electrical field will experience two forces [48]. The electric force (F_{el}) on a particle is $F_{el} = qE_f$ [45], where q is the net charge of the particle, and E_f is the electrical field. If it is assumed that the motion is steady-state and that the liquid is not affected by the electric field, the total force (F_t) acting on the particle is zero or

$$\bar{F}_t = \bar{F}_d + \bar{F}_{el} \Leftrightarrow |\bar{F}_d| = |\bar{F}_{el}|. \tag{A.30}$$

This is a good assumption if the electric field is uniform. Inserting equation 4.2 for the drag force and the electric field force in equation A.30 one can find the velocity of the particle under the influence of an electric field

$$6\pi\eta a_r v_l = qE_f \Leftrightarrow v_l = \frac{q}{6\pi\eta a_r}E_f. \tag{A.31}$$

The electromobility is then given as $\frac{q}{6\pi\eta a_r}$ or

$$\mu_e = \frac{v_l}{E_f}, \tag{A.32}$$

where μ_e is the electromobility. This equation also assumes that the particle is "far" from the walls of the channel. As there will be some electroosmosis the Zeta potential, ζ, would have needed to be estimated. The electromobility depending on the Zeta potential is given as

$$\mu_e = C_m\frac{\epsilon\zeta}{\eta}, \tag{A.33}$$

where ϵ is the permittivity of the medium and C_m is a constant depending on the size of κa_r, where κ^{-1} is the Debye length [113, 114]. Unfortunately there was not enough time during the project to do this and the necessary equipment was also not readily available.

A.1.2 Simulation of the electric field

The MATLAB^{TM} program used for these simulations can be found in appendix D.2. The program is based on the analysis presented in appendix A.

The simulation was done with an applied potential of 10V. The large peak just over the electrodes at a height of 5 μm is caused by the edges of the electrodes. As figure A.2 shows the field is absolutely uniform in most of the channel, i.e. also within the central 1 mm where the observations take place. From numerical simulations with COMSOL^{TM} we found that the variation of the field in this area is in the 4th decimal digit, i.e. non existent. This is excellent for obtaining a reasonable estimate of the mobility.

A.1.3 Experimental Setup

The setup consisted of a fluorescence microscope (model Nikon TE2000U with a 535-590 nm filter), with a Photometrics®Cascade®II:512) CCD camera, a DC power supply (model Agilent, E3643A), and a holder containing; a microfluidic chip, liquid reservoirs, and electrical connections to the chip (consisting of spring contacts Harwin model P13-1123) both of which are glued to the holder. The microscope was fitted with a 20X objective lens (model: Nikon 20X 0.5 DIC

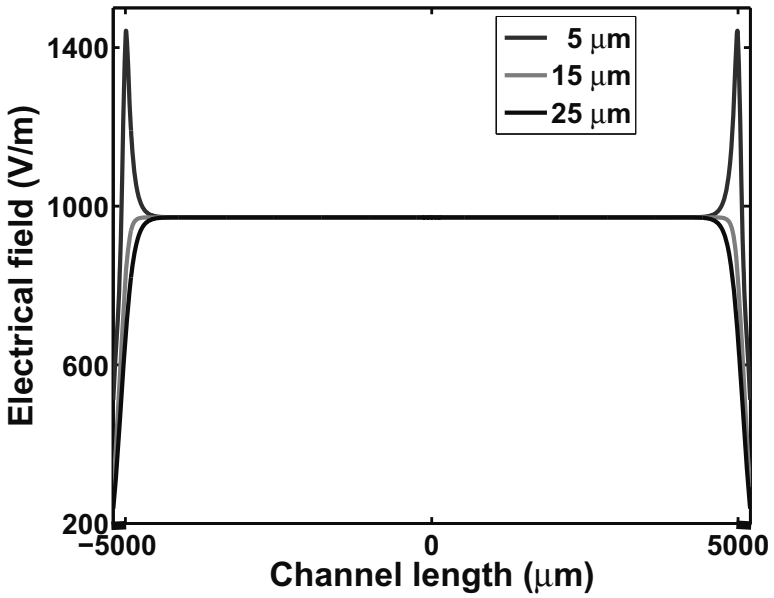

Figure A.2: MATLAB^{TM} simulation of the electric field in the channel at the height of 5, 15, 25 μm above the planar electrodes with an applied potential of 10V. The black at the corners of the x axis symbolizes the electrodes.

M/N2 Air). The power supply is connected to the holder's electrical contacts. Figure A.3 shows a schematic drawing of the cross section of the holder. The potential applied to the electrodes was 10V DC.

The micro-fluidic system in the holder consists of a 2x2 cm Pyrex chip (see appendix B) on which platinum electrodes are defined by photolithography. On top of the platinum electrodes are channels defined in SU-8. The chip is reversibly sealed by a piece of casted PDMS with through holes for electrode and liquid connections. The PDMS lid and chip are held together by two pieces of PMMA through notches, as shown in figure A.3. Figure A.4 shows a schematic layout of the Pyrex chip with the electrodes and channels. The electrodes are embedded in the SU-8 except at the rectangular parts. The dimensions of the structures were 10 mm long and 100 μm wide channel in SU-8 with 100 μm wide 130 nm high electrodes in platinum (see appendix B).

The preparation for an experiment is as follows: First the chromosome solution is mixed with a Polyvinylpyrrolidone (PVP) solution (Sigma: P5288) so the concentration 0.1% W/V is obtained. One reservoir is then filled with chromosome solution while suction is applied at the other end in order to fill the channel with the chromosome solution. The chip is left for 20 minutes in order for the flow to stabilize. The chip is then mounted on the microscope and the power supply is connected. Chromosomes are then located in the channel and a potential is ap-

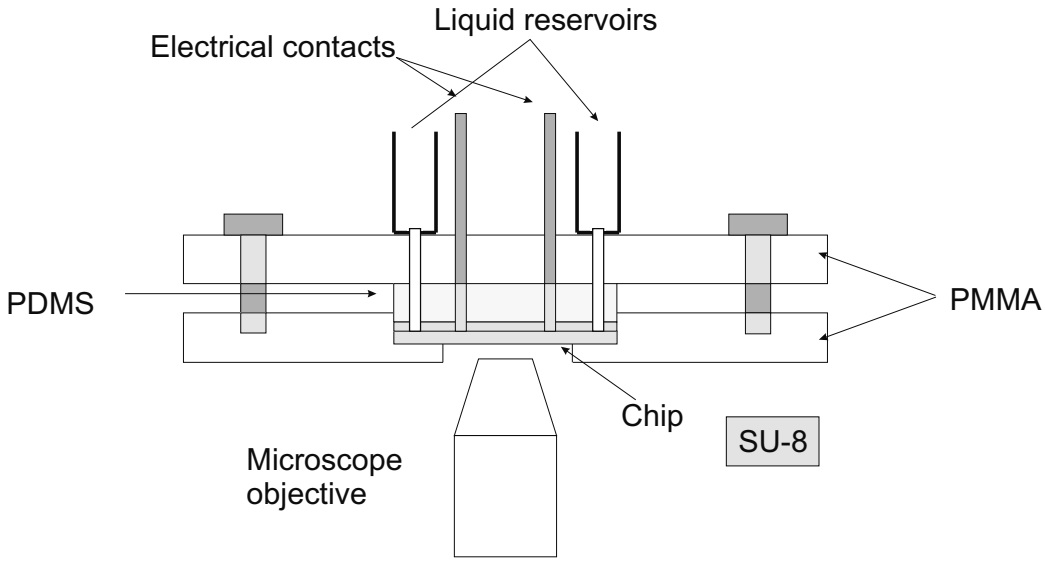

Figure A.3: Schematic drawing of the cross section of the holder used for electromobility measurements of chromosomes. The chip with the PDMS lid is mounted between two pieces of PMMA which contain the connections (liquid and electric).

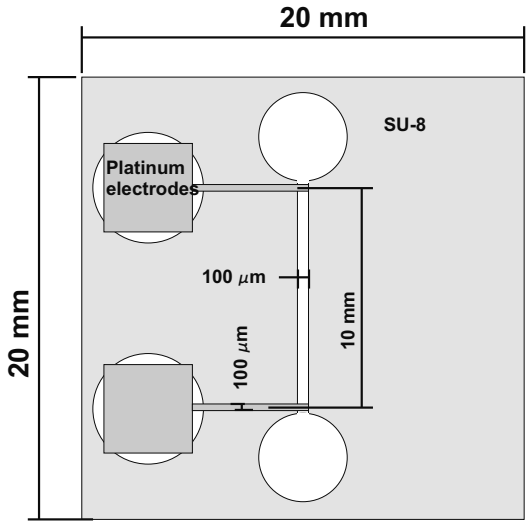

Figure A.4: Schematic layout of the Pyrex chip with the electrodes and channels. The chip was used for electromobility experiments with chromosomes.

plied while the movement of the chromosomes is recorded with the CCD camera. Afterwards a potential of the same amplitude but with negative sign is applied and the same procedure is done. For the electromobility and dielectrophoresis experiments the solution was stained with propidium iodide.

A.1.4 Results

The recorded images were analyzed with ImageJ [115] in order to obtain the velocity the experiment was made so the chromosomes were moved in both directions. The different in obtained velocity values for the chromosomes in the two directions was found to be $5\ \%$. Figure A.5 shows the distribution of the different velocities of the chromosomes. The chromosomes were moving towards the positive electrode every time, indicating a negative charge.

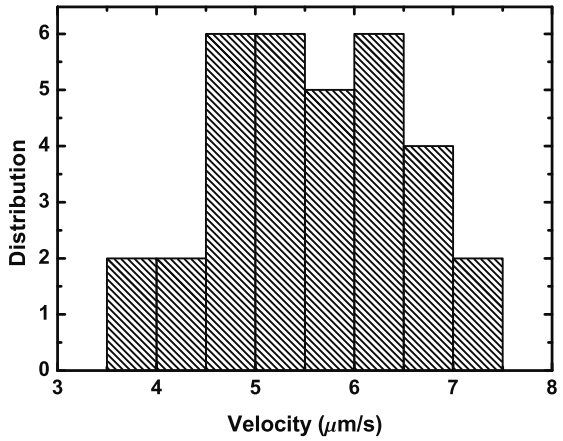

Figure A.5: Plot of the velocity distribution of different human chromosomes.

The average velocity of the chromosomes is 5.545 μm/s with a standard deviation of 0.99 μm/s. This variation could be attributed to the different sizes of the human chromosomes, however more experimental data is needed in order to verify this statement. Using equation A.32 an estimate of the average electrophoretic mobility is found to be 5.446 nm/s per V/m, with an uncertainty of 0.97 nm/s per V/m. Based on these numbers and equation A.32 the measured average charge on the chromosomes is $1.2 \cdot 10^{-16} \pm 0.21 \cdot 10^{-16}$ Cb. This calculation is based on a medium viscosity of 0.001 Pa·s and an average radius for the chromosomes of 1.5 μm, as measured by AFM.

A.2 Electric Field Calculations of the 2^{nd} Generation DEP Chip

To optimize this system in order to get the best deflection and hence the best readout, several of the system parameters can be varied. The applied potential, should be as high as possible without causing any unwanted effects e.g. like heat-

ing of the liquid which will in turn cause unwanted flow [116]. For the experiments described in this project an amplitude of 10 V was used since investigation of the electric signal showed that it got distorted at higher amplifications (especially at higher frequencies). Another way to optimize the system is to vary the dimensions of the system (channel height, channel width, gap between the electrodes, electrode width (access channel width), electrode length, and electrodes position in the access channels).

The channel height and the position of the electrodes in the access channels determine the uniformity of the field in the main channel. Further the optical setup used puts some restrictions on the dimensions of the electrode area. Therefore simulations of the potential in the channel were first carried out by varying the ratio of the gap between the access channels and the electrode width (see figure 4.4). As the electric field is far from uniform (see figure A.1) the best parameter to investigate is the effective potential (V_{eff}) in the channel. In figure A.6 it is shown how the parameters, which can be varied during the fabrication process can influence the effective potential (see appendix D.3 for the program).

Figure A.6 A) to E) shows the simulated effective potential as a function of the different system parameters. The simulations were done with one parameter being varied while the rest are kept constant. When kept constant the parameters were given the values they had in the fabricated device (system height 30 μm, main channel width 60 μm, gap width 40 μm, electrode width 60 μm, metal electrode length 30 μm, electrode distance from main channel 20 μm).

As figure A.6 A) shows, the effective potential increases with increasing system height. At the start of the plot there is deviation from the more or less smooth trend; this can only be attributed to the calculation of the cell constant of the access channels, as this is the only place in the program (see appendix D.2) where approximation is used for calculating the complete elliptical integral of the first kind. For this system a height of 30 μm was chosen to make it easier to identify chromosomes at different heights in the channel when analyzing the data. Figure A.6 B) shows the effective potential as a function of the main channel width. As the plot shows the potential drops with increasing channel width. This of course indicates that this geometry parameter should be as small as possible. Unfortunately, as the main channel width becomes smaller, the harder it is to maintain a flow rate which can be detected with a CCD camera. As the pumps used in this experiment have a minimum flow rate of 0.1 μl/minute this gives a velocity of the liquid of $\approx$ 1.4 mm/s [48], using a viscosity of 10^{-3} Pa·s [48], if a main channel width of 60 μm is used. At this velocity the camera used in the setup can obtain 25-30 images of the particle passing the electrode area. Figure A.6 C) shows the effective potential as a function of the gap between the access channels. As can be seen the effective potential increases with increasing gap size.

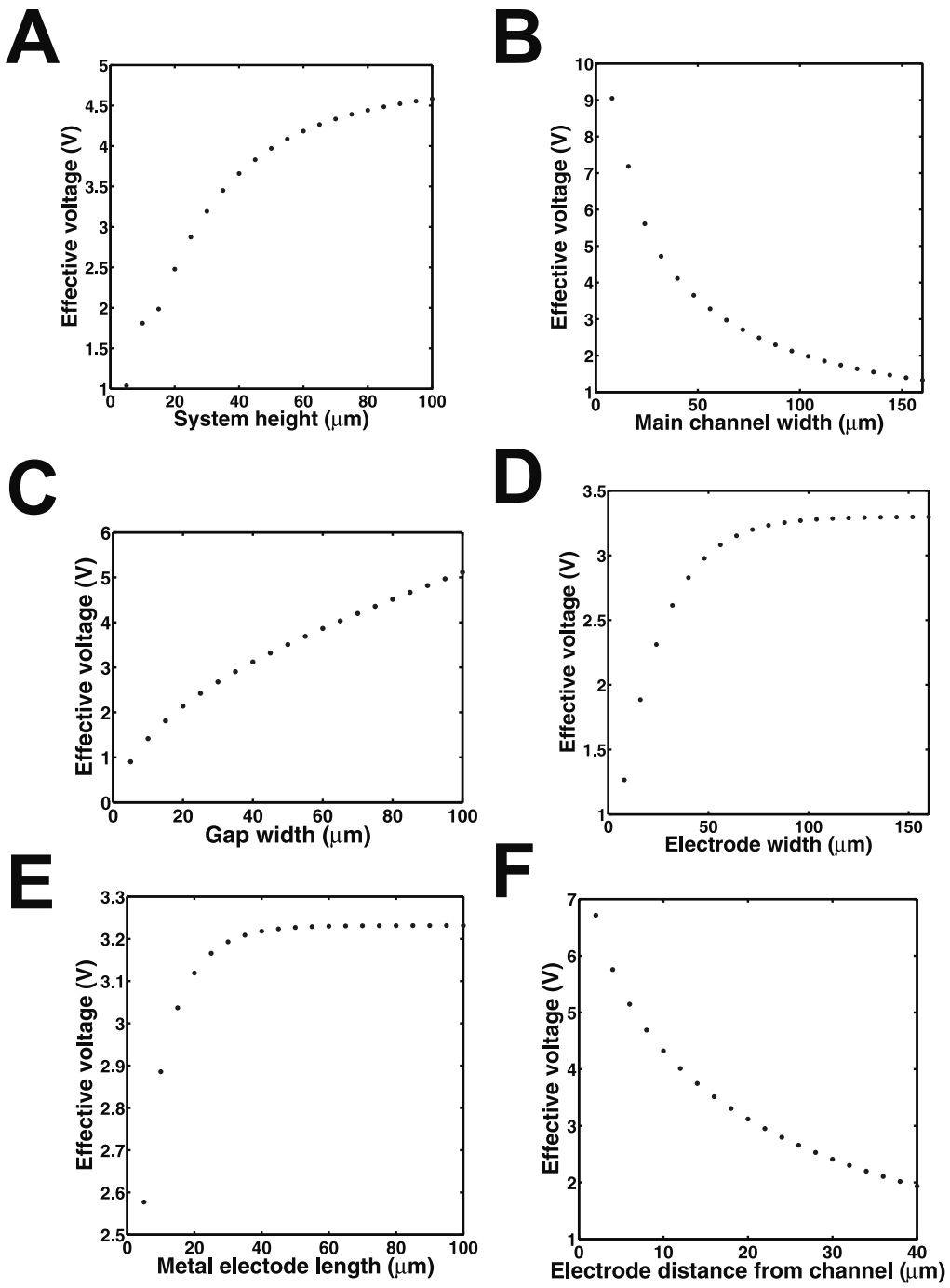

Figure A.6: MATLAB^{tm} simulation of the effective potential in the main channel depending on design parameters of the system, A) system height, B) main channel width, C) gap width, D) electrode width, E) metal electrode length, F) electrode distance from main channel.

The chosen value for this geometry parameter will be discussed below. Figure

A.6 D) shows the effective potential as a function of the electrode width (access channel width). As can be seen the effective potential increases with increasing electrode width until it saturates after a certain electrode width value. The value chosen for this geometry parameter will be discussed below. Figure A.6 E) shows the effective potential as a function of the metal electrode length. As can be seen the effective potential increases with increasing electrode length until around 30 to 40 μm above which the value saturates. The value used was 30 μm. Figure A.6 F) shows the effective potential as a function of the electrode distance from the main channel (access channel length-metal electrode length). As can be seen the effective potential decreases with increasing distance. A distance of 20 μm from the channel was chosen as an estimate in order to maintain the assumption that the field in the main channel is more or less uniform in the system height direction.

As discussed above, the optimal effective potential requires the gap between the electrodes to be as large as possible. However, as one also needs to be able to detect the trajectories of the chromosomes in the channel, the area of interest (electrodes plus a bit more) needs to fit to the view of the microscope in use. Therefore, the gap between the electrodes and the electrode width are solely determined by geometrical considerations, i.e the available observation view. The area of view of the microscope was around 300 × 300 μm and as some area is needed at each end of the image to estimate the deflection of the particles, the total length of the gap and the width of the electrodes was set to 160 μm. Figure A.7 shows the potential in the main channel as a function of the ratio of the gap and electrode width. All other parameters are the same as in the simulation above.

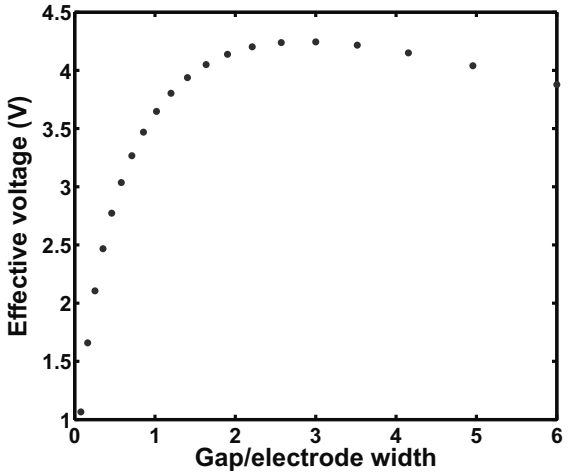

Figure A.7: MATLAB^{tm} simulation of the effective potential as a function of the relation of the electrode gap divided by the electrode length.

The optimal ratio of the gap and electrode width is about 2.5. In the exper-

imental setup, used for the experiments, this ratio was 0.66. Due to this, larger applied voltages are needed to generate a particular DEP force in our experimental system than could be the case if the system was fully optimized.

Appendix B

Fabrication Processes

B.1 Process Sequence

Process sequence for backgate substrates used in EFM-phase.

Step	process	Parameters
1	starting wafers	Si (100), ON30 (ON92), diameter = 4”, single polished
2	Oxide grow	100nm, Phosphor drive-in furnace, wet oxidation, time = 25 min., T = 1000°C
3	Removal of oxide on back side	Add blue film on front side, BHF etch, time = 4 min.
4	Deposit Ti/Au	Alcatel E-beam metal Ti thickness = 10 nm, Ti deposition rate = 2Å/s Au thickness = 1000 nm, Au deposition rate = 10Å/s

Process sequence for micro-fluidic systems used for electrophoresis, DEP, and impedance experiments.

Step	process	Parameters
1	Starting wafer	Pyrex, diameter = 4”, height = 525 μm, single polished
2	HMDS treatment	HMDS oven, T = 150°C, time = 30 min.
3	Spin on photo resist	SSI spinner, resist: AZ 5214E, recipe: PR1_5.RCP, thickness = 1.5 μm Prebake, T = 90°C, time = 60 s
4	1st. photolithography step (electrodes)	Dark field mask, ”positive” resist KS aligner, exposure, time = 8 s
5	Develop photo resist	KOH, time = 60 s Rinse in water, time = 5 min., spin dry
6	Deposit Ti/Pt	Alcatel E-beam metal evaporator Ti thickness = 10 nm, Ti deposition rate = 2 Å/s Pt thickness = 120 nm, Pt deposition rate = 10Å/s
7	Lift-off Ti/Pt	Acetone + ultra sound (US), time = 60 s Rinse in water, time = 5 min., spin dry
8	Dehydration of wafer	Temp = 250°C, time = 18 h.
9	Spin on SU-8 resist	KS spinner, resist: 2075, time 60sec., acc. 100 rpm, 3000 rpm prebake temp = 50°C, time = 5 hours
10	2nd. photolithgraphy step (channels)	Bright field mask, ”negative” resist KS aligner, exposure time = 30 s
11	Development	post exposure bake temp = 50°C, time = 2 hours PGMEA, rough 4 min. fine 1 min., wash IPA

B.2 Fabrication Sequence

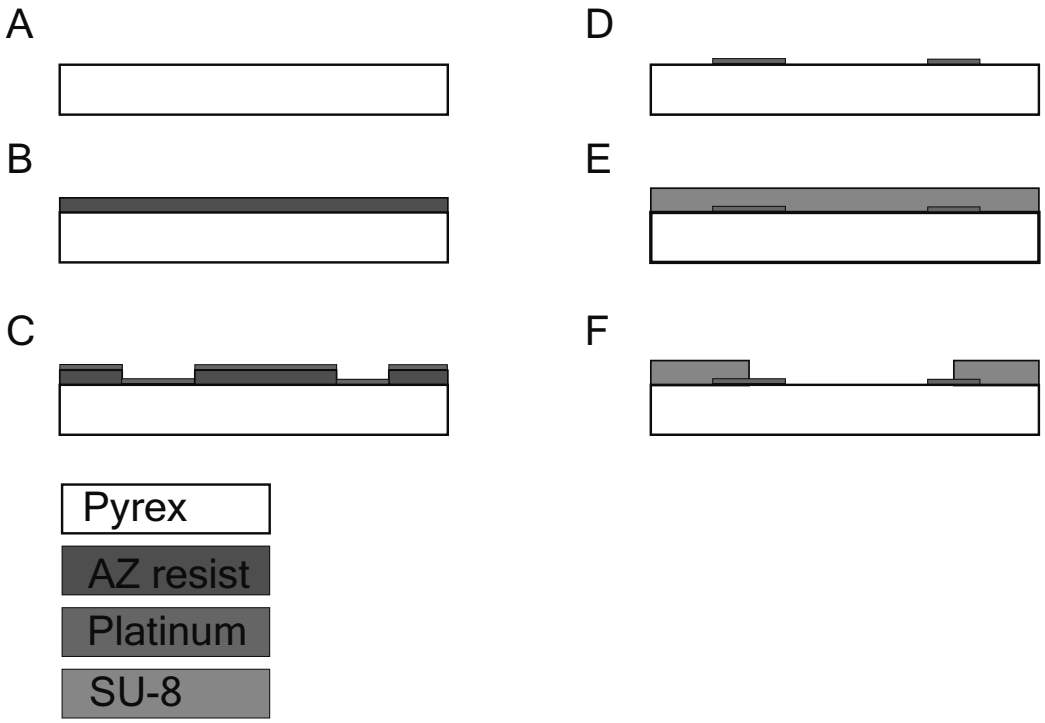

Figure B.1: Schematic illustration of the fabrication step of the micro fluidic systems A) step 1 the starting wafer; B) step 2 and 3 spinning of photo resist; C) step 4, 5, and 6 exposure, development, and evaporation of the electrodes; D) step 7 lift off the metal; E) step 8 and 9 dehydration of the wafer and spinning on of SU-8; F) step 10 and 11 exposure and development of the SU-8.

B.3 Mask Layout

The first mask layout, figure B.2, is for the estimation of the electromobility for different biological samples. All chips are 2×2 cm in size except for the one for the peptide DEP experiment which is 3×3 cm in size.

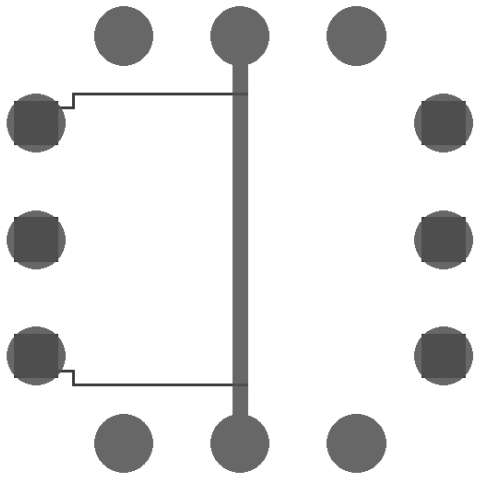

Figure B.2: Schematic drawing of the design for the estimation of the electromobility. Blue structures are metal electrodes, while red are openings in the SU-8 layer.

Figure B.3 A shows the over all layout for the chip used for trying to make a Coulter counter for chromosomes. The electrodes are either parallel along the channel length or parallel across the channel (see figure B.3 B).

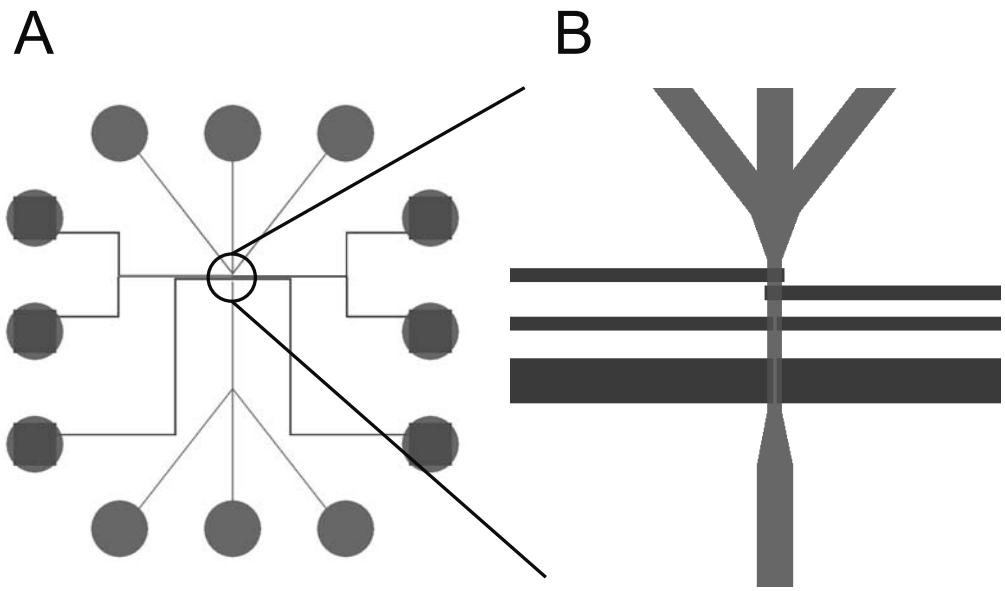

Figure B.3: Schematic drawing of the second design for impedance detection (Coulter counter). Blue structures are metal electrodes, while red are openings in the SU-8 layer.

The next mask layout (figure B.4 is based on work done by R. Tornay *et al.* [107] to move beads from one flow stream to another with an electrical field. The electrode pair on each side of the chamber are of different size and distance from each other in order to test the influence of these parameters on the manipulation of the particles. The design here is to test if the same can be done with chromosomes.

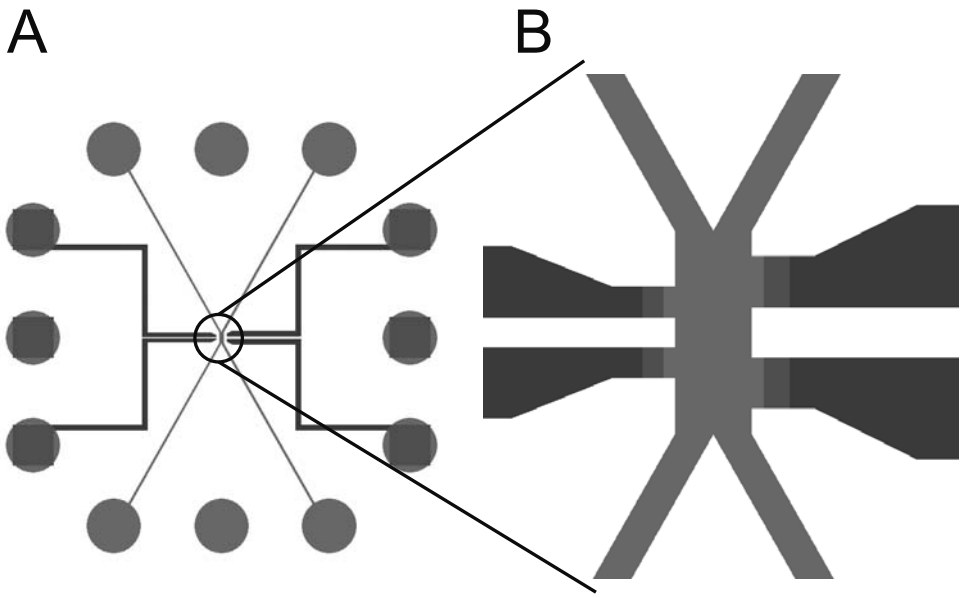

Figure B.4: Schematic drawing of one of the designs for the investigation of the dielectric response from chromosomes. Blue structures are metal electrodes, while red are openings in the SU-8 layer.

This mask layout shows the design used for the DEP experiments on the human chromosomes.

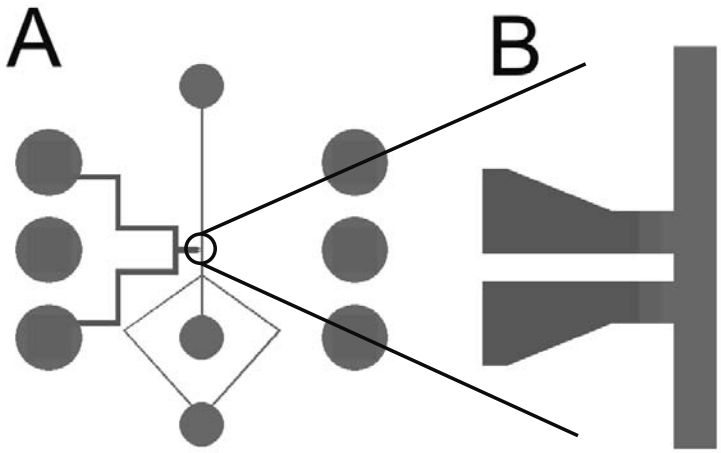

Figure B.5: Schematic drawing of the final design for the investigation of the dielectric response from chromosomes. Blue structures are metal electrodes, while red are openings in the SU-8 layer.

The mask layout shows the design used in order to make nano-sized liquid channels using dipeptide tubes as molds for PDMS. The red part in figure B.6 is SU-8 structures which serve to make a big cavity for the liquid before it enters the area with the electrodes and peptide tubes.

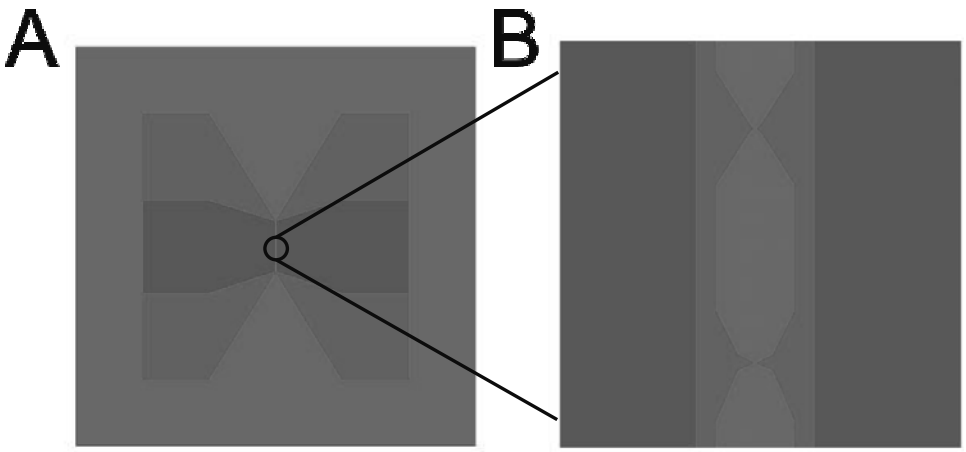

Figure B.6: Schematic drawing of the design for the experiment to make nano-sized liquid channels using dipeptide tubes as molds for PDMS. Blue and purple structures are metal electrodes, while blue are the SU-8 layer.

B.4 Fabrication process for Micro-contact Imprinting Stamp

Process sequence for micro-contact imprinting stamp used for KPM experiments on protein arrays.

Step	process	Parameters
1	Starting wafer	Si (1 0 0), diameter = 4”, height = 525 μm, single polished
2	HMDS treatment	HMDS oven, T = 150°C, time = 30 min.
3	Spin on photo resist	SSI spinner, resist: AZ 5214E, recipe: PR1_5.RCP, thickness = 4.2 μm Prebake, T = 90°C, time = 60 s
4	photolithography step (etch mask): align + expose	Bright field mask, ”negative” resist KS aligner, exposure, time = 3.5 s Inversion bake, T = 120 C, time = 100 s KS aligner, flood exposure, time = 30 s
5	Develop photo resist	KOH, time = 60 s Rinse in water, time = 5 min., spin dry
6	ASE Etch	Etch SF_6 = 260 sccm, O_2 = 26 sccm, Passivation: C_4F_8 = 120 sccm 6 cycles of 2.6 s
7	Lift-off Resist	Acetone + ultra sound (US), time = 60 s Rinse in water, time = 5 min., spin dry

B.5 Mask Layout for imprinting Stamp

The mask layout for imprinting stamps used for the protein array imprinting.

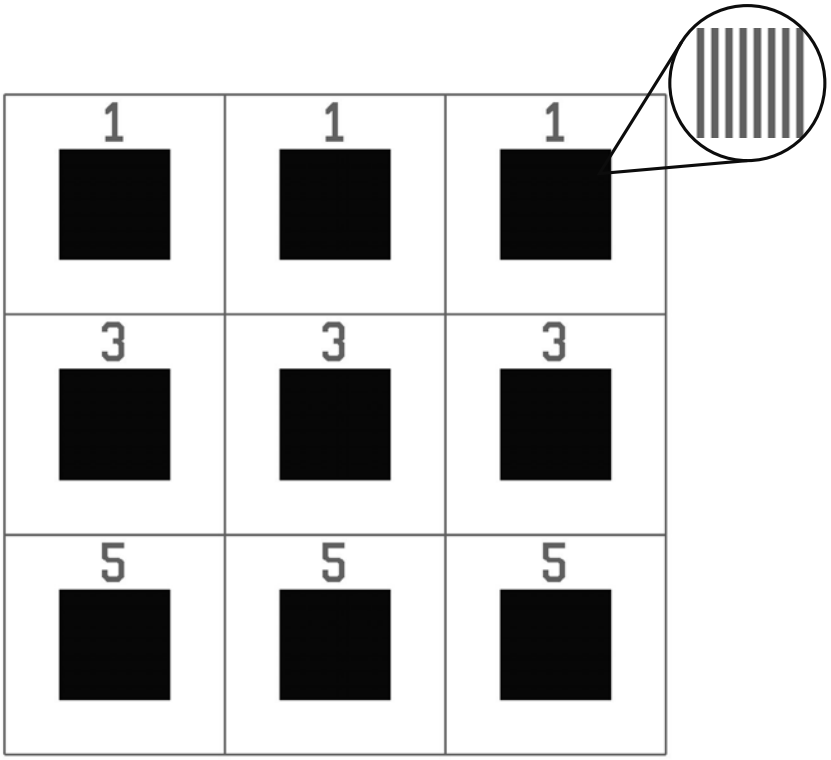

Figure B.7: The layout of the photolithography mask used to fabricate the mould for casting PDMS stamps. The number above the lines indicates the direction of the lines as well as the linewidth and line spacing given in μm.

Appendix C

The Force Gradient on the Different Parts of an AFM Cantilever

J. Colchero *et al.* [42] investigated the different electrical forces on an AFM cantilever. The formulas used for calculating the electrical forces as a function of the distance from the different parts of the AFM cantilever (not the tip) are given in the article. Here the formulas for the force gradient from the different parts of the cantilever used for plotting figure 2.13 are presented. The formulas were found on the basis of the work done by J. Colchero *et al.* [42]. z the distance between the tip and substrate, d the height of the cantilever cone, l_c length of the cantilever, w_c width of the cantilever, θ_{can} angle in radian of the titling of the cantilever with respect to the substrate, θ_{cone} angle of the cone in radian, ϵ_0 is the vacuum permitivity, r_{tip} are the radius of the tip, and V is the applied potential. Some of the parameters are shown in figure C.1.

For the cantilever part the gradient force is given as

$$\frac{\partial F_{can}}{\partial(z+d)} = \frac{2\cdot\tan^2(\theta_{can}/2)\cdot\epsilon_0\cdot l_c\cdot w_c\cdot V^2}{\theta_{can}^2\cdot d\cdot(z+d)\cdot(z+d+2\cdot l_c\cdot\tan(\theta_{can}/2))^2} - \frac{2\cdot\tan^2(\theta_{can}/2)\cdot\epsilon_0\cdot l_c\cdot w_c\cdot V^2}{\theta_{can}^2\cdot d\cdot(z+d)^2\cdot(z+d+2\cdot l_c\cdot\tan(\theta_{can}/2))}. \tag{C.1}$$

For the cone of the tip the gradient force is given as

$$\frac{\partial F_{con}}{\partial z} = \frac{4\cdot\epsilon_0\cdot\pi\cdot V^2\cdot(1-\frac{d+z-\frac{1}{2}\cdot r_{tip}\cdot\cot(\frac{\theta_{cone}}{2})^2}{z+\frac{1}{2}\cdot r_{tip}\cdot\cot(\frac{\theta_{cone}}{2})^2})}{(\pi-\theta_{cone})^2\cdot(d+z-\frac{1}{2}\cdot r_{tip}\cdot\cot(\frac{\theta_{cone}}{2})^2)} +$$

$$\frac{4\cdot\epsilon_0\cdot\pi\cdot V^2\cdot(d-r_{tip}\cdot\cot(\frac{\theta_{cone}}{2})^2)\cdot(z-\frac{1}{2}\cdot r_{tip}\cdot\cot(\frac{\theta_{cone}}{2})^2)\cdot\sin(\frac{\theta_{cone}}{2})}{(\pi-\theta_{cone})^2\cdot(z-\frac{1}{2}\cdot r_{tip}\cdot\cot(\frac{\theta_{can}}{2})^2)^2\cdot(d+z-\frac{1}{2}\cdot r_{tip}\cdot\cot(\frac{\theta_{cone}}{2})^2)} +$$

$$\frac{4\cdot\epsilon_0\cdot\pi\cdot V^2\cdot(d-r_{tip}\cdot\cot(\frac{\theta_{can}}{2})^2)\cdot(z-\frac{1}{2}\cdot r_{tip}\cdot\cot(\frac{\theta_{cone}}{2})^2)\cdot\sin(\frac{\theta_{cone}}{2})}{(\pi-\theta_{cone})^2\cdot(d+z-\frac{1}{2}\cdot r_{tip}\cdot\cot(\frac{\theta_{cone}}{2})^2)\cdot(z+\frac{1}{2}\cdot r_{tip}\cdot\cot(\frac{\theta_{cone}}{2})^2)} -$$

$$\frac{4 \cdot \epsilon_0 \cdot \pi \cdot V^2 \cdot (d - r_{tip} \cdot \cot(\frac{\theta_{cone}}{2})^2) \cdot \sin(\frac{\theta_{cone}}{2})}{(\pi - \theta_{cone})^2 \cdot (d + z - \frac{1}{2} \cdot r_{tip} \cdot \cot(\frac{\theta_{cone}}{2})^2) \cdot (z + \frac{1}{2} \cdot r_{tip} \cdot \cot(\frac{\theta_{cone}}{2})^2)}. \quad \text{(C.2)}$$

For the tip the force gradient is

$$\frac{\partial F_{tip}}{\partial z} = \frac{\epsilon_0 \cdot \pi \cdot r_{tip}^2 \cdot V^2}{(z)^3}. \quad \text{(C.3)}$$

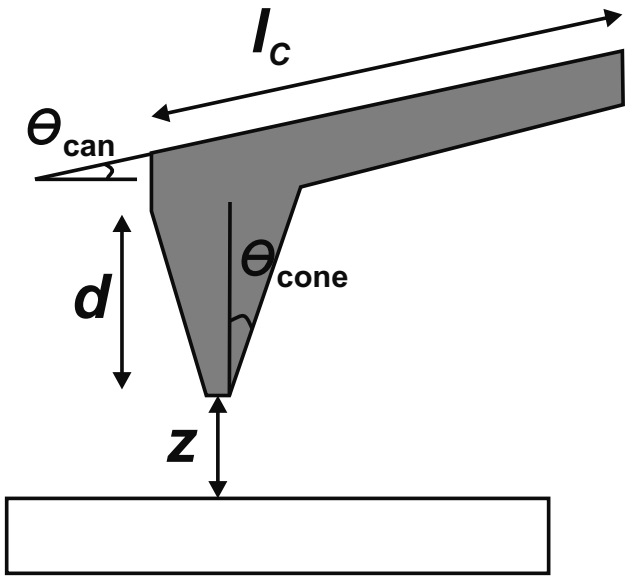

Figure C.1: Schematic drawing of some of parameters.

Appendix D

Matlab Programs

This chapter contains the scripts used for analyzing the AFM phase data and the dielectric properties of human chromosomes.

D.1 EFM-Phase Analysis Script

Script for analyzing the EFM-phase data of human chromosomes.

```
function [me_f, se_f, e_f] =
CalculateChromosomePermittivity(pfilename, tfilename)
```

Read the hdf image format to matlab.

```
pfilename = 'LPHLR03.HDF';
tfilename = 'TOPLR03.HDF';
pinfo = hdfinfo(pfilename); tinfo = hdfinfo(tfilename);
```

Get the data as image matrices and convert it to double for both topography and phase.

```
pimage = hdfread(pinfo.Filename, pinfo.SDS.Name);

pimage = double(pimage);

timage = hdfread(tinfo.Filename, tinfo.SDS.Name);

timage = double(timage);
```

Scale the images.

```
pscale = pinfo.SDS.Attributes(4);

pimage = pimage*(pscale(1).Value);

tscale = tinfo.SDS.Attributes(4);

timage = timage*(tscale(1).Value);
```

Process the images and select region of interest, followed by flat-fielding the whole topography image

```
tbackground1 = imopen(timage,strel('rectangle', [10 256]));

timage = timage - tbackground1; imshow(timage, [])
```

This crop the region of interest of the image, to get an estimate of the background phase and topography so that absolute heights and phase changes can be obtained.

```
H = imshow(timage, []); [IT, rect] = imcrop(H);

IP = imcrop(pimage, rect); figure imshow(pimage)
```

Convert the data to binary. Depending on the overall brightness of the image, the threshold will have to be adjusted.

```
BWs = im2bw(abs(IT), 0.04);

figure, imshow(BWs, []), title('binary gradient mask');
```

Find where the chromosomes are and are not.

```
chromosomesindices = find(BWs == 1);

notchromosomesindices = find(BWs == 0);

tnotchromosomes = IT(notchromosomesindices);

tbackground = ones(size(IT))*mean(tnotchromosomes);
```

Subtract background for topography and phase to get absolute values.

```
Topo = IT - tbackground;

figure title('Background subtracted topography')
imshow(Topo, [])

pnotchromosomes = IP(notchromosomesindices);

pbackground = ones(size(IP))*mean(pnotchromosomes);

Phase = IP - pbackground;

figure title('Background subtracted phase')
imshow(Phase, [])
```

Crop the specific area for the calculation (preferably long in the scanning direction and short in the other or just very small).

```
f = imshow(Phase, []);
[P, area] = imcrop(f);
T = imcrop(Topo,area);
```

Calculate the permittivity of the chromosomes

```
blank = ones(size(T));
```

Set the specific variables of the equation.

```
sp = 0.07e-6;
D = T*1e-9;
h = 0.15e-6;
t = 0.107e-6;
e_s = 3.9;
dPhi = P*pi/10000;

K = 1.081*10^-22;


V = 4;

A = t/e_s; B = 1/(h + sp + A)^3; C = dPhi/(K*V^2);
```

Calculate the permittivity of the sample.

```
e_f = D.*((((B-C).^(-1/3))-A-h-sp).^(-1));
```

Calculate the mean and standard deviation.

```
me_f = mean(mean(e_f)) se_f = mean(std(e_f))
```

D.2 Effective Voltage in Micro Channel Scripts

The scripts for the calculation of the electric field in the channel used for the plotting of the electric fields in the different geometries.

D.2.1 Script for the Transformations

```
function [Ex, Ey, Eux, Euy, Ew, u, u1, u3, u4, k, B, C, D] =
Electric_Field_in_Microchannel(elec, gap,
height, x, y, voltage)
```

Defining and transformation of the corner points. First in the z′ plane.

```
z1 = i*height; z2 = 0; z3 = gap/2; z4 = gap/2 + elec;
```

The corner points in U-plane.

```
u1 = sinh((pi/height)*(z1-i*height/2)); u2 =
sinh((pi/height)*(z2-i*height/2)); u3 =
sinh((pi/height)*(z3-i*height/2)); u4 =
sinh((pi/height)*(z4-i*height/2));
```

Defining the constant for the Möbius transformation based on the coordinates in the U-plane.

```
C = -(1.*(u4*u2+u1*u3+u4*u3-1.*u3^2-1.*u2^2+u1*u2-
2.*u1*u4+2.*sqrt(-1.*u4^2*u3*u1-1.*u3^2*u1*u2-
1.*u1^2*u4*u2-1.*u1^2*u4*u3+u4^2*u2*u3-1.*u4*u3*u2^2-
1.*u1*u3*u2^2+u4*u2^2*u1+u1*u3^2*u4-1.*u4^2*u2*u1+
u1^2*u3*u2+u3^2*u2^2+u1^2*u4^2+2.*u4*u2*u1*u3-
1.*u4*u2*u3^2)))/(-1.*u1*u3+u4*u2+u1*u2-1.*u4*u3+
u3^2-1.*u2^2);

B = (u3*(C-1)-u2*(1+C))/2;

D = u3*(1-C)+B;
```

The defining of the Möbius coordinates (V-plane). The interior electrode edges are at +/-1, and the outer edges are given by $v1 = -v4$. As well as taking the real part of the coordinates to make sure that they are real.

```
v1 = (u1+B)/(C*u1+D);
v1 = real(v1);
v2 = (u2+B)/(C*u2+D);
v2 =
real(v2);
v3 = (u3+B)/(C*u3+D);
v3 = real(v3);
v4 = (u4+B)/(C*u4+D);
v4 = real(v4);
```

Defining the modulus for the Schwartz-Christoffel transformation (W-plane).

```
k = 1/v4;
k = real(k);
```

Defining the transformation for the coordinate x, y.

```
z = x + i*y;
u = sinh(pi/height*(z - i*height/2));

v = (u+B)./(C*u+D);
```

Defining the derivatives of the transformations for the coordinate x, y.

```
dudz = pi/height*cosh(pi*z/height-i*pi/2);

dvdu = (D-B*C)./(D+C*u)./(D+C*u);

dwdv = 1./sqrt((1-k*k.*v.*v).*(1-v.*v));
```

Calculations of the electric fields in the different planes.

```
Ew = voltage/(2*ellipke(k^2));

Ev = Ew.*conj(dwdv);

Eu = Ev.*conj(dvdu);

Ez = Eu.*conj(dudz);

Ex = real(Ez); Ey = imag(Ez);

Ewx = real(Ew);

Ewy = imag(Ew);

Evx = real(Ev);
```

```
Evy = imag(Ev);

Eux = real(Eu);

Euy = imag(Eu);
```

D.2.2 Script for Plotting of the Field Lines

Calculates the grad (E^2) at a coordinate x, y.

```
function [Ex, Evx, u] =
Calculatefieldlines(elec, gap, height,
voltage, medium_conductivity,
metal_elec_length, channel_length)
```

Define the (effective) voltage

```
V_eff = 20;
```

Calculate a matrix of Ex and Ey values for setting the gradient.

```
counts = 250;

Ex = ones(counts, counts);

Ey = ones(counts, counts);

y = [1:counts]*height/counts;

x1 = [1:counts]*(elec*5)/counts;

x2 = fliplr(-1*x1); x = [x2 x1];

[X, Y] = meshgrid (x1, y);
[Ex1, Ey1, Eux, Euy, Ew, u, u1, u3, u4,
k, B, C, D] =
```

```
Electric_Field_in_Microchannel(elec, gap, height, X,
Y, V_eff);

Ex2 = fliplr(-1*Ex1); Ey2 = fliplr(Ey1);

Ex = [Ex2 Ex1]; Ey = [Ey2 Ey1];

no_of_streamlines = 20;
```

Calculation of the electric field lines in the W-plane.

```
Ewx = real(Ew); Ewy = imag(Ew);

K_k2 = ellipke(k^2); K_1minusk2 = ellipke(1-k^2); wx =
[-K_k2:2*K_k2/counts:K_k2];

wy = [0:(K_1minusk2-1e-4)/counts:K_1minusk2];

[Wx, Wy] = meshgrid(wx, wy);

swy = [1e-4:(K_1minusk2-1e-4)/no_of_streamlines:K_1minusk2];

swx = -K_k2*ones(size(swy)); Ewxmat = Ewx*ones(size(Wx));

Ewymat = Ewy*ones(size(Wx));

sw1 = stream2(Wx, Wy, Ewxmat, Ewymat, swx, swy); figure
streamline(sw1);
```

Calculation of the electric field lines in the V-plane.

```
vx = [-1/k-100:2/k/counts:1/k+100];

vy = [1e-4:(120-1e-4)/counts:100];

[Vx, Vy] = meshgrid(vx, vy); v=Vx+i*Vy; dwdv =
1./sqrt(1-k*k.*v.*v)./sqrt(1-v.*v);

size(dwdv); Ev=Ew*conj(dwdv);
```

```
Evx = real(Ev); Evy = imag(Ev);

svx = [-1/k:1/(k*no_of_streamlines):1];

svy = ones(size(svx))*1e-1;

sv1 = stream2(Vx, Vy, Evx, Evy, svx, svy);

figure streamline(sv1); min(min(vx)); max(max(vx));
```

Calculation of the electric field lines in the U-plane.

```
uy = [imag(u4):abs(u4-u1)/counts:abs(u1)+19];

ux = [1e-5:(60-1e-5)/counts:50];

[Ux, Uy] = meshgrid(ux, uy);

u=Ux+i*Uy; dvdu = (D-B*C)./(D+C*u)./(D+C*u);

v = (u+B)./(C*u+D);

dwdv = 1./sqrt(1-k*k.*v.*v)./sqrt(1-v.*v);

Ev=Ew*conj(dwdv); Eu=Ev.*conj(dvdu);

Eux = real(Eu); Euy = imag(Eu);

suy = [-1:2/no_of_streamlines:1];

sux = ones(size(suy))*1e-5;

su1 = stream2(Ux, Uy, Eux, Euy, sux, suy);

figure streamline(su1);
```

Calculation of the electric field lines in the Z′-plane.

```
x1 = [1e-4:(2*elec)/counts:100];

y = [1e-4:height/counts:100];

[X, Y] = meshgrid(x1, y); x2 = fliplr(-1*x1);

x = [x2 x1]; z = X + i*Y;

u = sinh(pi/height*(z - i*height/2));

v = (u+B)./(C*u+D);

dudz = pi/height*cosh(pi*z./height-i*pi/2);

dvdu = (D-B*C)./(D+C*u)./(D+C*u);

dwdv = 1./sqrt(1-k*k.*v.*v)./sqrt(1-v.*v);

Ev = Ew.*conj(dwdv); Eu = Ev.*conj(dvdu);

Ez = Eu.*conj(dudz); Ex1 = real(Ez);

Ey1 = imag(Ez); Ex2 = fliplr(-1*Ex1);

Ey2 = fliplr(Ey1); Ex = [Ex2 Ex1];

Ey = [Ey2 Ey1];

[sx,sy] = meshgrid(5e-4,
0:height/no_of_streamlines:height);

s1 = stream2 (X, Y, Ex1, Ey1, sx, sy);

[sx2,sy2] = meshgrid(-5e-4,
0:height/no_of_streamlines:height);

figure s2 = stream2(x, y, Ex, Ey, sx2, sy2);

streamline(s1); streamline(s2);

figure streamline(s1);
```

D.2.3 Script for Calculations of the Field

Defining the coordinates x, y.

```
counts = 2000; x = [1e-5:520/counts:520];
y = [1e-5:30/counts:30];

x2 = fliplr(-1*x); x1 = [x2 x];

[X, Y] = meshgrid(x, y);
```

Calculate the field at different height in the channel.

```
for ii = 1:3

    yy = 5+(10*(1*ii-1))

[Ez, Ex, Ey, Eux, Euy, Ew,
u, u1, u3, u4, k, B, C, D] =
Electric_Field_in_Microchannel(20,
10000, 30, X, yy, 10);

Ez1 = Ez; Ez2 = -Ez;

Ex1 = real(Ez1); Ey1 = imag(Ez1);

Ex2 = fliplr(real(Ez2)); Ey2 = fliplr(imag(Ez2));

Ex = [Ex2 Ex1]; Ey = [Ey2 Ey1];

Ez = Ex.^2 + Ey.^2;

Ez = sum(sqrt(Ez))./counts;

Ez = Ez./2.*10^(5); plot(10*x1, Ez)

hold on

end

xlabel('Channel length (\upmu m)', 'FontSize', 24)
```

```
ylabel('Electrical field (V/m)', 'FontSize', 24)
```

D.3 Effective Voltage in Main Channel Program

The scripts for the calculation (for optimization of the geometry) of the effective potential in the main channel for the system used in the DEP experiments.

D.3.1 Script for Calculations of the Cell Constant

This script is the same as the for calculating the E field, except that at the end it gives the relation between $K(k)$ and $K(\sqrt{1-k^2})$

```
function cell_constant =
Microchannel_cell_constants_for_coplanar_electrodes(
electrode_width,
gap_width, channel_height)

z1 = i*height; z2 = 0; z3 = gap/2; z4 = gap/2 + elec;

u1 = sinh((pi/height)*(z1-i*height/2)); u2 =
sinh((pi/height)*(z2-i*height/2)); u3 =
sinh((pi/height)*(z3-i*height/2)); u4 =
sinh((pi/height)*(z4-i*height/2));


C =
-(1.*(u4*u2+u1*u3+u4*u3-1.*u3^2-1.*u2^2+u1*u2-
2.*u1*u4+2.*sqrt(-1.*u4^2*u3*u1-1.*u3^2*u1*u2-
1.*u1^2*u4*u2-1.*u1^2*u4*u3+u4^2*u2*u3-1.*u4*u3*u2^2-
1.*u1*u3*u2^2+u4*u2^2*u1+u1*u3^2*u4-1.*u4^2*u2*u1+
u1^2*u3*u2+u3^2*u2^2+u1^2*u4^2+2.*u4*u2*u1*u3-
1.*u4*u2*u3^2)))/(-1.*u1*u3+u4*u2+u1*u2-1.*u4*u3+
u3^2-1.*u2^2);

B = (u3*(C-1)-u2*(1+C))/2;

D = u3*(1-C)+B;
```

```
v1 = (u1+B)/(C*u1+D);
v1 = real(v1);
v2 = (u2+B)/(C*u2+D);
v2 =
real(v2);
v3 = (u3+B)/(C*u3+D);
v3 = real(v3);
v4 = (u4+B)/(C*u4+D);
v4 = real(v4);


k = 1/v4
```

Calculation of the cell constant using the ellipke function.

```
K = ellipke(k^2)

K1 = ellipke(1-k^2)

cell_constant = K/K1;
```

D.3.2 Script for Calculations of the Effective Potential

Calculation of effective voltage in the main channel.

```
function [V_eff, V_x, Integral_Exchannel,
Integral_Exchannel_squared] =
Effective_voltage_for_coplanar_electrodes (elec,
gap, height,
voltage, medium_conductivity,
metal_elec_length, channel_length,
cheight);

clear V_eff
```

Calculation of the channel resistance.

```
cell_constant =
Microchannel_cell_constants_for_coplanar_electrodes
(elec, gap, height);

R_channel =
4*cell_constant/(medium_conductivity*height);
```

Calculation of the integral of the field and the integral squared field using trapeze integration, the boundaries have been found by investigation of the plotted field.

```
access_channel_cell_constant =
Microchannel_cell_constants_for_coplanar_electrodes
(metal_elec_length, 2*channel_length, cheight);


 x1 = gap/2:(elec/10000)/1e6:gap/2+elec/10000;
 x2 = gap/2+elec-elec/10000/2:(elec/10000)/1e6:elec+gap/2;
 x3 = gap/2+elec/10000:(elec-2*elec/10000)
 /1e6:gap/2+elec-elec/10000;

Integral_Exchannel = (trapz(x1,myfun(x1)) +
trapz(x2,myfun(x2))+trapz(x3,myfun(x3)));
Integral_Exchannel_squared
= (trapz(x1,myfun2(x1)) +
trapz(x2,myfun2(x2))+trapz(x3,myfun2(x3)));
```

Calculation of the access channel resistance.

```
R_access = access_channel_cell_constant*
(Integral_Exchannel_squared)/(medium_conductivity*
(Integral_Exchannel^2))
Rx = access_channel_cell_constant/
(medium_conductivity*cheight)
```

Calculation of the effective voltage.

```
V_eff = voltage*R_channel/(R_channel + 2*R_access)
```

```
V_x = voltage*R_channel/(R_channel + 4*Rx)
```

Defining the functions for integrating the E field and E^2.

```
function Echannel =
myfun(x) [Ezz, Exchannel, Eychannel] =
Electric_Field_in_Microchannel(elec, gap,
height, x, 1e-6, 1);
Echannel = ((Exchannel.^2).^(1/2) +
(Eychannel.^2).^(1/2)); end

function Echannel_squared =
myfun2(x) [Ezz, Exchannel, Eychannel] =
Electric_Field_in_Microchannel(elec,
gap, height, x, 1e-6, 1);
Echannel_squared = ((Exchannel.^2).^(1/2) +
(Eychannel.^2).^(1/2)).^2; end

end
```

Appendix E

KPM on Printed Proteins

To measure local physical properties of protein-protein systems, SPM techniques such as KPM can be used to measure changes of local electrostatic properties. In this work the proteins were transferred by micro-contact printing on a glass substrate [1].

E.1 Stamp Fabrication

To transfer the proteins and study their interaction, micro-contact printing was used to create patterns suitable for SPM. As several others have already reported the use of Polydimethylsiloxane (PDMS) as a stamp in micro-contact printing [73, 74, 117, 118, 119, 120], this was also chosen for this experiment. The pattern chosen for the stamp was simple parallel lines, as these made it possible to have the four different surfaces (bare surface, IgG, anti-IgG, and the interaction site) close to each other. The width of the lines needed to be as small as possible in order to fit the scan area of the SPM system. As the SPM system's maximum resolution is 1024 $\times$ 1024 pixels then for a scan area of 20 μm $\times$ 20μm the resolution is about 20 nm per pixel. The width of the line was chosen to be 3 and 5 μm (1 μm was tried as well but it did not develop well) as this is the smallest linewidth that can be reproducibly fabricated using standard photolithography without optimizing the process [121]. The area covered by the lines was set to 1 $\times$ 1 cm. Appendix B.5 shows the mask layout.

The molds were made on a silicon wafer using an Advanced Silicon Etcher (ASE). The ASE machine used was made by Surface Technology Systems Plc. The fabrication process was (see appendix B.4 for full process): a 4 inch silicon wafer was HDMS treated and AZ5214e photo resist was spun on, which will function as an etch mask for the ASE process. The wafer was exposed and developed, using a

[1] The work described in this section was done in collaboration with Martin Græsvænge Hansen and Jaime Castillo.

negative photolithography process [121]. The ASE etch was done in cycles of 2.6 s etch and 2.0 s passivation. The etching was done with a gas flow of SF_6 = 260 sccm (Standard Cubic Centimeters per Minute) and O_2 = 26 sccm. The passivation was a gas flow of C_4F_8 = 120 sccm. This gave an etch depth of around 1 μm, giving the PDMS structures an aspect ratio of 3 or 5 to 1 which should ensure that they do not collapse during printing. Finally the remaining resist was removed with acetone and the individual molds were diced.

For the fabrication of the stamp PDMS from PDMS Sylgard R 184, Dow Corning was used, with a mixed ratio of 10 : 1 volume of polymer to hardener [122]. The mixture was added on top of a silicon mold placed in a plastic container and it was aimed to have a total stamp thickness of 4 to 5 mm. The PDMS stamps were cured for 3 h at 70C, in order to obtain a high compression modulus [123]. This is desirable in order to avoid collapse of the lines in the stamping process. They were then peeled off and were ready for stamping (for more on the fabrication of the stamp see appendix B.4).

E.2 Pattern Transfer of Proteins

In this section the method for micro-contact printing of proteins on glass cover slides will be described. The proteins used were as described earlier, immunoglobulin G (IgG), both the antibody and antigen. The anti-IgG (antibody) and IgG (antigen) were prepared separately in two different buffers: A Phosphate-Buffer (PB, pH = 7.0 ±0.1, VWR), and a Phosphate-Buffered Saline solution with sodium chloride (PBS, pH = 7.2 ±0.1, 150 mM, Fluka). All the protein solutions were made with a concentration of 100 μg/ml. The reason for this was that salt concentration has an influence on protein binding as shown by A. Holmberg *et al.* [124]. The pattern transfer of proteins from a PDMS stamp to a substrate is a widely used method [74, 73, 117, 118, 119, 120]. Even so, it is still unclear what causes the proteins absorbed on the PDMS stamp to be transferred onto the substrate during the stamping process. It is assumed that the proteins are transferred from the stamp to the substrate, if they can interact more strongly with the substrate than with the stamp [119]. The mechanisms of the transfer are believed to be influenced by the difference in wettability between the stamp and substrate. It has been reported by Tan *et al.* [119] that increasing the wettability of the substrate and/or lowering it for the stamp will result in a better protein transfer. Having a hydrophobic stamp as is the case with PDMS is not without a downside. The hydrophobic stamp and its low wettability causes problems, when the proteins are diluted in a water based solution (such as the PBS), as the hydrophobicity will result in a poor coverage of proteins on the PDMS stamp [120].

For transferring of the proteins the PDMS stamp has to be soaked in the protein so-

lution before stamping. A variety of times has been reported in the literature ranging from 15 min to 100 min. [74, 73, 118, 119, 120, 125, 126]. The time needed to transfer the proteins from the stamp to the substrate, also called the stamping time, varies from just a few seconds and up to 15 min [74, 73, 118, 119, 120, 125, 126]. A lot of different combinations have been tested during this work in order to obtain a good protein patterning on a glass cover slide.

The optimal process of transferring the proteins was based on the work done by Y. J. Oh *et al.* [74] with a few changes. During the printing experiments sometimes the pattern was not transferred. Optimization of the transfer process was done by varying the printing and drying time, however the results did not change much. It is possible that the humidity might have influenced the transfer as the weather conditions during the time of the experiments changed from dry to wet. This is however not something, that has been closely monitored in the laboratory during the succession of experiments, and even if it had there was no simple solution to solving the issue in case this was the reason for the varying results. The process followed is described below:

1. The PDMS stamp is cleaned by flushing it with ethanol and then drying with pressurized nitrogen.

2. The protein solution (IgG) is now added to the PDMS stamp by adding a drop that covers the area with the protrusions.

3. After 20 min. the solution of proteins on the stamp is removed and the stamp is dried in ambient air for 10 min. If the stamp is not dry after this time, pressurized nitrogen is used.

4. If the buffer with salt is used, the stamp is lightly flushed with deionized and millipore-filtered water and dried with nitrogen.

5. The glass cover slide where the proteins are to be printed on is cleaned. This is done by flushing it with ethanol, deionized and millipore-filtered water, and again ethanol.

6. Proteins are then transferred to the cover slide by placing the stamp on the cover slide. To ensure conformal contact between the cover slide and stamp a weight of 550 g is placed on the back of the PDMS stamp. This delivers a force of approximately 5 N.

7. This was repeated with the anti-IgG solution, but the stamp was now rotated 90° in order to get the crossover areas of the two types of proteins.

For validating that the micro-contact printing did result in the transfer of the proteins to the glass cover slide printing using the anti-IgG protein labeled with

Cy3 (Sigma C2181) was used. The image in figure E.1 A shows an optical image of a glass slide illumined with UV light, while figure E.1 B shows a topography image of the same sample. As can be seen from figure E.1 A there are fluorescence lines in the image, while figure E.1 B shows a topography image of the same array. The grey average line profile from figure E.1 B is plotted in figure E.1 C, and shows the height of the anti-IgG proteins to be around 6 nm, which should correspond to a monolayer (see section 1.6.3).

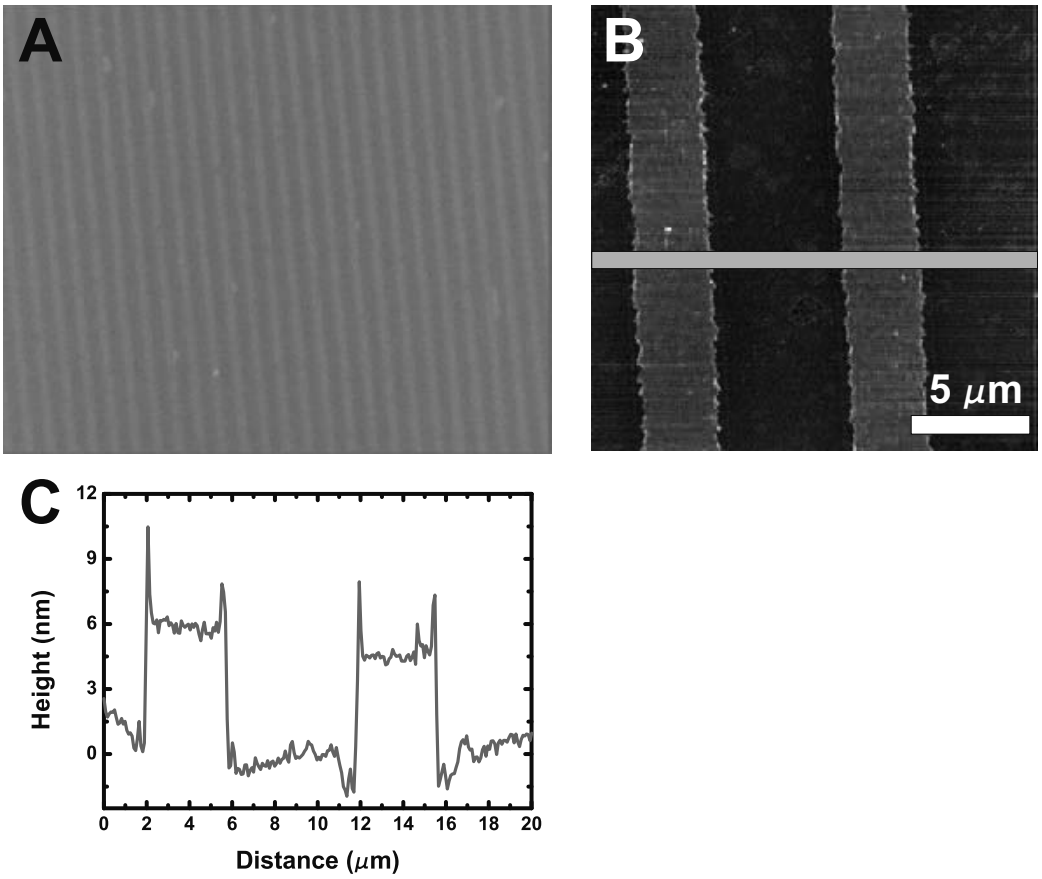

Figure E.1: A) Optical image of fluorescence of anti-IgG line made by micro-contact printing B) topography image of the same sample C) average line profile from B (the grey line).

The micro-contact printing of the protein arrays was not totally uniform and when the samples were inspected it was revealed that large areas had only lines in one direction or none at all.

E.3 Setup

The scanning probe microscope used in this project to obtain the data was a CP-II SPM system from Veeco. For the KPM measurements a TermoMicroscopes setup was used. It consisted of a Stanford Research Systems SR830 lock-in amplifier and an ECAP module to measure the surface potential. The correct operation of the lock-in amplifier (set of the phase lack, gain, and time constant) will give the amplitude of the locked signal. Equation 2.29 indicates that the locked signal needs to be minimized in order to find the surface potential. To lock the signal the lock-in amplifier is used, while for minimizing the signal the ECAP module is used to vary the DC potential (V_{DC} from equation 2.29). As the lock-in amplifier gives the amplitude of the locked signal (which according to equation 2.29 needs to be minimized) the ECAP minimizes the signal by varing the DC potential. So for the setup to mimic the minimizing of the DC potential of equation 2.29. The ECAP controller contains a PI-controller which is used to vary the DC potential in order for the tip potential to be that of the sample. Figure E.2 is a schematic drawing of the layout of the setup.

The lock-in amplifier generates an AC potential (the reference signal), which is sent to the ECAP module and added with a DC potential from a PI-controller. This potential is then applied to the cantilever (figure E.2, *A*). The vibration of the cantilever, which consists of two signals, the vibration caused by the Van der Waals interaction between the tip and sample and of the potential interaction between the tip and sample, is sent to the lock-in amplifier (figure E.2, *B*). The lock-in amplifier generates a DC voltage based on the signal from the tip [17], as the lock-in amplifier is used to generate the reference signal. This is then fed to the ECAP module (figure E.2 *C*), and the PI controller changes the DC potential in order to change the signal from the lock-in amplifier (figure E.2 *D*) to zero. This signal is then recorded as the potential of the sample (V_S). Further as the signal retrieved from the SPM system may have a phase lag, one has to set the phase of the reference signal to match that of the recorded signal from the SPM system. This is not an easy task as the response from the PI-controller in the ECAP module can change the signal. Further, the PI-controller needs to be adjusted as it needs to be fast enough to make the changes, but not too fast so it saturates.

For the measurements AFM cantilevers coated with platinum from Budgetsensors (model BS-*Electri*Multi75) were used. Analysis of the recorded data from the SPM system was carried out using the ”SPIP” software [15].

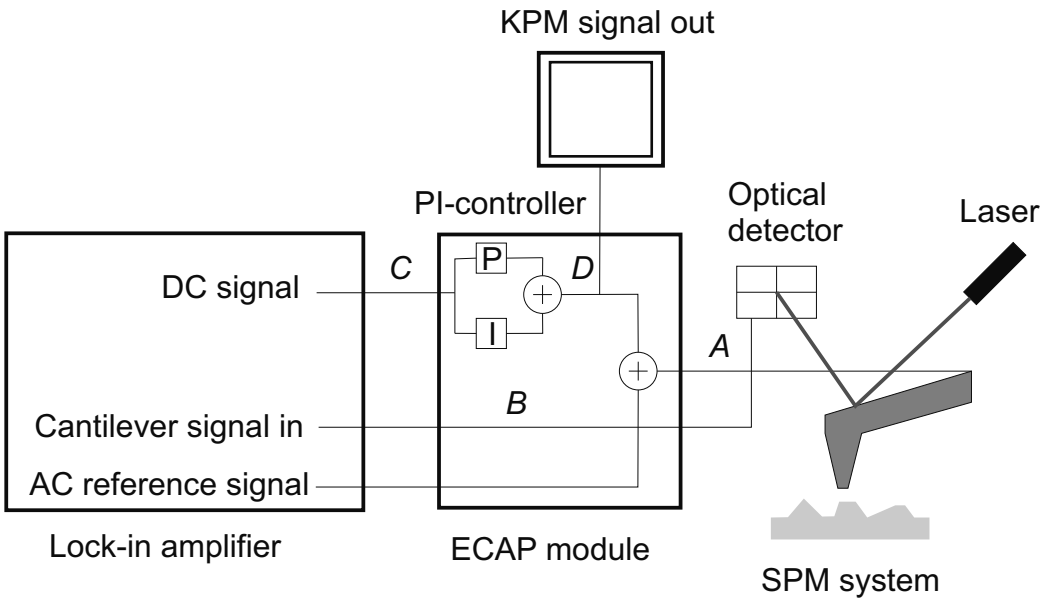

Figure E.2: Drawing of the KPM setup used in this experiment. The lock-in amplifier generates an AC potential reference signal, which is sent to the ECAP module and added with a DC potential from a PI-controller. *A*) This potential is then applied to the cantilever. *B*) The vibration of the cantilever, which consists of two signals (the change in vibration caused by the Van der Waals interaction between the tip and sample and of the potential interaction between the tip and sample) is sent to the lock-in amplifier. The lock-in amplifier generates a DC voltage based on the signal from the tip [17], as the lock-in amplifier is used to generate the reference signal. *C*) This is fed to the ECAP module. *D*) Here the PI controller changes the DC potential in order to change the signal from the lock-in amplifier to zero. This DC signal is then recorded as the potential of the sample.

E.4 Results and Discussion

All SPM images shown in this section were obtained at 512×512 pixels. The scan rate was 0.4 Hz. The setting on the lock-in amplifier was an amplitude of 3 V and a frequency of 20 kHz for the AC reference signal. The sensitivity was set to 1 mV and the time constant to 10 ms. The ECAP module was set to Filter: On, Mode: EFM, Feedback: On, Integral: Enable, Proportional: 10, and Integral: 1. The stated values were found by optimizing the different parameters in order to get the best signal to noise ratio.

As stated earlier (section E.2) micro-contact printing was done with two different buffers (no salt and with sodium chloride). The samples were stored at 5 °C and a custom made SPM holder was made in order to keep the samples at this temperature during scanning. The layout of the holder is sketched in figure E.3. It consisted of a Peltier element between two copper plates of 2 mm thickness fitted with one thermocouple each.

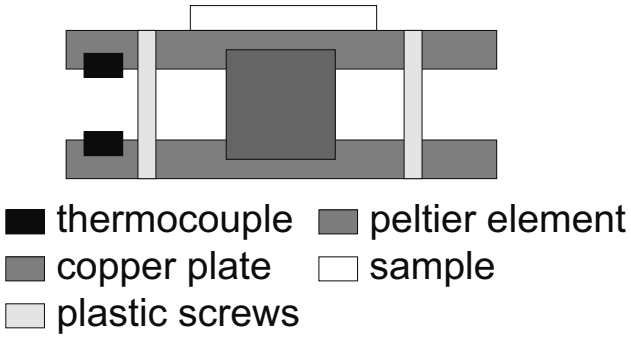

Figure E.3: Schematic drawing of the holder made for the SPM system to keep the temperature stable.

An Agilent DC power supply (model: E3643A) and two Tenma 72-7760 multimeters were used to measure the temperature of the thermocouples. The plates were kept together by plastic screws (to keep the gradient between the two plates at a minimum) and in between them the peltier element was mounted. The thermocouples were used to measure the temperature on the two plates. The holder was used to keep the temperature at around 5 °C during the scanning, in order to keep the conditions the same as storage. Six samples with PB buffer solution and five samples with the sodium chloride solution were made and measured.

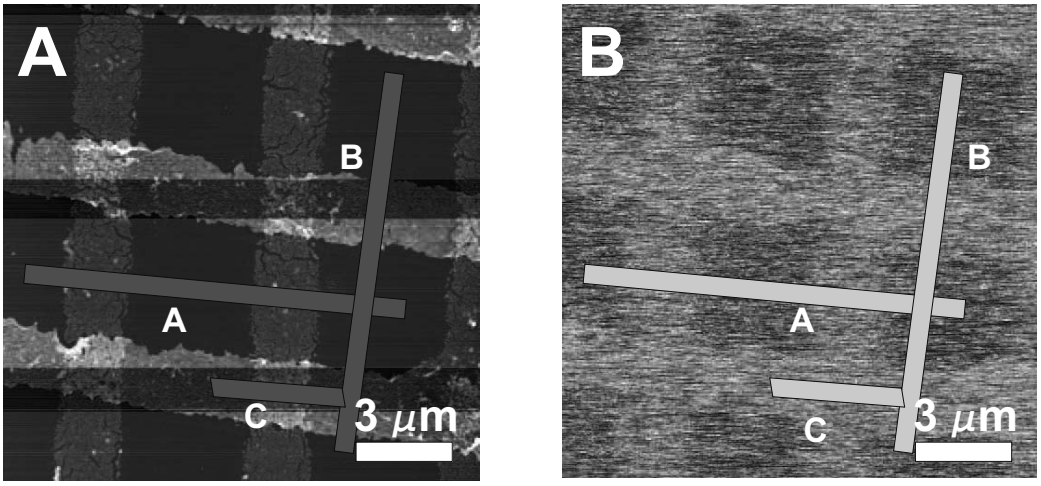

Figure E.4: A) Topography of the micro-contact printed proteins pattern, based on a saltless buffer solution. The topography image have some darker lines along the scan lines these are due to the software (SPIP [15]) used for flattening of the image B) KPM image of the same pattern. The bars are line profiles which are shown in figure E.5.

Figure E.4 A shows a typical topography image of an array line patterns of IgG and anti-IgG where the PB buffer was used for the solution. The 3 μm wide

horizontal lines are anti IgG while the vertical ones are IgG. The image have some darker lines along the scan lines these are due to the software (SPIP [15]) used for flattening of the image. Figure E.4 B shows the corresponding KPM image.

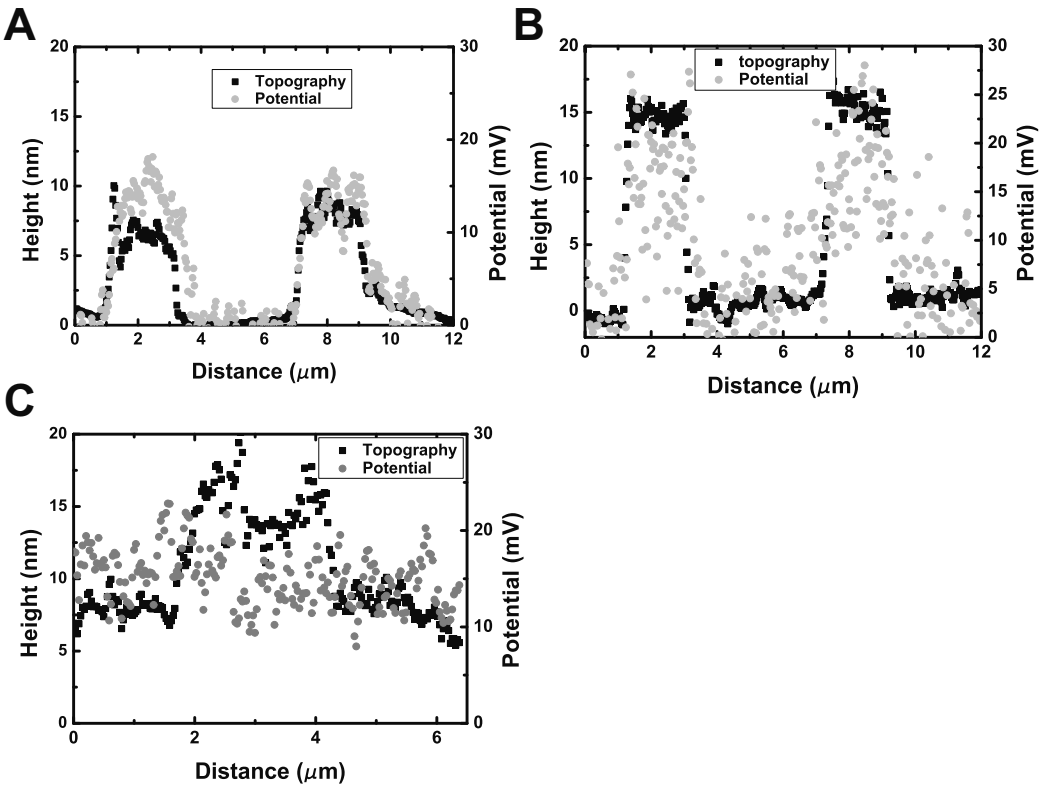

Figure E.5: A) Average line profiles from figure E.4 A and B (long horizontal lines), B) average line profiles from figure E.4 A and B (vertical lines), C) average line profiles from figure E.4 A and B (short horizontal lines).

Figure E.5 A, B, and C shows the average line profiles from figure E.4 A and B, where the black line corresponds to the topography and the grey line is the potential. As can been seen from the figure the potential line profiles are more or less on top of the topography lines. Figure E.5 C shows the cross area which roughly corresponds to the sum of the topography height of the two other line profiles. The KPM signal does not shows any variation as the topography signal does.

Figure E.6 A shows a typical topography image of array line patterns of IgG and anti-IgG where the PBS (NaCl) buffer was used for the solution. The 3 μm wide horizontal lines are anti IgG while the vertical ones are IgG. Figure E.6 B shows the corresponding KPM image.

Figure E.7 A, B, and C shows the average line profiles from figure E.7 A and B, where the black line corresponds to the topography while the grey line is the potential. Figure E.7 C is the cross area. There is here a signal from the KPM

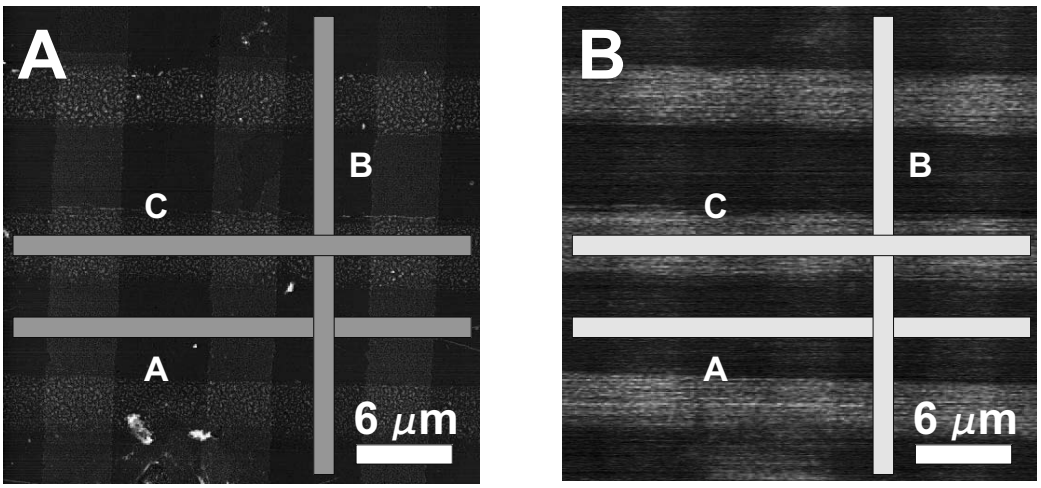

Figure E.6: A) Topography of the micro-contact printed proteins pattern, based on a salt (NaCl) buffer solution (PBS) B) KPM image of the same pattern. The bars are line profiles which are represented in figure E.7.

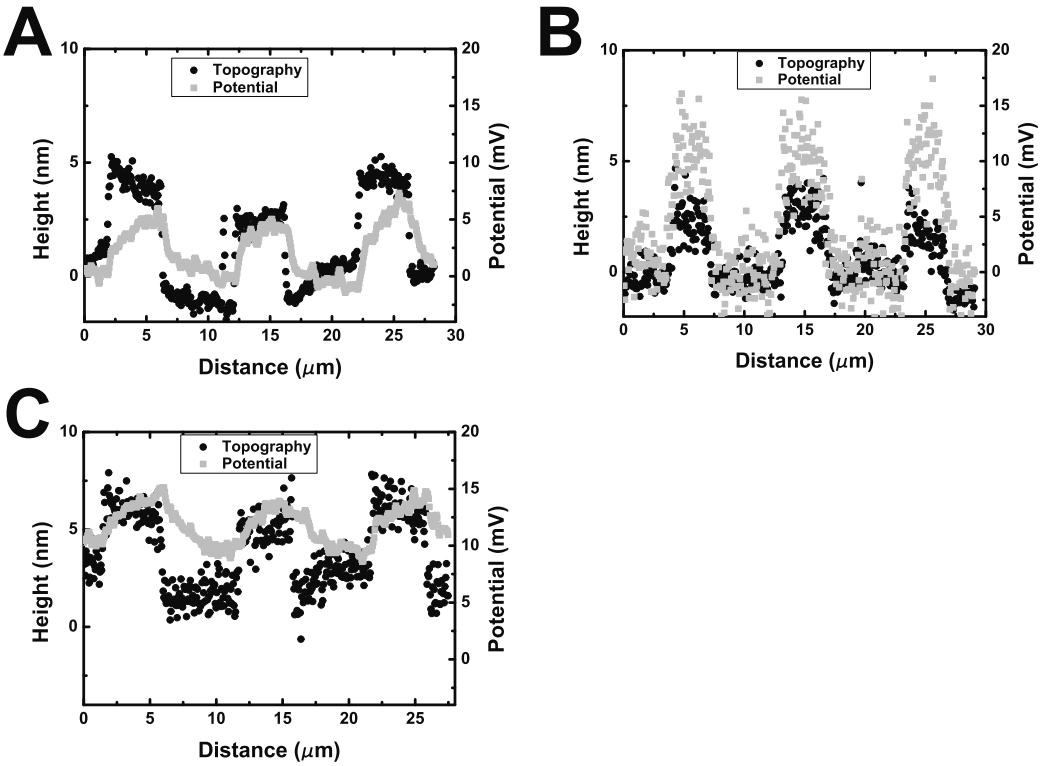

Figure E.7: A) Average line profiles from figure E.6 A and B (long horizontal lines), B) average line profiles from figure E.6 A and B (vertical lines), C) average line profiles from figure E.6 A and B (short horizontal lines).

images, which was not present in figure E.5.

The average height of the lines was estimated by taking 10 scan lines and average them and then measure the difference between the background and the top of the line. The average height of the IgG lines was 7-9 nm when patterned using the buffer without salt, and 6-8 nm for the salt (NaCl) buffer. As it would be expected they are in the same range. For the anti-IgG lines the average height was 7-8 nm for the PB buffer and 6-7 nm for the PBS (NaCl). Here the height variation is also within the same range. For the cross area (the area of the sample were the different proteins cross) the height was 10-20 nm for the two different buffers. Table E.1 summarizes the estimated heights of the different layers.

Buffer type	IgG	Anti-IgG	Cross area
PB	7-9 nm	7-8 nm	12-21 nm
PBS (NaCL)	6-8 nm	6-7 nm	10-18 nm

Table E.1: Table of the height of the different layers of proteins after micro-contact printing.

In literature the height of a monolayer of IgG and anti-IgG has been found to be 8.5-14.5 nm and 4-9 nm respectively, while the height of the binding area is found to be 10.5-18.5 nm [75, 76, 127]. our results are therefore in good agreement with previous reports.

The potential was measured with respect to the bare substrate which gave potential differences of 7-19 mV for IgG in the PB solution. For the PBS (NaCl) based solution the potential differences was 6-20 mV for the IgG, while for the anti-IgG the potential differences were measured to 12-24 and 13-22 mV for the PB and PBS (NaCl) respectively. The values for the cross areas were measured to 14-24 and 10-40 mV for the PB and PBS (NaCl) respectively. Table E.2 summaries the above results.

Buffer type	IgG	Anti-IgG	Cross area
PB	7-19 mV	12-24 mV	14-24 mV
PBS (NaCL)	10-15 mV	13-22 mV	8-41 mV

Table E.2: Table of the measured surface potential for the different layers of proteins relative to the bare substrate.

Table E.1 shows the variation in the height of the different protein areas. As can be seen the cross layer thicknesses vary with around 10 nm. As described in section 1.6.3 the dimensions of the protein are not the same in the different

directions. The reason for the large height variation is therefore probably that the proteins are not lying in the same way. As can be seen from table E.2 the potential differences of the lines for the two different buffers are in the same range, however, the variation from sample to sample is large. The reason for this could be, as discussed in section 2.4.2, that the potential measured is an average sum of the potential under the tip and the surface potential felt by the cantilever. As the coverage with the protein arrays is far from complete this could vary the average surface potential and therefore the measured potential. Another possible source for error could be that even though the temperature was kept constant there was no control over the humidity.

E.5 Summary

As these experiments are preliminary there are still several parameters which needs to be investigated such as the salt leftover on the sample influence on the KPM image, as well as this is done under ambient conditions how would this influence the different protein layers.

Appendix F

Acoustic sorting of Chromosomes

Attempts to sort human chromosomes by acoustic sorting were carried out at Lund University with the help of the group of Thomas Laurell and especially his Ph.D. student Carl Grenvall.

F.1 Results

The chromosomes were prepared in suspension at DTU and brought to Lund University. Here the suspension was introduced into a fluidic system, through an inner channel that was pinched by two outer flows. An acoustic force was applied and the hypothesis was that the chromosomes (or some of them) will move to the outer flow. At the end of the chip, samples are collected from outer and inner flow.

The collected samples were brought back to DTU where Jacob Moresco Lange made a PCR analysis of them, checking for the X and Y chromosomes as they are roughly the largest and smallest chromosomes in the genome respectively. The idea was that if size sorting of the chromosomes was taking place by acoustic sorting then checking for these two chromosomes was going to be enough to conclude. The PCR analysis indicated that the chromosomes are indeed affected by the acoustic force and moved from the inner flow to the outer flow. However, there appears to be no size sorting. For this reason no new attempts were made and the project ended.

Appendix G

Coulter Counter for Chromosome Detection in Fluidic

Attempts to fabricate a simple Coulter counter for the detection human of chromosomes was made using a micro fluidic chip consisting of a narrow slit and two planar electrodes for detecting impedance changes (see figure B.3).

G.1 Principle

The principle of the device is that as chromosomes pass in between the electrodes the impedance measured by the electrodes will monumentally change. It was hoped that different chromosomes would give different changes in the impedance. Figure G.1 shows the idea.

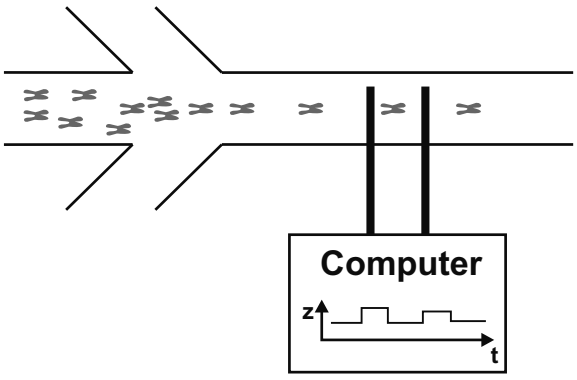

Figure G.1: Schematic drawing of the principle of the device to work as a Coulter counter for chromosomes.

Appendix B.3 shows the mask layout of the chip. As can be seen from appendix B.3 the channel narrows at the electrodes in order to increase the change in the impedance between the electrodes.

G.2 Results

The setup consisted of a microscope (Olympus model IX 51), a Tabor Electronics 50 MHz Function Generator 8550 for generating the electrical signal, while for recording the output signal a Stanford Research System model SR 570 current preamplifier connected to a computer equipped with a Data Acquisition Card (Model NI PCIe-6251) was used. A Chemix N300C syringe pump was used for driving the flow through the system. The setup aimed at detecting impedance changes by applying a fixed potential (sine signal) and then monitoring changes in the current. The function generator was used to generate a signal (one of the connections grounded see figure G.2), which was applied to the electrodes while the while the amplifier and the computer (using a LabView$^{\mathrm{tm}}$ program) was used to record any change in the current. A drawing of the setup is shown in figure G.2.

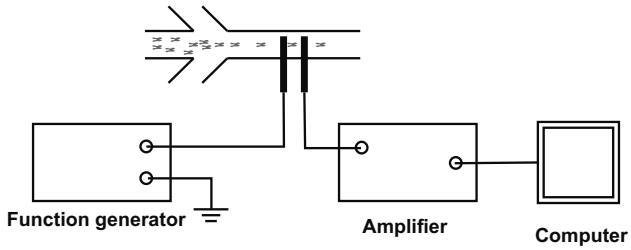

Figure G.2: Schematic drawing of the setup used for the Coulter counter.

Chromosomes were sent through the system and different frequencies were swept between 50 kHz to 10 MHz in order to check if the setup showed any respond. The amplitude of the signal was also swept between 100 mV to 1 V. As the setup gave no signal change with chromosomes passing through, no new attempts were made as the project ended.

Appendix H

Nano-sized Channel Fabrication using Dipeptide Superstructure

Attempts to fabricate nano-sized liquid channels using dipeptide tubes were made based on work done by J. Castillo *et al.* [128]. The idea was inspired by work done by N. Sopher *et al.* [129] where the same type of peptide tubes where used as molds for PDMS, but not in a controlled way. Figure H.1 shows the initial results done on one of J. Castillo devices. Figure H.1 A shows a single set of electrodes with a peptide tube immobilized by DEP. Figure H.1 B shows the same set of electrodes after PDMS was poured on top, cured, and removed. Figure H.1 C shows the molded structure in the PDMS.

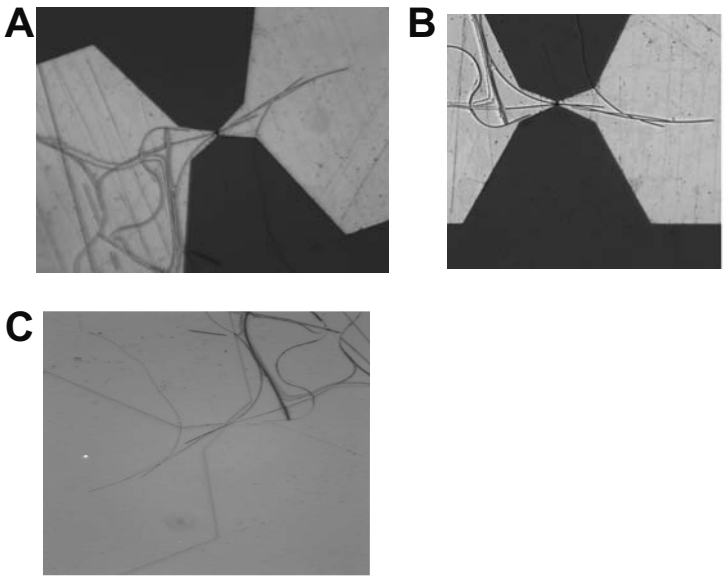

Figure H.1: Initial results: A) a single set of electrodes with a peptide tube immobilized by DEP B) the same set of electrodes after PDMS was poured on top, cured, and removed C) shows the molded structure in the PDMS.

H.1 Principle

The idea was to use a peptide tube as molds for two dimension nano-sized channels in a polymer. The controlled positioning was done with DEP on electrodes, while the polymer used was PDMS, which was poured on top and then cured. Figure H.2 shows the schematic drawing of the process.

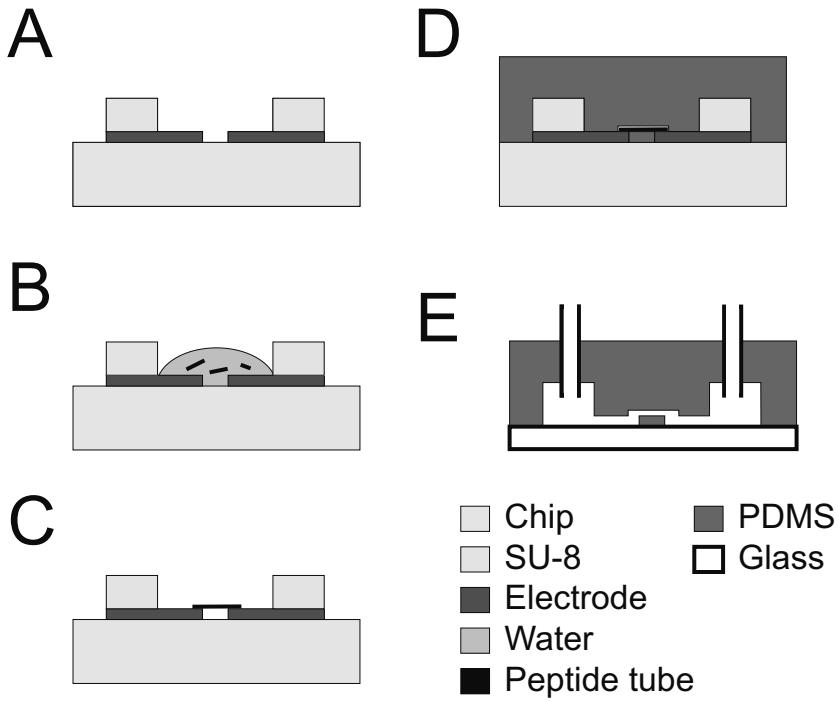

Figure H.2: Schematic drawing of the fabrication of the nano-sized channel. A) the chip, B) a droplet containing the peptide tubes is added on top of the electrodes, C) the liquid is removed and the chip is dried, D) PDMS is poured on top of the chip and is cured, E) the PDMS is removed and glass tubing is inserted for connections, and then irreversibly bonded to a glass cover slide.

The design of the chip was based on earlier work [128], but a layer of SU-8 was added on top of part of the electrodes to act as a cavity. Further, as the exact dimensions for the optimal design for the electrodes for immobilizing peptide tube had not been investigated the design used an array of pointy electrode sets of different sizes. There was two electrode designs, and for each type the distance between was varied as 1.5 μm, 2.5 μm, 4 μm, 6 μm, 7.5 μm, 10 μm, and 15 μm.

H.2 Results

The setup consisted of a microscope (Olympus model IX 51) and a Chemix N300C syringe pump, used for driving the flow through the fabricated channels. For bonding the PDMS to the glass slide a Electro Technic Products model BD-20V was used (see K. Haubert *et al.* [130] for a description of the bonding method).

For the DEP experiments a solution of peptide tubes were added on the electrodes and an AC signal with amplitude of 5 V and a frequency of 5 MHz was applied for 5 minutes. The AC signal was then turned off and the solution was removed from the chip by nitrogen flow.

The devices assembled as sketched in figure H.2 were first filled with a solution of Proteinase K (SigmaAldrich cat. No. P6556) at a concentration of 100 μg/mL into one of the chambers using the syringe pump. No liquid seems to pass from one chamber to the other. Figure H.3 shows one part of the filled chip with blue colored water along the barrier containing the peptide tubes.

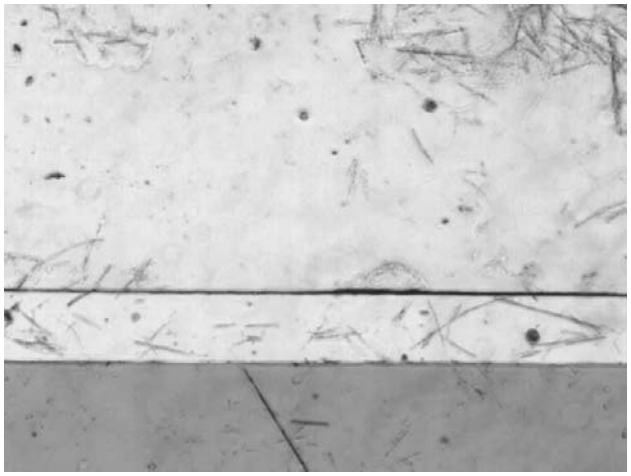

Figure H.3: Optical image of the interface between the two chambers. The bottom is filed with colored dye while the top is empty.

As time went by the pressure became too big for either the plastic tube connections or the bonded PDMS so the setup leaked. As it seemed that it was not possible to pass liquid from chamber to another, no new attempts were made as the project ended.

Appendix I

List of Journal Publications

This chapter contains the journals articles, which have been published, accepted, or submitted during the span of this Ph.D. project.

- Scanning conductance microscopy investigations on fixed human chromosomes. **C. H. Clausen**, J. M. Lange, L. B. Jensen, P. J. Shah, M. Dimaki, and W. E. Svendsen, Biotechniques, 44 (2), 225-228, 2008.

- A microfabricated platform for chromosome separation and analysis M. Dimaki, **C. H. Clausen**, J. M. Lange, P. J. Shah, L. B. Jensen, and W. E. Svendsen, Journal of Physics: Conference Series, 100 (5), 2008.

- Qualitative Mapping of Structural Different Polypeptide Nanotubes. **C. H. Clausen**, J. Jensen, J. Castillo, M. Dimaki, and W. E. Svendsen, Nano Letters, 8 (11), 4066-4069, 2008.

- Electrostatic Force Microscopy of Polypeptide Self Assembly Structures. **C. H. Clausen**, J. Castillo, S. P. Panagos, E. Kasotakis, A. Mitraki, and W. E. Svendsen, submitted to Ultramicroscopy.

- Investigations of the Dielectrophoretic Properties of Human Chromosomes. **C. H. Clausen**, M. Dimaki, S. M. Buckley, J. M. Lange, and W. E. Svendsen, submitted to Electrophoresis.

- Improved anti-stiction coating of SU-8 molds. J. Moresco, **C. H. Clausen**, W. Svendsen, Accepted in Sensors and Actuators B: Chemical.

- Fabrication of biological self-assembled nanoparticles on-chip. J. Castillo, A. C. Ø. Jensen, **C. H. Clausen** W. E. Svendsen, submitted to Advanced Materials.